NORTHWESTERN UNIVERSITY

Self-assembly and Transport in Chemical and Physical Networks

A DISSERTATION

SUBMITTED TO THE GRADUATE SCHOOL
IN PARTIAL FULFILLMENT OF THE REQUIREMENTS

for the degree

DOCTOR OF PHILOSOPHY

Field of Applied Physics

By

Dingwen Qian

EVANSTON, ILLINOIS

August 2024

ABSTRACT

After Albert Einstein's extraordinary insight into Brownian motion and Jean Baptiste Perrin's seminal study of Brownian motion of particle suspensions, humanity realized that matter is composed of atoms and molecules. How these tiny building blocks assemble into the colorful and complex world remains a question for all curious minds. Due to the existence of highly oriented and saturated interactions, network structures emerge as an important morphology for materials. Regarding the self-assembly process, I developed a phenomenological model of the nucleation and growth of hydrogen-bonded organic frameworks. The minimal model captures the complicated free energy landscapes of the network structure and predicts that the dominant product is sensitive to experimental conditions. We then proceed to a natural application of the network structure. Covalent organic framework (COF) membranes are known for their tunable pore sizes, which make them an ideal candidate for water purification and desalination. However, the morphology of COF membranes is not well understood due to their polycrystalline nature. The mechanism of size-sieving purification is therefore questionable. Experiments reveal that adsorption is an alternative mechanism to the filtration mechanism. My theoretical model provides important insights into why large dye molecules tend to have higher affinities for the membranes, explaining why people believe the plausible explanation of size-sieving filtration. The transport inside the network structure is highly coupled to the geometry of the host matrix. When the network is vibrating, the nonequilibrium transport is coupled to the vibrational degrees of freedom. We observe an interesting soliton-like excitation in the far-from-equilibrium regime.

ACKNOWLEDGEMENTS

I would like to express my deepest gratitude to many people who supported and accompanied me throughout my doctoral studies. First and foremost, I want to thank my advisor, Prof. Monica Olvera de la Cruz, for guiding me not only as a scientist but also as a mentor in life. Over the past six years, she gave me the freedom to explore the amazing world of soft matter physics and offered numerous forms of support along the way. I also want to thank the members of my committee, Prof. Michael Bedzyk and Prof. George C. Schatz, for taking the time to review this document and provide their valuable suggestions.

I am very fortunate to be a member of this intelligent, supportive, and fun lab. Dr. Felipe Jimenez led me into my first project and gave me tremendous guidance and advice. His ideas are very insightful and illuminating. I also want to thank Dr. Trung D. Nguyen, Dr. Baofu Qiao, and Dr. Eleftherios Kirkinis for their valuable help and advice in science and programming. Dr. Yihao Liang showed me the beauty of Monte Carlo simulations with different techniques, which helped me throughout my PhD research. I always enjoy scientific discussions with Dr. Hang Yuan, Dr. Yange Lin, Dr. Yao Xiong, and Yang Li, which led to many fruitful ideas. Dr. Leticia Lopez-Flores is always energetic and provides me with tremendous help in simulations. Dr. Han Umana Kossio is a great scientist who is knowledgeable in Chemistry, Biology, and many languages! It was always fun talking with him in the office. I also learned a lot about continuum physics from Dr. Ahis Shrestha and Dr. Aaveg Aggarwal. I wish that I could learn more about the subject and apply it in my future research. Dr. Ali Ehlen is a great scientist and person with great physics intuition. So is Hector, and I believe that makes them great partners. I am also indebted to Dr. Jianshe Xia, from whom I learned a lot of knowledge and techniques in polymer physics. I would also like to extend my gratitude to all the other group members, whose warmth and helpfulness

have greatly influenced my PhD life.

My PhD life would not have been complete without my friends and classmates. It was a great time studying, cooking, and playing with my Applied Physics cohort. I also made many great friends in the English program, starting even earlier than the first quarter at Northwestern. I would like to express special gratitude to my love, Yaxin Cui, for supporting and sharing her enthusiasm with me over the years.

Finally, I would like to thank my parents, Wei Qian and Wei Wang, for their support and love throughout my entire life.

TABLE OF CONTENTS

LIST OF FIGURES

LIST OF TABLES

CHAPTER 1

INTRODUCTION

In nature, particles form condensed phases when the interactions between the constituents overcome the entropic effects. Different orders emerge from the competition between different components of free energy. For example, simple amphiphilic molecules can assemble into supramolecular structures with different geometries and dimensionalities. The structure of the self-assembly is sensitive to the experimental conditions, such as temperature, concentration of molecules, and salt concentration for charged amphiphilic molecules. As modern synthetic techniques enable better control of the geometry and chemistry of the building blocks, the interactions between building blocks become highly orientational and programmable. Starting from zeolite, different strategies for building well-defined porous crystalline structures have been employed, leading to tremendous success in synthesizing functional materials with desired pore sizes and chemical/physical properties. This development has led to a new field known as reticular chemistry, which includes metal-organic frameworks (MOFs), covalent organic frameworks (COFs), and hydrogen-bonded organic frameworks (HOFs). The design and synthesis of materials in reticular chemistry are based on simple geometric rules. Understanding the nucleation and growth processes remains an intriguing and challenging question in the field. Classical nucleation theory assumes that the free energy of a cluster only depends on its size:

$$\Delta G = -\frac{4}{3}\pi r^3 \Delta g_v + 4\pi r^2 \gamma \tag{1.1}$$

where δg_v represents the free energy difference per volume between the nucleated phase and the vapor phase, and γ denotes the surface tension of the interface. The clusters are hypothesized to have spherical geometry. The first work in this thesis elucidates the mechanism of nucleation and growth processes of hydrogen-bonded organic nanotubes (HONTs). This work unravels the complex thermodynamic landscapes of the nucleation and growth processes of hydrogen-bonded organic frameworks due to their network topology. Combined with experimental results, we demonstrate the sensitivity of the dominant product to the experimental conditions. This enables us to control the geometries and dimensionalities of the self-assembled structures with subtle changes in the experimental setup. This part is included in Chapter 2.

Porous materials are ideal candidates for water purification applications. Due to their tunable pore sizes and solvent processibility, COF membranes have the potential to filter pollutants and ions through a size-sieving mechanism. Nevertheless, it is challenging to synthesize free-standing single-crystalline COF membranes, calling the filtration mechanism into question. The universal belief in the filtration mechanism originates from experimental observations that larger dye molecules are stopped in the permeation process. This evidence is so convincing that people did not carefully check other mechanisms. However, our experimental collaborators found evidence that adsorption serves as an alternative mechanism for water purification. Through all-atomistic molecular simulations and theoretical arguments, I elucidate that the free energy of adsorption is mainly attributed to entropic terms—depletion interaction. According to the Asakura-Oosawa model of depletion interaction, the free energy of affinity is proportional to molecular size:

$$\Delta G = -2Nk_BTAR_s \tag{1.2}$$

where N is the concentration of water molecules, A is the effective area of the dye molecules, and R_s is the radius of water molecules. This model explains why larger dye molecules tend to have higher affinity for COF membranes. This part is included in Chapter 3.

In Chapter 4, we explore the transport of particles in networks. As previous studies reveal, when size-asymmetric colloidal particles form crystal structures, small particles can diffuse through the lattice formed by large particles at high temperatures. This phase is reminiscent of the superionic phase in ionic crystals. When a small electric field is applied to the superionic colloidal crystal, the small colloidal particles exhibit finite mobility under the electric field. When the electric field exceeds a critical value, a phenomenon named lane formation occurs. Lane formation is a nonequilibrium phase where charged particles with opposite charges spontaneously form lanes under an electric field. It is also observed when pedestrians walk in opposite directions. Previous studies on lane formation focus on size-symmetric particles. In our system, we also observe lane formation. Interestingly, when we further increase the electric field, we observe another nonequilibrium phenomenon where small particles form clusters. The large particles vibrate around their equilibrium positions and form stable wavepackets. The vibrational motion of the large particles resembles the soliton in nonlinear elastic systems. Due to the coupling between the fluid-like degrees of freedom of small particles and the vibrational motion of the lattice of large particles, a soliton-like excitation is observed far from equilibrium.

In this thesis, we explore the self-assembly, functionality, and nonequilibrium phase transition in materials with network topology. The studied systems have positional order, i.e., are crystalline. Conversely, disordered systems are ubiquitous in biological systems. It is important to understand how ionic mobility changes with network structures in polyelectrolyte gels, which are disordered

networks by nature. Collaborating with experimentalists, we obtained some preliminary results for ionic mobilities in copolyelectrolyte gels, where the porosity and charge fractions can be tuned independently. This research serves as the outlook of my PhD research and is described in Chapter 5.

CHAPTER 2

SELF-ASSEMBLY OF PHYSICAL-BONDED NETWORK STRUCTURE

Self-assembly is a process in which an ordered and condensed phase forms from a preexisting disordered system with interacting components. The components are the building blocks of the assembled structures. Self-assembly can be classified into static and dynamic self-assemblies, depending on whether the system is driven by external forces. Static self-assembly occurs when the system approaches lower free energy.

The self-assembly process can generally be divided into two steps: nucleation and growth. The nucleation process is when the free energy of the cluster increases as more components are attached to it, and the growth process is when the free energy decreases as the cluster grows larger. Therefore, the nucleation process relies on thermal fluctuations of the system and is seen as a rare event with a rate that depends on the free energy barrier:

$$R = N_S Z j \exp\left(-\frac{G^*}{kT}\right) \tag{2.1}$$

where N_S is the number of nucleation sites, Z is the Zeldovich factor, which gives the probability that a nucleus at the top of the barrier will go on to form the new phase, rather than dissolve [1]. j is the rate at which molecules attach to the nucleus. G^* denotes the free energy barrier.

In classical nucleation theory, the cluster is assumed to be spherical. This assumption of a highly isotropic structure is reasonable for isotropic interactions between building blocks, e.g., van der Waals interaction. This is also called the Fisher droplet model of condensation, named after Dr. Michael E. Fisher, who used this model to understand the critical point of a fluid [2]. The free

energy of homogeneous nucleation is:

$$\Delta G = -\frac{4}{3}\pi r^3 \Delta g_v + 4\pi r^2 \gamma \tag{2.2}$$

$-\Delta g_v$ is the difference in free energy per unit volume between the phase that nucleates and the thermodynamic phase nucleation is occurring in, and is generally negative. γ is the surface tension between the nucleus and its surroundings, which is always positive.

Classical nucleation theory is widely used to understand nucleation and growth processes. However, in systems with anisotropic interactions, the homogeneous nucleation hypothesis is broken. In systems with DNA tiles, graph theory is utilized to characterize the free energy landscapes of the clusters [3]. Thermodynamic calculations will give the most stable structure of the self-assembly process. The graph representation applies to systems with anisotropic and variant interactions, including metal-organic frameworks (MOFs), covalent organic frameworks (COFs), and the hydrogen-bonded organic frameworks (HOFs) our work focused on. In our work, we emphasize the kinetics of the self-assembly process. The kinetics of nucleation and growth is constrained by the detailed balance, thereby characterizing the local thermodynamic landscapes at the early stage of self-assembly processes. The dominant product is proven not to be the most thermodynamically stable cluster. Therefore, the self-assembly processes are kinetically controlled. The prediction of the theory is consistent with experimental observations.

The following part is submitted to JACS in 2024. Supplementary material associated with this chapter can be found in Appendix A.

Hydrogen-Bonded Fibers Assembled from Trigonal Prismatic Building Blocks

Authors: Sayantan Mahapatra[#], Dingwen Qian[#], Ruihua Zhang, Shuliang Yang, Penghao Li, Yuanning Feng, Long Zhang, Huang Wu, James S. W. Seale, Partha Jyoti Das, Prateek K. Jha, Kevin Lee Kohlstedt, M. Olvera de la Cruz, and J. Fraser Stoddart

Author contributions: M.O.d.l.C and J.F.S. designed the research; S.M. did experiments; D.Q built the theoretical model and performed simulations; S.M., D.Q., M.O.d.l.C and J.F.S. wrote the paper. This paper was submitted to JACS.

2.1 Chapter abstract

In reticular chemistry, molecular building blocks are designed to create crystalline open frameworks. A key principle of reticular chemistry is that the most symmetrical networks are the likely outcomes of reactions, particularly when highly symmetrical building blocks are involved. The strategy of synthesizing low-dimensional networks was to reduce explicitly the symmetry of the molecular building blocks. Here we report the spontaneous formation of hydrogen-bonded fibrous structures from trigonal prismatic building blocks, which were designed to form three-dimensional crystalline networks on account of their highly symmetrical structure. Utilizing different microscopic and spectroscopic techniques, we identify the structures at the early stages of the process and understand the growth mechanism. The symmetrical molecular building blocks grow preferentially in the longitudinal direction, giving rise to highly anisotropic hydrogen-bonded porous organic nanotubes. Entropy-driven anisotropic growth provides micrometer-scale unidirectional nanotubes with high porosity. Combining experimental evidence and theoretical modeling, we obtain a deep understanding of the nucleation and growth process. Our finding offers fundamental insight into molecular design of tubular structures. The nanotubes evolve further in the transverse directions to provide extended higher-order fibrous structures [nano- and microfibers], ultimately

leading to large-scale interconnected hydrogen-bonded fiber-like structures with twists and turns. Our work provides fundamental understanding and paves the way for innovative molecular designs in low-dimensional networks.

2.2 Introduction

The spontaneous assembly of molecular building blocks into intricate, porous, and interconnected hydrogen-bonded fibrous structures is of paramount importance in nature, serving essential functions in various biological systems [4–6]. This assembly process has sparked researchers' curiosity, leading to exploration of the intrinsic mechanisms and growth processes involved in the formation of these anisotropic structures [7–14]. Owing to their dynamic nature, the complex structures in the early stage of the process pose significant challenges on experimental observations and investigations [15–17]. Here, we describe in detail the experimental and theoretical investigations of a spontaneous hydrogen-bonded fibers formation process from trigonal prismatic peripherally extended triptycene (PET) molecular building blocks . The assembly first of all grows anisotropically into hydrogen-bonded organic nanotubes (HONT) and subsequently leads to large-scale interconnected and intertwined fibrous structures. We demonstrate a phenomenon where hydrogen-bonded fibers spontaneously emerge from H_6PET (peripherally functionalized with six aryl-carboxyl groups, **Figure 2.1a**) trigonal prismatic molecular building blocks in acetone under ambient conditions and manage to characterize the structures of the early stages of the process and growth trajectories. The symmetrical molecular linkers were primarily designed for applications in hydrogen-bonded organic frameworks (HOFs) and metal-organic frameworks (MOFs) involving complex three-dimensional (3D) interpenetrated structures [18–20], aimed at secure and efficient storage of methane and hydrogen gases [21], as well as possessing an exceptional water uptake capacity [22]. Herein, by combining the molecular design, theoretical modeling with atomic force

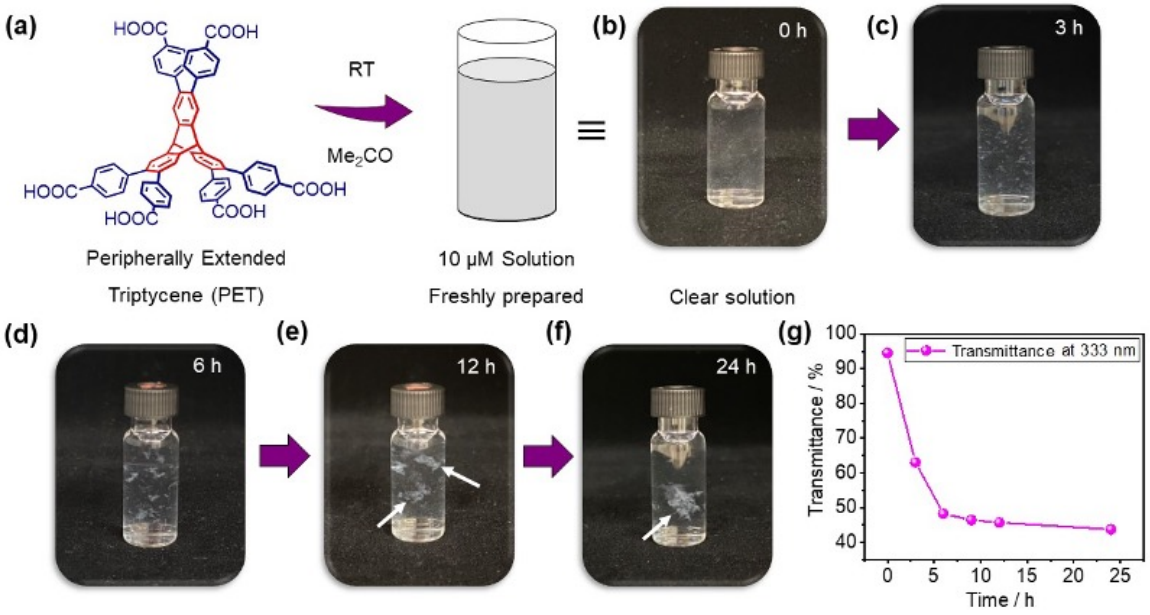

Figure 2.1: Evolution of hydrogen-bonded fiber structures in Me_2CO under ambient conditions. **(a)** Structural formula of H_6PET, showing trigonal prism conformation. **(b)–(f)** Images of the solution at different time intervals (0→3→6→9→12→24 h). The large-scale microfibers are indicated by a few white arrows. **(g)** Variation in transmittance (%) [at 333 nm] with respect to time.

microscopy (AFM) and transmission electron microscopy (TEM) results, we have been able to image successfully the unidirectional HONTs with a hollow interior at the early stage of the process, providing a non-interpenetrated structure. Furthermore, our multiscale simulations predict the formation of a growth seed that grows longitudinally into a highly anisotropic nanotube framework because of entropy loss of restricted arms. The nanotubes grow in the transverse direction into large-scale porous interconnected micro-fibrous structures with twists and turns, offering key details about the growth mechanism and trajectories.

Our results reveal how the hydrogen-bonded interconnected fibers grow spontaneously from trigonal prismatic molecular building blocks, with potential applications in ion-sensing, molecular

inclusion, separation, catalysis, and drug delivery as well as in transmembrane transport [23]. Additionally, the phase diagram elucidates the significant impact of experimental conditions, such as solvent or molecule choice, which play a pivotal role in either stabilizing or destabilizing both the bound and unbound states of the supramolecular structures [24].

2.3 Results and discussion

2.3.1 Evolution of Fiber Structures.

The synthesis of the H_6PET was achieved by repeating the methods previously documented in published literature [25]. Adding H_6PET to acetone ($\sim$1mM) resulted (**Figure A.1a**) in a turbid solution characterized by abundant fiber formations. In order to investigate the entire process of fiber formation thoroughly and uncover the intricate microscopic mechanisms involved, we prepared freshly a low-concentration solution ($\sim$10 μM), preventing rapid fiber formation based on concentration-dependent observations. This solution (**Figure 2.1**) was designated as the starting point (0 hours), and the evolution of fiber formation was observed over a period of 24 hours. Initially, the solution appears as clear (at 0 hours, **Figure 2.1b**), but within 3 hours, fibrous structures started to emerge (**Figure 2.1c)** from multiple nucleation sites (visible to the naked eye). During the period of 3 to 24 hours, the fibrous structures gathered progressively and aggregated into a singular large-scale fiber structure (**Figures 2.1d–f**). UV/Visible spectroscopy was employed to examine the transparency of the solution at different time intervals. **Figure 2.1g** represents the transmittance of the light at 333 nm. Within 6 hours, the transmittance of the solution exhibited a significant decline (**Figure 2.1g**), dropping from 94.6% to 48.3%. This decrease in light scattering can be attributed (**Figures 2.1d–f**) to the aggregation of the fibers within the solution. Subsequently, the fibrous structures reach dynamic equilibrium slowly with the free monomers in the surrounding solution, as evidenced by a change in transmittance from 48.3% to 43.7% over the

next 18-hour duration. The transmittance spectrum (**Figure 2.1g**) clearly illustrates that the transmittance diminishes as the fibrous structures increase and aggregate. Conversely, the refractive index of the solution exhibits (**Figure A.2d**) an increment over time.

2.3.2 Characterization of the Structure at the Early Stage

2.3.2.1 Atomic Force Microscopy (AFM).

In order to identify the elementary steps and the detailed structure, $\sim$6 μL freshly prepared (i.e., 0 h, for more details, see **Supplementary Section 1**) solution ($\sim$10 μM) was dropcasted onto a highly oriented pyrolytic graphite (HOPG) surface under ambient conditions and subjected to AFM analysis. A large-scale AFM image (**Figure 2.2a**) is reveals the existence of elongated tube-like structures oriented in a single direction [up to several micrometers in length]. The AFM height profile (**Figures 2.2b** and **2.2d**) shows a uniform diameter of $\sim$4.75 $\pm$ 0.2 nm for an isolated structure. The AFM phase profile of the same tube-like structure, however, shows (**Figures 2.2c** and **2.2e**) a dip in the center. This dip in the AFM phase image suggests the presence of hollow tubes [26, 27]. Based on tip-sample interactions, one can correlate the phase shift directly to the dissipation energy (E_d) in the tip-sample contact [28]. While the accurate interpretation of phase images remains challenging, the phase shift in the tip oscillation establishes a link between the dynamic behavior of the cantilever and the interaction between the tip and sample. The phase variation $(\delta\phi)$ can be related to the variation in dissipation energy (δE) as [29]:

$$P\delta E = A_0^2 \left[\cos\phi_0 \left(\delta a\right) - 2a_0 \left(\delta a\right) - a_0 \sin\phi_0 \left(\delta\phi\right)\right] \tag{2.3}$$

where P is the cantilever-related constant, A_0 is free amplitude, ϕ_0 is phase shift, and δa is the error image. For more details, see **Supplementary Section 3**.

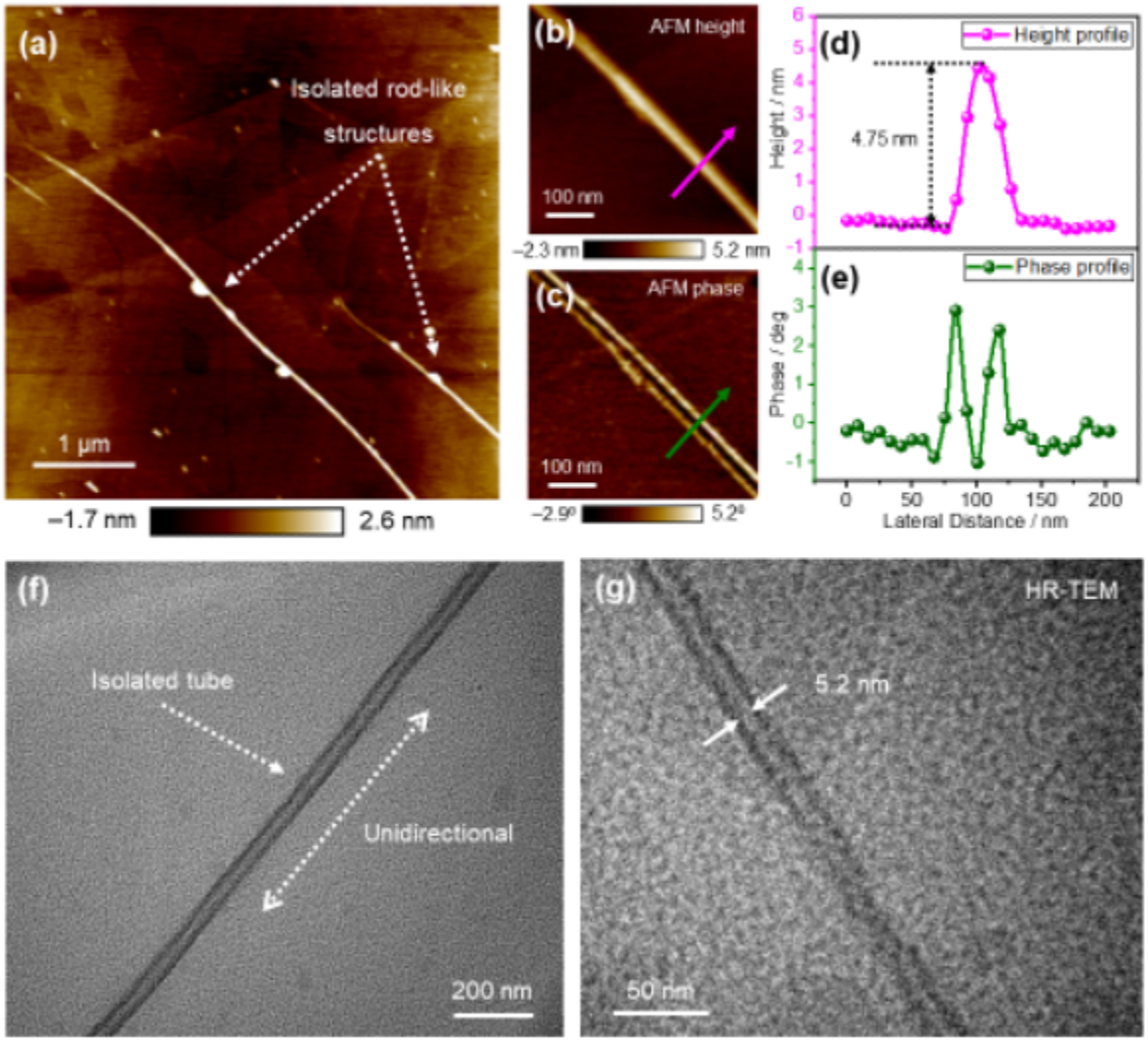

Figure 2.2: Characterization of nucleation and growth of hydrogen-bonded structures at an early stage. (a) Large-scale AFM image, showing the existence of isolated rod-like structures. (b)–(c) Zoom-in AFM Height and Phase images of individual nanotube, respectively. (d)-(e) AFM Height and Phase profile of individual nanotube along the color-assigned arrows, respectively. (f) TEM Image shows the presence of unidirectional tube-like structures of H_6PET. (g) High-resolution TEM illustrates hollow tubular structures of H_6PET with an interior diameter of ∼5.20 nm for an individual nanotube.

Hence, the interactions between the tip and sample can be linked to the material properties, charge distribution, or sample conformation (geometry). The phase line profile indicates (**Figure 2.2e**) an average delay of $+2.75 \pm 0.25^{\circ}$ in the phase shift on the side walls compared to the HOPG surface. Conversely, the central part of the tube, situated between the side walls, exhibits an advancement of -1°. This observation confirms the similarity in tip-sample interactions on the side walls, while revealing a distinct behavior in the central region. This behavior is understandable given the fact that the molecular conformation is anticipated to differ in the central region compared to both sidewalls, where the molecular geometry is similar (**Figure A.3**). This disparity in molecular arrangement contributes to variations in the tip-sample interactions.

2.3.2.2 Transmission Electron Microscopy (TEM).

In search of more evidence to support the nanotube observation, structural morphology was visualized by TEM (**Figures 2.2f–g**). For more details, see **Supplementary Section 4**. The high resolution-TEM analysis (**Figure 2.2g**) corroborates the presence of hollow tubular structures with an interior diameter of $\sim$5.20 $\pm$ 0.02 nm for individual nanotubes. Moreover, nanotubes are also observed (**Figure A.4d**) to exhibit a unidirectional nature of up to several micrometers in length. These findings align closely with the results obtained from AFM, providing further confirmation of the presence of hydrogen-bonded organic nanotubes (HONTs). Based on these experimental results, we consider the formation of hydrogen-bonded nanotubes as the preliminary nucleation and growth step in the fibers formation process. The spatial orientation of carboxylic acid functional groups in trigonal prismatic H_6PET building blocks (dihedral angle of $\sim$120), as well as the highly directional nature of hydrogen bonding facilitate the growth of the hydrogen-bonded framework in one dimension. Moreover, our AFM and TEM findings exhibit similarities to a recent study conducted by Koner *et al.*, [30] in which the authors designed covalent organic nanotubes (CONTs)

using a tetratopic amine-functionalized triptycene and a linear dialdehyde as the building blocks using an aldehyde-amine condensation process. It is also worth mentioning that, in addition to the nanotubes, a few higher-order structures are also observable when examining the freshly prepared solution, i.e., 0 hours under TEM analysis (**Figures A.4d-f**). A detailed discussion regarding these structures will be provided later.

2.3.2.3 Proposed Hydrogen-Bonded Organic Nanotube (HONT) Model.

Drawing upon the AFM and TEM results, we have proposed (**Figure 2.3a**) a schematic representation of the anisotropic one-dimensional nanotube structure, originating from trigonal prism-based units. Among the six carboxylic acid functional groups, four of them engage in robust cross-linked hydrogen bonding interactions to form a one-dimensional tube structure. The other two acidic groups, however, remain free and available for additional structural extensions. The totality of the AFM and TEM evidence makes any other contrary model unlikely. This tentative nanotube model suggests (**Figure 2.3b**) the diameter of the tube is $\sim$5.4 nm, which is in line with the TEM and AFM measurements. Moreover, our tentative nanotube model indicates the presence of a hollow tubular channel whose pore size has a diameter of $\sim$3.6 nm ($\sim$36 Å) and extends along the entire length of the HONT (**Figure 2.3c** and **Figure A.6b**). In support of our hypothesis, the porosity of the hydrogen-bonded fibers was assessed through the measurement of the nitrogen (N_2) adsorption isotherm as isolating the individual HONTs proved impossible because of their spontaneous transformation into the large-scale micro-fibers. The pore size distribution of the fibers aligns well (**Figure A.5b**) with the predicted one-dimensional tube model. The porosity measurements also rule out the possibility of interpenetrated structures in the fibers, which would shrink the pore size significantly. Furthermore, the observed similarity in pore size distribution across both the nanotube and large-scale micro-fibrous structures (i.e., higher-order structures) suggests the possi-

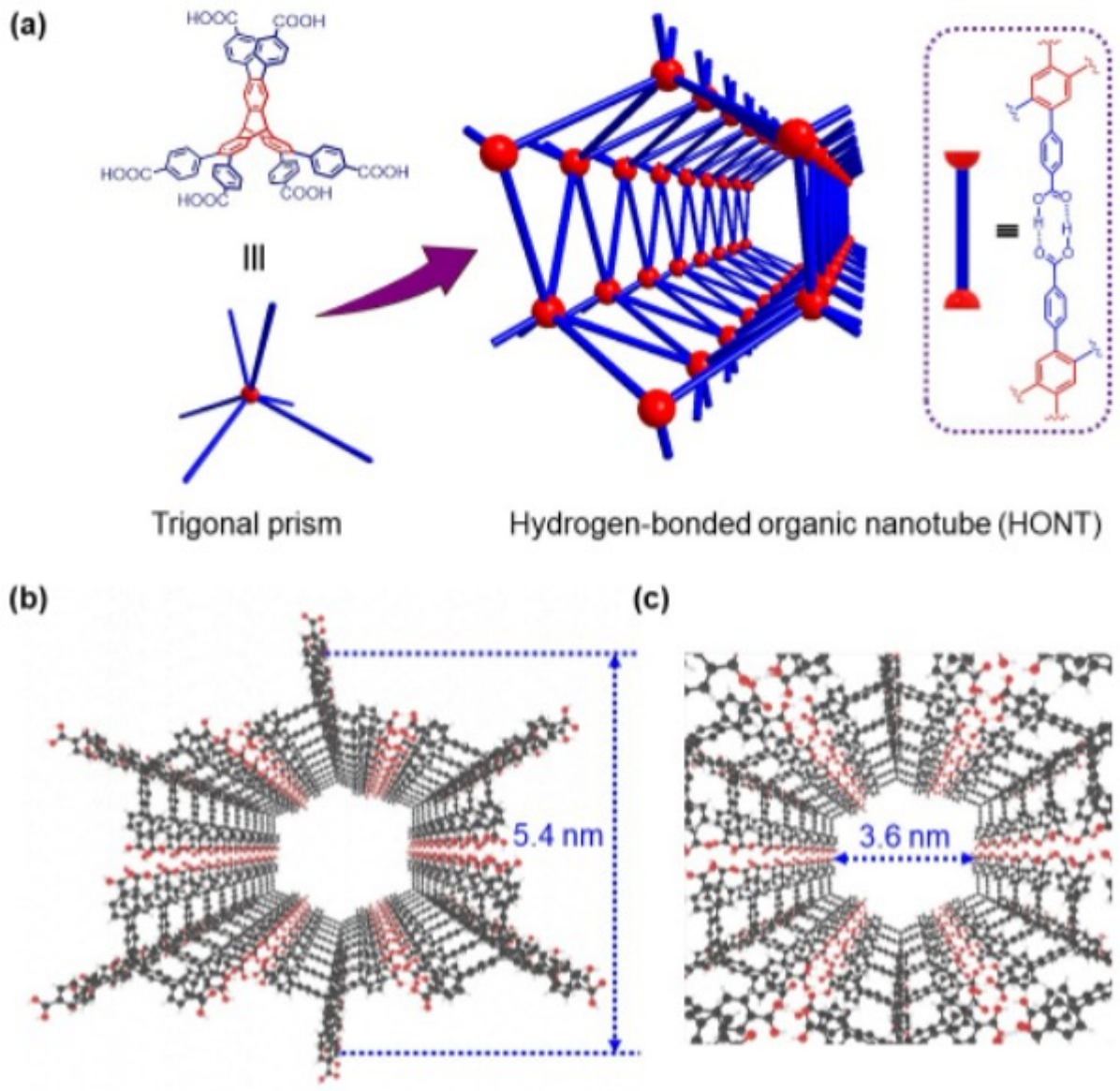

Figure 2.3: Proposed hydrogen-bonded organic nanotube (HONT) model. (a) Structural formula of H_6PET and its graphical representation as a trigonal prism. Transformation of the trigonal prismatic building blocks into nanotubes. (inset) The primary intermolecular force stabilizing the framework is the hydrogen bonding associated with the carboxyl dimers. (b) Model of proposed nanotube, showing the diameter of the tube to be $\sim$5.4 nm. (c) Inside view of proposed nanotube, showing the hollow interior with $\sim$3.6 nm pore size.

bility of assembly process during the growth of fibers (final stage) from one-dimensional nanotubes (early stage).

2.3.3 Theoretical Investigation of the HONT Formation at the Early Stage.

Triptycene (D_{3h} symmetry) and o-terphenyl components (in the H_6PET structure) are known [25] for suppressing face-to-face π-stacking interactions. Consequently, we anticipate that the primary intermolecular force governing the framework will be the hydrogen bonding associated with the carboxyl dimers [25, 31]. It remains, however, puzzling to decipher why the molecules grow preferentially in a longitudinal direction (anisotropic growth) for the formation of a rigid nanotube framework in acetone at the early stage. In order to gain deeper insights into the nucleation mechanism and the influence of the solvent medium during the early stages of the fiber formation process, we built a phenomenological model based on molecular dynamics and kinetic Monte Carlo simulations.

2.3.3.1 The Internal Degrees of Freedom of Arms and Steric Effect.

The H_6PET molecule features six identical arms, each terminated with carboxylic groups. Each arm is connected to the core by a single carbon-carbon bond that can rotate as shown in **Figure 2.4a**. In the molecular dynamics simulation, it is notable that each arm exhibits four peaks in its density distribution of dihedral angles, a pattern consistent with the biphenyl dihedral potential landscape (**Figure A.7a**). Additionally, we also observe that the dihedral angles of the arms are not independent, forming three correlated groups among the six arms. Because of steric effects (**Figure 2.4b**), the arms within each arm group tend to adopt either the same conformation or conformations that differ by π radians. As a result, each pair of arms exhibits eight stable configurations (**Figure 2.4b**) with the bonding of one arm leading to the restriction of motion of a pair of arms (**Figures**

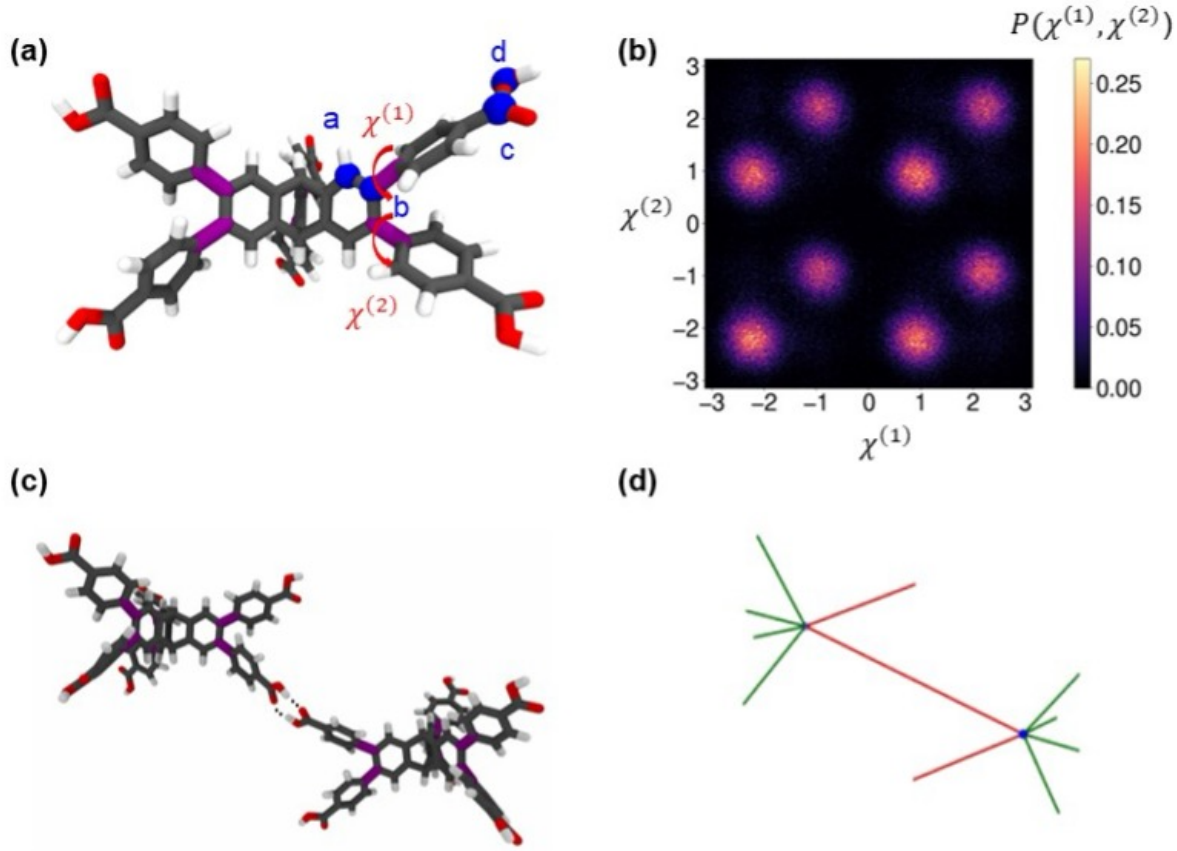

Figure 2.4: Illustration of the structure of H_6PET monomer and steric effect between the arms. (a) Molecular structure of the H_6PET monomer. The flexible single bonds are marked in purple. The four blue atoms define the dihedral angles of the arm: $\chi = \arctan 2[\overrightarrow{bc} \cdot ((\overrightarrow{ab} \times \overrightarrow{bc}) \times (\overrightarrow{bc} \times \overrightarrow{cd}), |\overrightarrow{bc}|(\overrightarrow{ab} \times \overrightarrow{bc}) \cdot (\overrightarrow{bc} \times \overrightarrow{cd})]$. The dihedral angles of one correlated arm group labeled by red curved arrows. (b) The statistical distribution of the dihedral angles of correlated arm groups when the arms are not bonded. This distribution is sampled from 100 H_6PET molecules over 800 timesteps with intervals of 0.1 ns. (c) Schematic representation of hydrogen bonding between H_6PET monomers. The motion of the bonded arms and their neighbors are restricted because of the hydrogen bonds and steric interactions. (d) Simplified representation of the hydrogen-bonded H_6PET dimer. The green arms are free to rotate, while the red arms are restricted.

2.4c–d). The steric effect reduces significantly the molecule's entropy when bonds are formed. Furthermore, we will show that the entropy loss of restricted arms serves as the origin of anisotropy in growth directions.

2.3.3.2 The Graph Representation of the Assembly.

Since there are isomers of H_6PET assemblies when the degree of polymerization is larger than 2, it is convenient to use graphs to represent assembled fragments [3]. The vertices of the graph represent monomers and the edges represent double hydrogen bonds between carboxylic groups. Any fragment can be represented by a graph with N_V vertices and N_E edges, which is denoted by g_{N_V,N_E} (**Figure A.7b**). The monomer is denoted by$g_{1,0}$ or m for convenience. From the graph, we can also obtain the number of arms that are restricted, denoted by N_A.

The reversible reaction of N_V monomers assembled into an assembled fragment represented by g_{N_V,N_E} is:

$$N_V m \rightleftharpoons g_{N_V,N_E} \tag{2.4}$$

We propose a phenomenological free energy of this reaction under standard conditions:

$$\Delta G^{\circ}\left(g_{N_V,N_E}\right) = N_E \Delta H_d^{\circ} - \left(N_V - 1\right) T \Delta S_m^{\circ} - N_A T \Delta S_a^{\circ} \tag{2.5}$$

where ΔH_d° denotes the enthalpy gain of forming a double hydrogen bond between the arms. ΔS_m° represent the loss of entropy due to the restriction of rigid body motion of one monomer in the assembled fragment. N_A is the number of restricted arms and ΔS_a° denotes the entropy loss due to the restriction of arm rotation. The free energies of the fragments depend not only on their sizes, but also on their structures, which are fully encoded in their graph representations.

In the case of tree-type graphs, the fragments satisfy $N_E = N_V - 1$. The free energy returns to

the free energy change of cylindrical micelles [32]:

$$\begin{aligned}\Delta G^{\circ}\left(g_{N_V,N_E}\right) &= \left(N_V-1\right)\Delta H_d^{\circ} - \left(N_V-1\right)T\Delta S_m^{\circ} - 4\left(N_V-1\right)T\Delta S_a^{\circ} \\ &= \left(N_V-1\right)\left[\left(\Delta H_d^{\circ} - T\Delta S_m^{\circ}\right) - 4T\Delta S_a^{\circ}\right] \\ &= \left(N_V-1\right)\Delta\mu_d^{\circ}\end{aligned} \tag{2.6}$$

where $\Delta\mu_d^{\circ} = \Delta H_d^{\circ} - T\Delta S_m^{\circ} - 4T\Delta S_a^{\circ}$ is the chemical potential change of a monomer attaching to a tree graph under standard conditions. If we only consider the formation of tree-type graphs, the critical concentration [32] is $[m_{c1}] = \exp\left(\frac{\Delta\mu_d^{\circ}}{kT}\right)$. If the concentration of monomers $[m_0]$ exceeds this critical concentration, the self-assembly process is diffusion-limited, and the anisotropy is minimal. Therefore, the formation of nanotube falls into the regime where $[m_0] < [m_{c1}]$. In the regime where $[m_0] < [m_{c1}]$, there is a free energy barrier for nucleation. We bypass the nucleation process by selecting a short nanotube as the growth seed. The short nanotube is selected because the attachment of one monomer to the short nanotube results in the formation of two bonds, thereby stabilizing the fragment through the creation of an additional bond. The growth process following the formation of the seed is analyzed using kinetic Monte Carlo (kMC) simulations.

2.3.3.3 The Kinetic Monte Carlo (kMC) Simulation of Self-Assembly.

In our kMC simulation, we model the process where a single monomer is either attached to or removed from a growing assembly on a fixed lattice. The starting point for our simulation is a short nanotube composed of 36 monomers. This simulation is designed to model the early stage of self-assembly of an aggregate that is in contact with a reservoir of constant concentration of monomers. That is, we are working in a grand canonical ensemble [33, 34]. Here, the concentration of monomers is set equal to the initial concentration $[m] = [m_0]$, mirroring the conditions at

the onset of self-assembly.

We describe the attachment or detachment of a monomer from the assembly using the following reaction formula:

$$m + g_{N_V,N_E} \rightleftharpoons g_{N_V+1,N'_E} \tag{2.7}$$

The difference in chemical potential ($\Delta\mu^i$) between the monomer in the assembly at a specific site i and in the reservoir depends on the chemical potential difference under standard condition and the concentration of the monomers:

$$\Delta\mu^i = \Delta\mu^{i,\circ} - kTln\left[m\right] = \Delta N_E^i \Delta H_d^\circ - T\Delta S_m^\circ - \Delta N_A^i T\Delta S_a^\circ - kTln\left[m_0\right]) \tag{2.8}$$

In this formula, ΔN_E^i and ΔN_A^i denote the number of new bonds formed and the number of arms restricted, respectively, when a monomer is added to the assembly at the site i. These variables depend on how the monomer connects to the rest of the structure.

The ratio between the rates of adding and removing a monomer, r_{on}^i and r_{off}^i, is dependent on the chemical potential difference, respecting the law of detailed balance:

$$\begin{aligned} \frac{r_{on}^i}{r_{off}^i} &= \exp\left[-\frac{\Delta\mu^i}{kT}\right] = [m_0]\exp\left[-\frac{\Delta\mu^{i,\circ}}{kT}\right] \\ &= [m_0]\exp\left[\frac{\Delta S_m^\circ}{k}\right]\exp\left[\frac{-\Delta N_E^i \Delta H_d^\circ}{kT} + \frac{\Delta N_A^i \Delta S_a^\circ}{k}\right] \end{aligned} \tag{2.9}$$

We define the time unit τ in our simulation as the average time required for a monomer to locate an attachable site. The time unit is estimated to be in the order of milliseconds based on the diffusion

coefficient of the PET molecules and the rotational entropy change. See **Supplementary Section 6**. The achievable simulation time is thus a few orders of magnitude longer than molecular dynamics and canonical kinetic Monte Carlo simulations. Therefore, the grand canonical kinetic Monte Carlo simulation is appropriate for modeling the self-assembly process of hydrogen bonded organic nanotubes. The rate of monomer addition is inversely related to the rate of finding an attachable site and the probability of arms alignment, given by $r_{on}^{i} = (\frac{1}{4})^{\Delta N_E^i} \frac{1}{\tau}$. The rate of monomer removal events follows from Eq. (6), $r_{off}^{i} = r_{on}^{i} \exp\left[\frac{\Delta\mu^i}{kT}\right]$. In one Monte Carlo step, after building the lists of the rate of all insertion and removal events, we implement the Bortz-Kalos-Lebowitz (BKL) algorithm [35] to choose one event randomly to execute and update the state of the system. The system evolves in the fragment space and there is no correlation between successive events (**Figure A.8**). The total Monte Carlo steps for each simulation is set to be 10^4. In order to obtain statistically meaningful results and estimation of errors, simulations with the same parameters are repeated 10 times. The constant part in the chemical potential difference, $[m_0] \exp\left[\frac{\Delta S_m^\circ}{k}\right]$, is set equal to $\exp[-23]$ based on an estimation from density functional theory (DFT) calculations and the concentration of the monomers in experiments. For more details, see **Supplementary Section 6**. The free parameters in our simulations are the hydrogen bonding strength $|\Delta H_d^\circ|$ and the entropy loss of restricted arms $|\Delta S_a^\circ|$. By performing kMC simulations spanning the parameter space, we observe three different phenomena (**Figure 2.5a**): no assembly, formation of tubular structures, and formation of three-dimensional structures. The system is classified as no assembly when it dissembles to one monomer and the simulation stops. Then we measure the shape anisotropy of the systems with continuous growth and classify them as tubular structures or three-dimensional structures based on the criterion (**Figure A.7c**) that the shape anisotropy of a tubular structure is larger than 0.2. As the hydrogen bond strength increases, the system progresses from a state of no assembly to the formation of tubular structures, and subsequently advances to the development

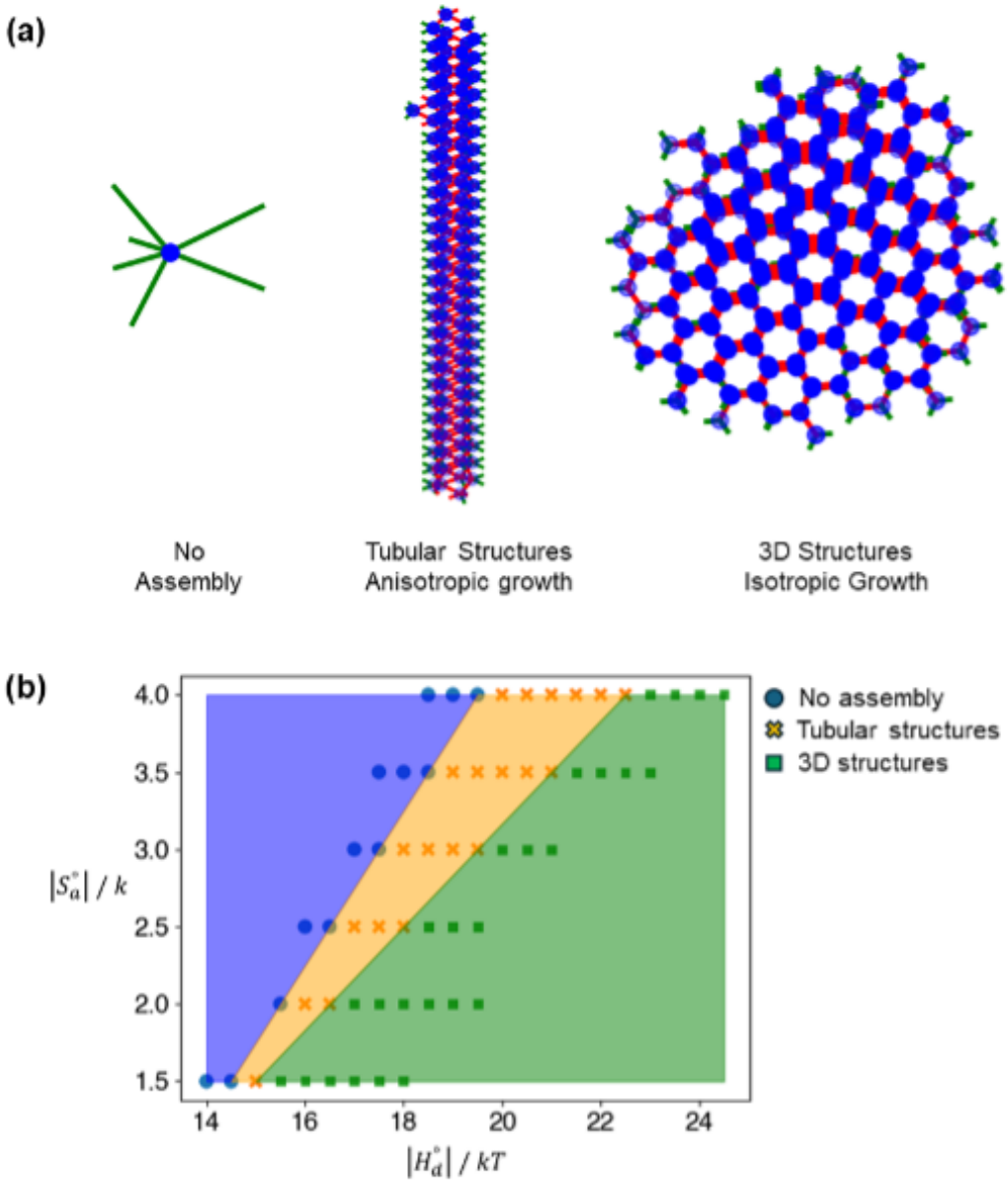

Figure 2.5: Growth regimes predicted by kinetic Monte Carlo simulations. (a) Snapshots from kinetic Monte Carlo simulations corresponding to different phenomena (left) no-assembly, (mid) highly anisotropic tubular structures (nanotubes) resulting in longitudinal growth, and (right) three-dimensional (3D) structure resulting in transverse growth. The green arms are free to rotate, the motion of the red arms are restricted because of steric interactions. (b) The phase diagram of H_6PET assembled at an early stage. The dots represent simulation results from kinetic Monte Carlo simulations. The parameter space is divided into three colored regions based on the data points. Inside the tubular structure region, the closer to the no assembly region, the more anisotropic the structure becomes.

of three-dimensional structures (**Figure 2.5b**). As the entropy of restricted arms increases, the range of tubular structures formation becomes wider. This trend confirms that the entropy of restricted arms is the origin of the anisotropy in the growth direction, i.e., nanotube formation. In the following Section, we are going to explain the growth anisotropy in terms of free energy landscapes of different pathways of growths.

2.3.3.4 Kinetic Growth Pathways and Free Energy Landscapes.

The free energy of fragment g_{N_V,N_E} is defined as [2, 3, 36, 37]

$$\Delta G\left(g_{N_V,N_E}\right) = \Delta G^{\circ}\left(g_{N_V,N_E}\right) - \left(N_V - 1\right) kTln[m_0] \tag{2.10}$$

It is a natural extension of the Gibbs free energy of cluster formation in classical nucleation theory. For more details, see **Supplementary Section 6**. In **Figure 2.6a**, we construct the kinetic growth paths in longitudinal and transverse directions. In **Figure 2.6b**, we illustrate the corresponding free energy landscapes of these two pathways within the regime of nanotube formation. The free energy keeps decreasing as the nanotube grows longitudinally, while there are a few free energy barriers as the nanotube grows transversely. The origin of the difference in the free energy landscapes is a result of the different numbers of arms restricted when a monomer is attached to different sites on the assembly.

The chemical potential change of attaching one monomer on top (denoted as t) is $\Delta\mu_t = 2\Delta H_d^{\circ} - TS_m^{\circ} - kTln[m_0] - 4T\Delta S_a^{\circ}$, where four arms are restricted during the process. The chemical potential change of an individual monomer attached on the side (denoted as s) is $\Delta\mu_s = 2\Delta H_d^{\circ} - T\Delta S_m^{\circ} - kTln[m_0] - 6T\Delta S_a^{\circ}$, where six arms are restricted during the process. Therefore, the first monomer is more stable on the top than on the side. When $\Delta\mu_t < 0$ and $\Delta\mu_s > 0$,

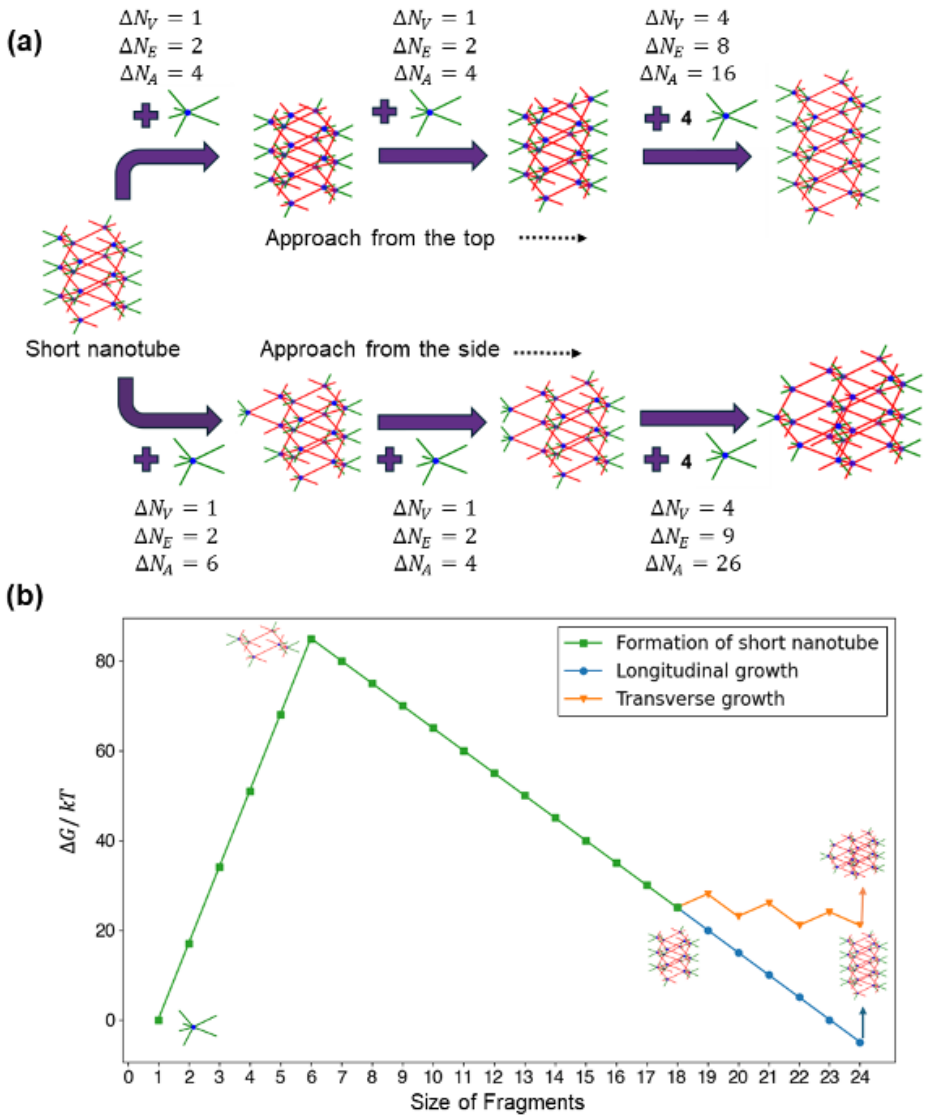

Figure 2.6: Energetics of nanotube growth at an early stage. (a) Schematic representation of kinetic growth paths in longitudinal (top) and transverse (bottom) directions. The cores of monomers are represented by blue vertices. Bonded arms are represented by red edges connecting the vertices. The unbonded arms are also shown as short lines in the graphs for the illustration of restricted arms. Restricted unbonded arms are also colored red, while free unbonded arms are colored green. ΔN_V, ΔN_E, and ΔN_A represents the changes of number of vertices, edges, and restricted arms at each step. (b) Free energy landscape of different pathways of nucleation and growth when nanotube is formed in the kKinetic Monte Carlo simulation. The hydrogen bond strength $|\Delta H_d^\circ| = 22kT$ and the entropy loss of restricted arms $|\Delta S_a^\circ| = 4k$.

there is no free energy barrier in the longitudinal growth pathway, while there exist free energy barriers in the transverse growth pathway. Therefore, the growth in the longitudinal direction is diffusion-limited and much faster than the growth in the transverse direction, leading to the formation of anisotropic tubular structures. The free energy landscapes in the regime of no assembly and formation of 3D structures are demonstrated in **Figure A.10**.

In the classical nucleation theory (CNT), the Gibbs free energy change (ΔG) of the formation of a highly symmetric nucleus can be written as [38]:

$$\Delta G = -v\Delta g_v + A\gamma \tag{2.11}$$

where v represents the volume of the nucleus, Δg_v signifies the Gibbs free energy difference per unit volume between the parent and product phases, A is the area of the interface formed during the nucleation process, and γ represents the interfacial free energy per unit area of the created interface. ΔG goes through an energy barrier as a function of nucleus size.

Alternatively, the nucleation and growth process in our model cannot be described by the classical free energy of nucleation that is only dependent on the nucleus size [39]. The free energies of the fragments in our system are highly dependent on the geometry, especially during the early stage of nucleation and growth. Numerous pathways of nucleation and growth exist, each characterized by its unique free energy landscape. The dominance of a particular product arises from the competition among these diverse pathways [40–43]. The relative nucleation rate of these pathways is notably sensitive to the interaction strength. Hence, it is possible to control the dominant product by carefully tuning the experimental conditions [44]. In the experiments, the entropy of restricted arms and hydrogen bond strength can be tuned by varying the arm length of individual monomers and solvent polarity. Our hypothesis can be validated by controlled experiments, which include utilizing H_6PET monomers with varying arm lengths (**Figure A.11**) and employing different sol-

vent mixtures as reported in our previous work [25]. We hope that the knowledge acquired from this investigation will contribute to deepening our understanding of the significance of competitions between different pathways of self-assembly, inspiring new strategies of forming networks with desired anisotropy [45–47].

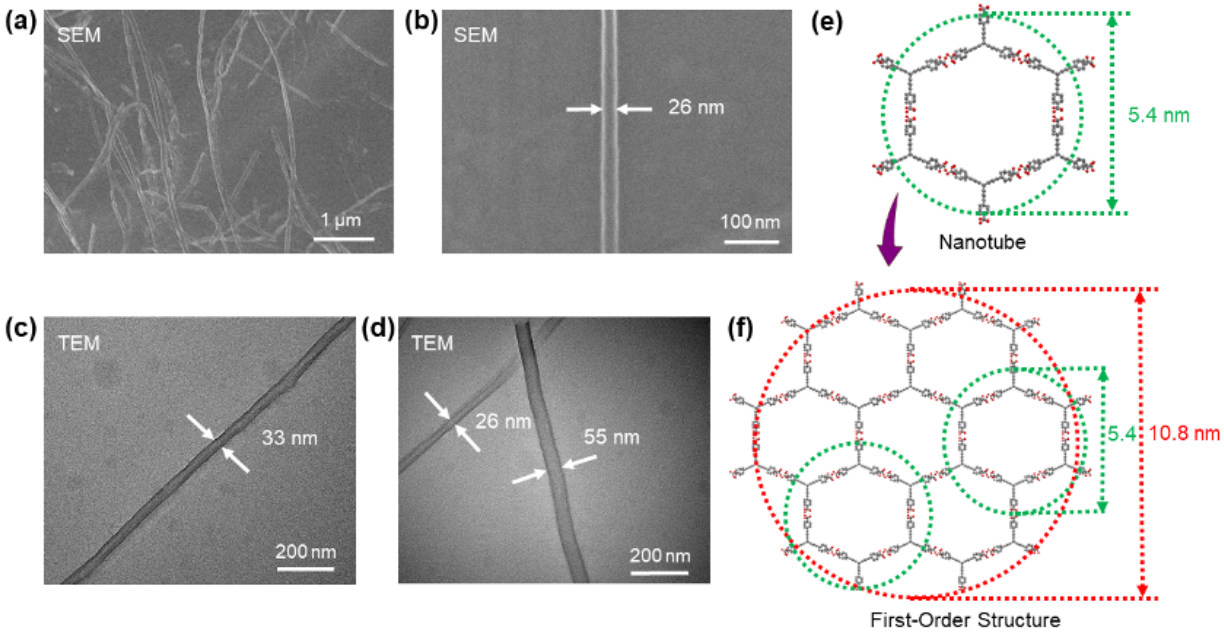

Figure 2.7: Higher-order structures. (a) large-scale SEM image of 6-hours solution (dropcasted from clear portion), showing abundance of nanofibers. (b) Zoom-in SEM image of nanofiber, depicting unidirectional nature with ∼26 nm width. (c)–(d) Corresponding TEM images of the nanofibers with different widths. (e)–(f) Proposed model of first-order structure from the nanotube.

2.3.4 Growth Mechanism of Hydrogen-Bonded Fibers.

Following the structural identification of the early nucleation and growth stage, we proceeded to explore the growth mechanism and trajectories of the hydrogen-bonded fibrous structure formation process. After 3 hours and 6 hours, several fiber structures become apparent. Consequently, we

opted to examine (**Figure A.1f**) the remaining clear part of the solution in more detail. Analysis conducted using SEM reveals (**Figures 2.7a–b**) the presence of abundant nanofibers, which are classified as higher-order structures, exhibiting a width ranging from 20 to 170 nm. Furthermore, the examination of these higher-order structures through TEM, i.e., structures depicted in **Figure 2.7c** with a width of $\sim$33 nm and **Figure 2.7d** with a width of $\sim$26 nm and $\sim$55 nm provides insights into the tubular morphology of the nanofibers. Based on these experimental observations, we put forward a tentative model for higher-order structures. Once the rigid HONT framework (foundational framework, 0^{th}-order structure, **Figure 2.7e**) is formed through the longitudinal growth of H_6PET molecules (at the early stage), the following higher-order structure (defined as first-order structure) can be generated through a self-assembly process in the transverse directions, as depicted in **Figure 2.7f**. The first-order structure has the potential to further develop into higher-order structures, including the second, third, and subsequent orders, eventually resulting in the formation of large-scale (micrometer-width) fibrous structures. Although speculative, the proposed model of higher-order structures is consistent (**Figure A.13**) with the pore size distribution result in the final fibrous structures. Considering the diameter of the one-dimensional HONT, which measures $\sim$5.4 nm, the predicted diameter of the first-order structures would be $\sim$10.8 nm (**Figures 2.7e–f**). Through AFM analysis, we visualized the first-order structure, which exhibits (**Figure A.14**) a diameter of $\sim$10.72 nm. This observation further serves as a validation of our proposed model.

The diameter (D_n in nm) of the higher-order structures (n^{th}-order) roughly follows a simple equation:

$$D_n \approx (n+1) \times 5.4 \tag{2.12}$$

Therefore, nanofibers with a width of $\sim$26 nm, $\sim$33 nm, and $\sim$55 nm can be hypothesized as 4^{th}-order, 5^{th}-order, and 9^{th}-order structures, respectively. Moreover, the high-order structures

exhibit predominantly a unidirectional nature, aligning well with the pattern observed in the one-directional nanotube structures. This observation strongly suggests that the high-order structures originate from the nanotubes. The population of nanofibers decreased relatively (**Figure A.12c**) after 12 hours. With an increasing number of prominent large-scale fibers (micrometer-width) becoming apparent at this point in time, it is reasonable to anticipate that the nanofibers have undergone a transformation into higher-order [micrometer (μm) width, referred to as microfibers] structures through a similar self-assembly process. Following a span of 24 hours, the occurrence of small-scale nanofiber structures (ranging from 20 to 150 nm) becomes infrequent, indicating that a significant portion of the nanofibers have been transformed into larger-scale fibers (μm-width) with the system reaching a dynamic equilibrium. **Figure 2.8a** illustrates the visualization of the large-scale microfibers using SEM analysis. The image portrays an interconnected structure composed of 4–5 fibers, each with a width ranging from 10–15 μm. Upon closer examination, it becomes apparent that each fiber exhibits numerous line-like features along its wall (**Figure 2.8a**). Moreover, the self-assembly process reveals the presence of intertwined structures exhibiting twists (**Figure 2.8b**) and turns (**Figure 2.8c**). The substantial growth in fiber width stimulates a degree of flexibility, encouraging the development of an intertwined arrangement. We would like to note that AFM and TEM may not distinctly detect these large-scale fiber aggregates (μm-width) which is likely due to from AFM's poor contrast, TEM's limitation in resolving very thick nanostructures, and the necessity for both techniques to focus on highly dispersed sample regions. The final hydrogen-bonded fibrous structures remain unchanged in solution for several months.

2.4 CONCLUSION

We have explored the growth mechanism and trajectory underlying the spontaneous formation of hydrogen-bonded fibers from symmetric trigonal prismatic molecular building blocks under

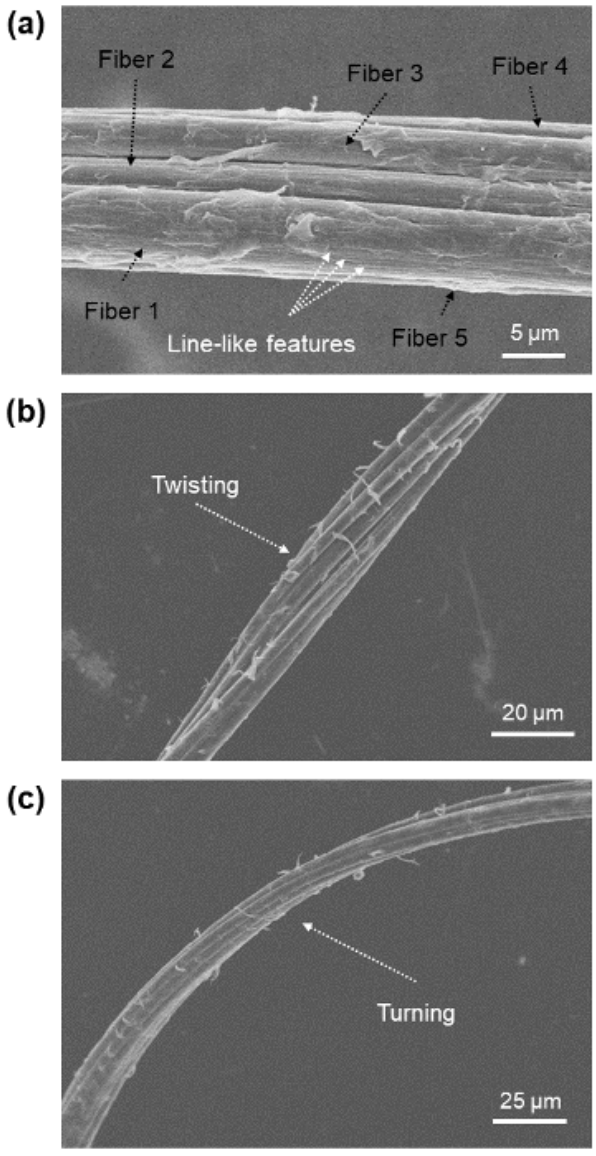

Figure 2.8: (a) SEM image of a few microfibers (width ranging from 10–15 µm) assembly. Line-like features are visible on the walls (marked). Substantial growth in fiber width induces a degree of flexibility, which introduces (b) twists and (c) turns.

ambient conditions. At the early stage of the process, the individual H_6PET molecules prefer an orientational attachment to form one-directional nanotube structure because of anisotropy in growth kinetics. Moreover, our theoretical model hypothesizes the formation of a short nanotube as growth seed which undergoes growth preferably in longitudinal direction as a result of entropy loss of restricted arms, resulting in the development of nanotube framework. As time progresses, the unidirectional nanotube tends to undergo thicker growth (transverse growth), giving rise to higher-order structures (μm-width structures). This sequential progression ultimately leads to the formation of large-scale interconnected and intertwined fibers with twists and turns. **Figure A.15** illustrates the evolution of the hydrogen-bonded fibrous structure formation starting from H_6PET molecular units. Our study sheds light on the complexity and importance of the free energy landscapes of network structures. A subtle change in experimental conditions can alter the free energy landscapes profoundly, thereby changing the dominant product of the self-assembly. Following this fundamental mechanistic analysis of spontaneous hydrogen-bonded fiber formation, future work will focus on developing appropriate applications, in which molecular inclusions [48, 49] and viscoelastic measurements [50] will be analyzed.

CHAPTER 3
FUNCTIONS OF PLANAR MACROMOLECULES WITH NETWORKED STRUCTURES

Two-dimensional polymeric networks are ideal candidates for porous materials. As a family of polymeric networks, covalent organic framework (COF) membranes are promising for separating ions, dye molecules, and other water pollutants. However, COF films have a polycrystalline nature, with domain sizes ranging from nanometers to microns. Molecules can penetrate the film through predefined pores and grain boundaries. Though COF films are not single-crystalline membranes, they were expected to have oriented structures, i.e., the normal directions of COF domains align with the normal direction of the film. This expectation might not be true in thick COF membranes, where COF domains can stick together in a random fashion. Therefore, polycrystalline COF films have complex morphology, and it is difficult to exclude the transport of molecules through channels other than the predefined pores.

The polycrystalline nature of COF films raises questions about the mechanism of dye molecule separation experiments. Dye molecules are large organic molecules with aromatic groups and hydrophilic functional groups. Therefore, the interaction between dye molecules and hydrophobic COF macromolecules is complicated. Dye molecules range in size from one nanometer to tens of nanometers. For COF structures with predefined pore sizes of a few nanometers, it is reasonable to separate dye molecules of different sizes by a size-sieving mechanism. However, this size-sieving mechanism is built on the hypothesis that dye molecules travel through the predefined pores of COF structures. Even if COF films have well-defined oriented structures, they will not be ideal for water purification if the dye molecules have high affinity for the COF films, since the dye molecules

will bind strongly to the films and reduce their capability for water filtration. Therefore, it is important to elucidate the binding affinity of different dye molecules to COF macromolecules. In the following report, we use experimental adsorption measurements combined with computational results to determine the affinity of different dye molecules to COF macromolecules. Interestingly, large dye molecules have higher affinity for COF macromolecules. This result supports the alternative mechanism that COF films serve as adsorbents in water filtration experiments, where large dye molecules are measured to have a higher ”rejection” rate because they have higher affinity for the COF structures. The report was published in [51] and was changed structurally for the purpose of integration into the thesis.

Polycrystalline Covalent Organic Framework Films Act as Adsorbents, Not Membranes

Authors: Julie L. Fenton[#], David W. Burke[#], Dingwen Qian, M. Olvera de la Cruz, William R. Dichtel

Author contribution: W.R.D and M.O.d.l.C designed the research. J.L.F and D.W.B conducted experiments. D.Q. performed molecular dynamics simulations. J.L.F., D.W.B and D.Q analyzed results. J.L.F, D.W.B, D.Q, M.O.d.l.C and W.R.D wrote the paper.

This paper was published in [51]

3.1 Chapter abstract

Covalent organic framework (COF) membranes are of great promise for energy-efficient separations. Thick, polycrystalline COF films have been reported to separate dyes, salts, bacteria, and nanoparticles on the basis of size-selective transport through ordered pores. Here, we show that these materials function as adsorbents, not as size-sieving membranes. Binding isotherms of several dyes typical of the COF membrane literature to three COF powder samples illustrate that COFs are high-capacity adsorbents with affinities that span a range of 3 orders of magnitude, trends which map onto previously reported separation behavior. Computational results suggest that observed differences in adsorption can be correlated to variable entropic gains driving the adsorption process. The interaction between dye molecules and COF molecules can be understood using Asakura-Oosawa theory for depletion interactions. This model explains why large dye molecules tend to have higher affinity to the COF molecules. The theoretical results explain why large dye molecules have higher ”rejection” rate in the water filtration experiments using COF films, leading to misconception that COF films serve as size-sieving membranes.

3.2 Introduction

Covalent organic frameworks (COFs) are permanently porous, crystalline polymers with predictable structures obtained by reacting geometrically-constrained nodes and linkers to form networks of well-defined pores [52–55]. Changing the monomer structure enables tuning of the pore size, topology, dimensionality, and linkage chemistry [53, 55], offering a rational means to impart emergent properties of interest for energy storage [56–58], catalysis [59, 60], electronics [61–63], sensing [62, 64], gas storage[65], and molecular separations [66–70]. Of the many proposed applications for COFs, rationally designed membranes with uniform porosity are among the most promising [67, 70]. So far, tested COF separation membranes vary in materials quality, and can be divided into two categories. The first are thin films ($<$ 500 nm) with little or no apparent crystallinity, which are obtained by polymerizing monomers at liquid-liquid, liquid-solid, or liquid-air interfaces [69, 71–78]. These films exhibit low water permeability (typically $<$50 L m^{-1} bar^{-1} h^{-1}) and have shown separations of dyes [69, 71, 72, 74–78] and salt solutions [69, 71–73, 75]. The second category of COF membranes are obtained as thick films or solids using typical solvothermal or interfacial polymerization methods, and are effectively polycrystalline powders fused into arbitrary shapes [68, 79–84]. These forms often exhibit higher water permeability ($>$50 L m^{-1} bar^{-1} h^{-1}), and have been used to separate organic dyes [68, 80–82, 84], proteins [81], bacteria [80], salts [83], and nanoparticles [79]. The separation capabilities of both categories of COF membranes have been attributed to a size-based sieving mechanism through the micropores or mesopores defined by the COF lattice [68, 69, 71–84].

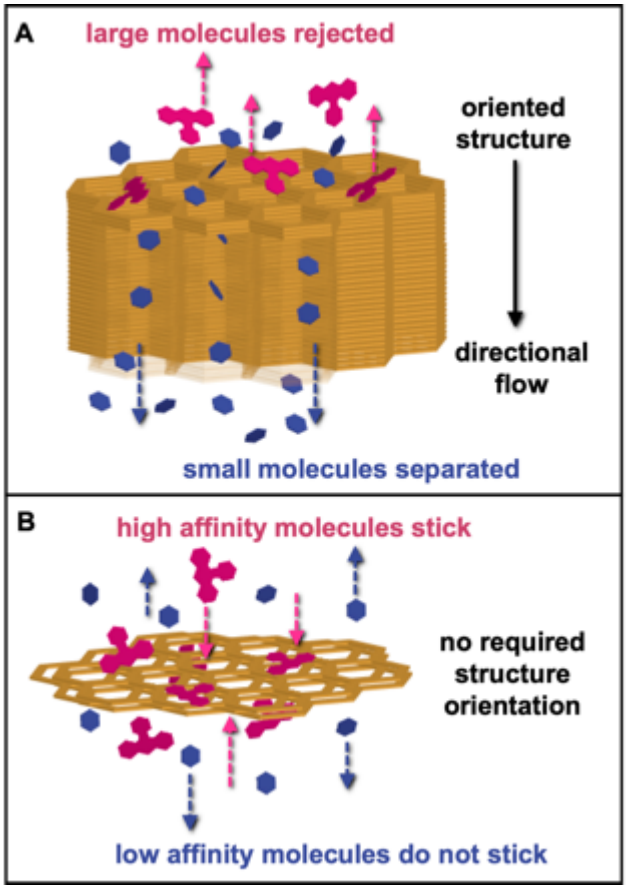

Figure 3.1: Cartoon depictions of (A) an idealized COF membrane sieving molecules based on its pore size and (B) adsorption-based separation of molecules based on their adsorption affinities for a non-oriented COF crystallite.

3.3 Experimental observations

3.3.1 Powder adsorption experiments

Organic dyes reported to be rejected by COF-based nanofiltration membranes adsorb onto polycrystalline COF powders with high affinities, whereas dyes reported to pass through COF membranes do not adsorb strongly. For example, an unfunctionalized, imine-linked COF powder (TAPB-PDA, Figure 3.2) was introduced into separate aqueous solutions of six organic dyes and mixed using an orbital shaker for 72 hours. The dyes were selected because they were used in prior reports of COF membrane separations and span broad ranges of size, charge, and chemical structure [68, 76, 77, 80–82, 84]. The set of dyes included larger molecules that did not pass through the COF membranes (Rhodamine B [RB], Brilliant Blue G [BB]) and smaller molecules that were passed by the membranes (4-nitrophenol [NP], 4-nitroaniline [NA]). Despite being of similar size to the rejected dyes, Methylene Blue (MB) and Congo Red (CR) have demonstrated variable transport through different COF films and were also selected. Visual inspection of the dye solutions after 72 h in contact with the COF powder indicated that the dyes adsorb to varying degrees: RB and BB adsorb strongly to the COF powder, leaving nearly colorless aqueous solutions above the solid COF. In contrast, almost no color change was observed for NP and NA-containing solutions under identical conditions. The MB and CR solutions exhibited moderate decolorization. These observations, which cannot be attributed to differences in molecular transport through a membrane, represent a first indication that the separations assigned to size exclusion by COF pores might instead be attributable, at least in part, to adsorption.

The range of qualitative association behaviors observed for organic dyes are quantifiable and general to multiple COF structures and linkage chemistries. The binding of each dye was assessed in triplicate against 3 polycrystalline COF powders: imine-linked TAPB-PDA and BND-TFB, and

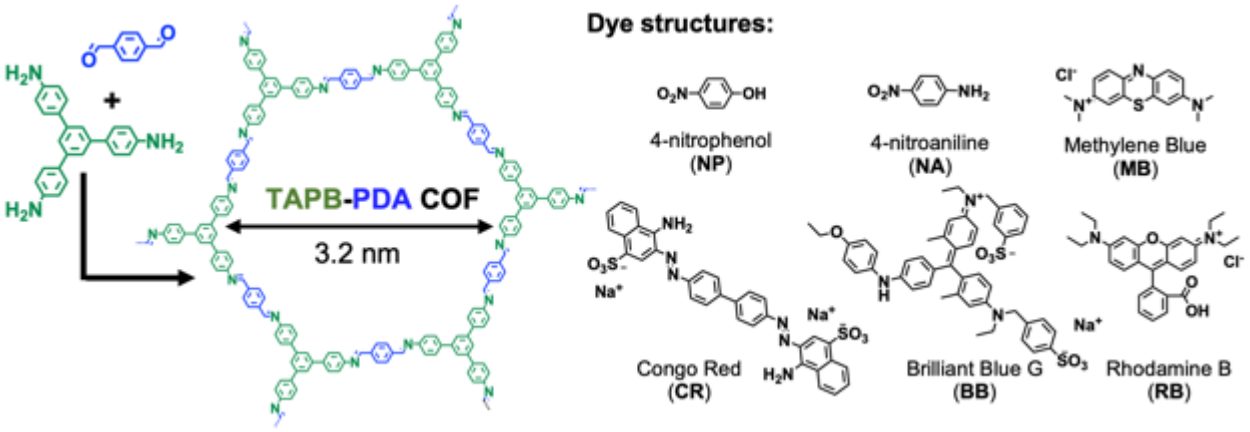

Figure 3.2: Molecular structures of (left) TAPB-PDA COF monomer and (right) six dye molecules used in the adsorption experiments.

β-ketoenamine-linked BND-TFP COF structures [85–87]. UV-Vis spectroscopy was used to quantify the residual dye in each solution post-incubation and calculate the amount adsorbed to the COF powder (Figure 3.3A). All COF-dye combinations resulted in at least partial dye removal, indicating that dye adsorption is general across all of the studied COFs, none of which were specifically designed as adsorbents. The three COFs do not show significantly differentiated adsorption behavior, as most dyes adsorb to all three COFs to similar degrees. The general trends observed in adsorption experiments are similar to those claimed to arise from membrane separations [68, 79, 83]: RB and BB strongly associate with the COF powders in a static experiment, resulting in more than 80% removal from aqueous solution. Smaller dyes like NP and NA associate to a far lesser extent (¡20% removal). MB and CR show variable and more moderate association with COF powders (30-80% removal). These quantitative findings offer a second indication that differences in adsorption behavior could be a meaningful factor in molecular separations previously attributed to size-dependent transport. Association constants between the COF powders and dyes vary by several orders of magnitude depending on the dye structure and reflect the observed differences in

initial uptake experiments. Isotherms were constructed for the three COF powders with RB, CR, and NP, dyes that sample the range of associations observed in the single-point uptake experiment. COF powder (333 mg L^{-1} loading) was introduced to dye solutions at six concentrations and mixed using an orbital shaker for 72 hours to reach adsorption equilibrium. Residual dye concentration was determined by UV-Vis spectroscopy. The resulting isotherms were fit to a Langmuir model (Figure 3.3B-D) to determine values for maximum capacity (Qm, mg g^{-1}) and adsorption affinity (KL, M^{-1}) for each COF/dye pair (Table 3.1) [87–89]. For TAPB-PDA (Figure 3.3B), the maximum dye capacities are uniformly large (700, 520, and 580 mg g^{-1} for RB, CR, and NP, respectively), consistent with a high surface area adsorbent. However, the adsorption affinities of the three dyes span a 100-fold range, with RB most strongly adsorbed (KL = 104 M^{-1}), followed by CR (KL = 103 M^{-1}) and NP (KL = 102 M^{-1}). Similar trends in capacity and affinity were also found for BND-TFB and BND-TFP COFs. To date, many "membrane" experiments have been conducted by passing low-concentration dye solutions through thick COF films [68, 80, 84]. At these low concentrations, dyes with high association constants will almost completely adsorb to the COF, while those with low association constants will largely remain in solution, assuming that the COF is not near saturation. Given that polycrystalline COFs have uniformly high uptake capacities, and rejection performance is often characterized using small (<15 mL) volumes of dye solution [68, 80, 84], it is reasonable to expect that adsorption could play a dominant role in controlling the observed separation performance of these systems.

3.3.2 Flow experiments through a polycrystalline COF pellet

Mixtures of organic dyes claimed to be separated by COF membranes via selective transport are separated when passed through a polycrystalline COF pellet. However, these dye separations are better explained by differences in their adsorption affinity to COF powders. Typical studies de-

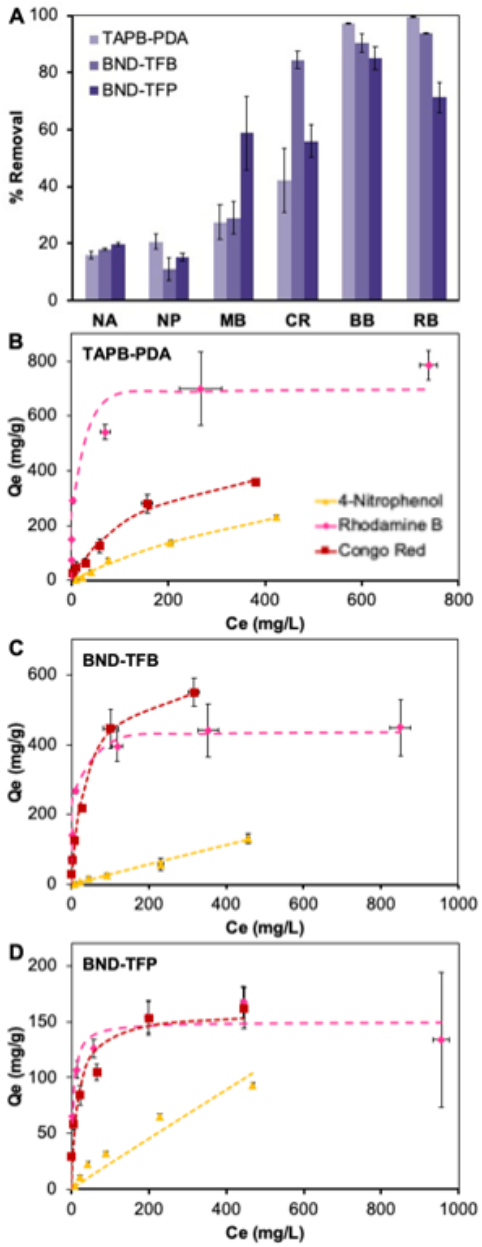

Figure 3.3: (A) Removal of various organic dyes (50 mg L-1) from Milli-Q water by TAPB-PDA, BND-TFB, and BND-TFP COFs (333 mg L-1). (B-D) Adsorption isotherms and associated Langmuir fits for Rhodamine B, Congo Red, and 4-nitrophenol binding to (B) TAPB-PDA, (C) BND-TFB, and (D) BND-TFP COFs. Residual dye concentration determined by UV-Vis spectroscopy. Error bars represent standard deviation of triplicate measurements.

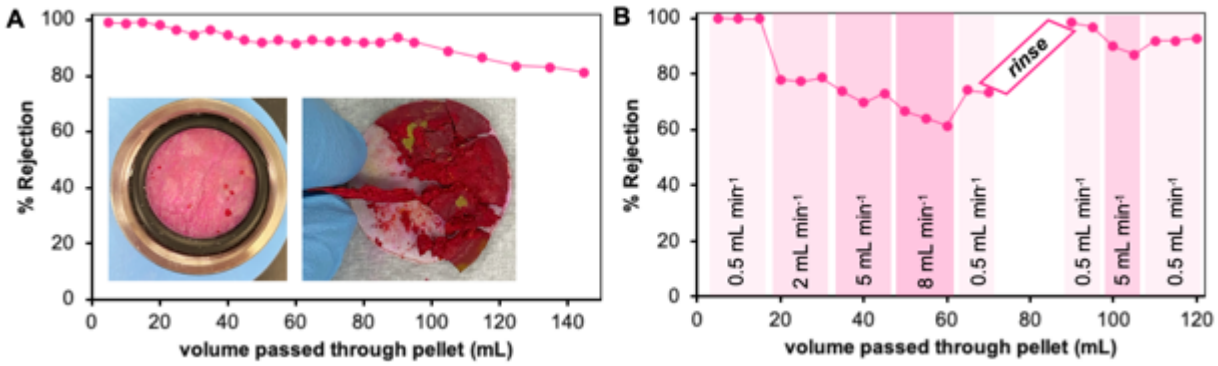

Figure 3.4: (A) Rejection of RB as a function of total passed volume with a constant 0.5 mL min^{-1} flow rate, obtained for a TAPB-PDA COF pellet and a 50 mg L^{-1} dye solution. Consistent with literature precedent, RB is rejected initially, but performance gradually decreases, which is more consistent with an adsorption process. Inset: photographs of pellet after testing, showing RB saturation on the surface and within a cross-sectional area of the pellet. (B) Plot of rejection of RB as a function of total passed volume with variable flow rate, highlighting the dependence of observed rejection on dye contact time. Increased flow rates dramatically decrease rejection performance, which can be partially recovered by decreasing flow rate and fully recovered with a methanol wash. This behavior is consistent with typical adsorbents and inconsistent with a nanofiltration mechanism.

	Rhodamine B		**Congo Red**		**4-Nitrophenol**	
	Q_m (mg/g)	K_L (M^{-1})	Q_m (mg/g)	K_L (M^{-1})	Q_m (mg/g)	K_L (M^{-1})
TAPB-PDA	700	9.4 x 10^4	520	4.4 x 10^3	580	2.2 x 10^2
BND-TFB	440	7.0 x 10^4	620	1.7 x 10^4	2500	1.7 x 10^1
BND-TFP	150	9.5 x 10^4	160	4.0 x 10^4	2500	1.3 x 10^1

Table 3.1: Association constants and maximum capacities for COF powders with different dyes.

signed to evaluate size-sieving effectively separate a two-dye mixture consisting of a larger dye (such as RB) and a smaller one (such as NP), although the pores of COFs evaluated in these experiments should be sufficiently large to accommodate both dyes. Our experimental isotherms demonstrate that these dyes also span a two order of magnitude range of adsorption affinities, indicating that adsorption could be responsible for this separation process. To this typical mixture, we added MB, which is similar in size to RB but exhibits substantially lower adsorption affinity, similar to NP. A mixed RB/NP/MB solution (100 mg L^{-1} total dye concentration, 33.3 mg L^{-1} for each individual dye) was passed through a TAPB-PDA COF pellet at a constant rate of 0.5 mL min^{-1}. 5 mL aliquots of the filtrate were collected, diluted, and measured by UV-Vis spectroscopy until a total of 40 mL had passed through the pellet (Figures 3.4A). Absorbance signals corresponding to each dye were compared to the absorbance of appropriate controls to determine the percent breakthrough of each dye as a function of passed volume (Figure 3.4B). Consistent with single-dye flow results, the majority of the strongly adsorbing RB is removed by the COF layer, resulting in a low and consistent solution concentration of RB throughout the 40 mL experiment, corresponding to 10-17$\%$ breakthrough. Conversely, weakly associating dyes, NP and MB, break through the pellet to greater extent, corresponding to 31$\%$ breakthrough in the first 5 mL aliquot, which increased to 70$\%$ and 68$\%$ in later aliquots. A subsequent methanol wash removes the adsorbed dyes from the pellet. These experiments provide compelling evidence that the dye separation capabilities

observed in previous studies of polycrystalline COF membranes can be explained by differences in adsorption affinities of the dyes to the COF and do not require selective transport through the pores. The above results cast serious doubt on whether any separation of dye molecules by a thick, polycrystalline COF membrane occurs through differences in molecular transport through the pores rather than adsorption. Recently, nanoparticles were separated by a similar COF membrane with remarkable size cutoffs that exactly matched the diameter of the inorganic component of the particle [79]. These results would seemingly be a powerful confirmation of the ability to tailor the size of a COF pore to achieve deterministic separation of nanometer-scale objects. This capability would be especially useful since nanoscale structures are better matched to the size of typical 2D COF pores than small molecules. We believe that these experiments were designed to produce the desired size selectivity by manipulation of the nanoparticle surface chemistry. The reported conclusions are further eroded by a lack conclusive corroborating evidence that inexplicably passed through peer review. Solution-dispersible colloidal inorganic nanoparticles contain an inorganic core surrounded by a shell of stabilizing ligands, which prevent agglomeration, promote solvent dispersibility, and add to the total size of the composite particle beyond that of the inorganic core. A reported size cut-off that exactly matches the size of the nanoparticle with the calculated COF pore size ignores the contribution of the molecular ligand shell, a physically impossible result if transport is dominated by size-selective pore exclusion. More importantly, larger nanoparticles reported to be rejected by the COF membrane had standard citrate ligands, whereas smaller nanoparticles reported to pass through the membrane had cationic thiol ligands. Therefore, the particle separation corresponded to this altered ligand identity, not just the particle size. The thiol ligands used on the particles that were able to pass through the COF are exotic and seem likely to have been chosen because they confer the desired separation behavior. We do not make the this claim lightly, but it is otherwise hard to rationalize why the ligand sets were switched between

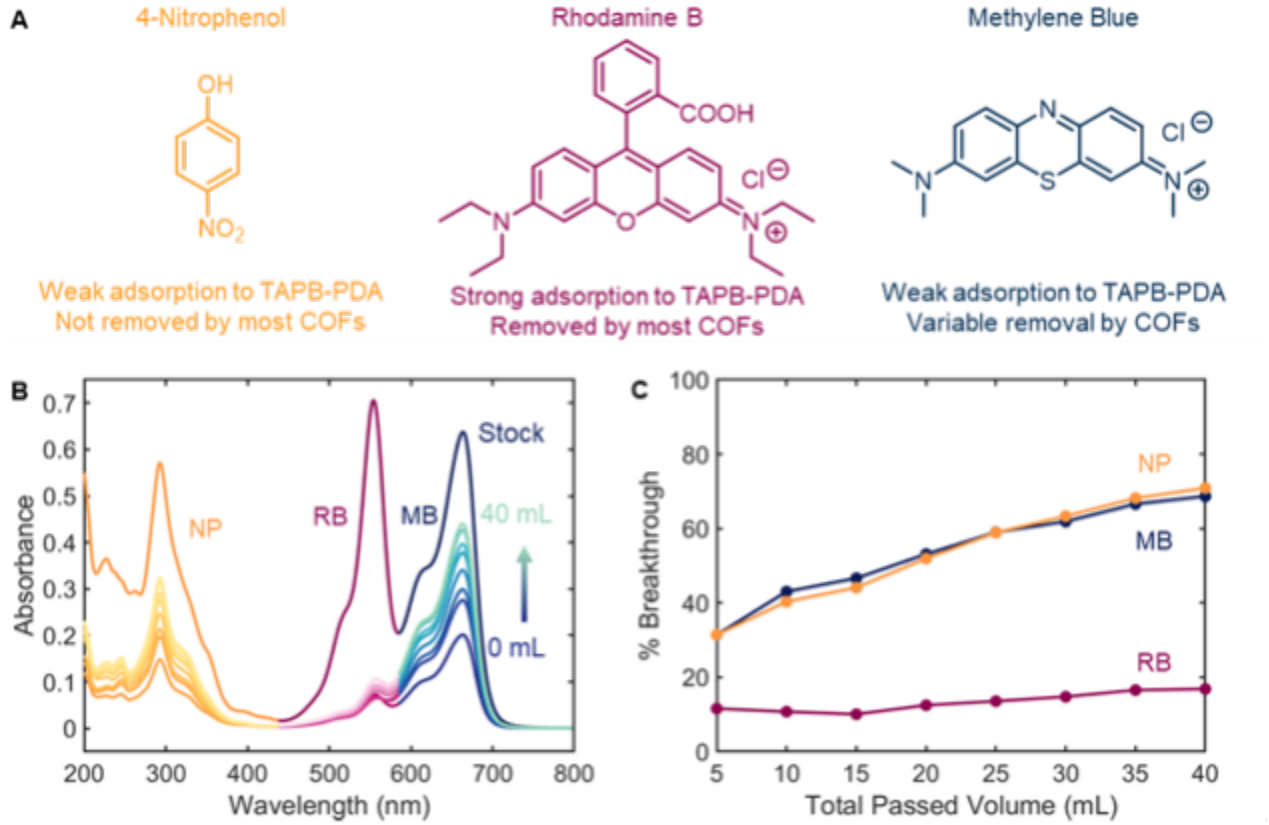

Figure 3.5: (A) Chemical structures of NP, RB, and MB, a mixture of which was passed through a TAPB-PDA COF pellet to study their separation in flow. (B) UV-Vis spectra of the mixed dye stock solution and all aqueous eluted fractions, color coded by dye (yellow for NP, pink for RB, and blue for MB). (C) Percent breakthrough for each dye plotted as a function of total passed volume of mixed dye stock solution. These data indicate that the weakly-adsorbing dyes (NP and MB) break through the COF pellet rapidly, while strongly adsorbing RB is largely captured by the pellet, leading to the separation of dye molecules based on affinity for the COF.

standard and exotic ligands for populations of nanoparticles on either side of the calculated COF pore size.

3.4 Molecular simulations and theoretical modeling

3.4.1 Description of the simulational systems

Classical all-atom MD simulations were performed using the OPLS AA/M force field [90]. The simulations were performed using the package GROMACS [91]. The force field parameters of dye molecules are achieved through LigParGen Server [92]. The simulations of BND-TFB COF membranes combined with 4-Nitrophenol and Rhodamine B molecules are conducted with the same simulation box size. Ten layers of COF membranes and one dye molecule are contained in both simulation boxes. It is observed that both dye molecules are absorbed to COF membranes at equilibrium. Since the system is translational invariant in x-y plane, the free energy profiles of absorption (also referred to as potential of mean forces (PMFS)) were derived from molecular dynamics simulations using umbrella sampling method along z axis.

3.4.2 Determining experimental free energies of adsorption from K_L values

The difference of absorption free energy achieved from experiments was determined using adsorption affinity (K_L) values determined from experimental dye adsorption isotherms in accordance with the following equation:

$$\Delta G_{4-Nitrophenol} - \Delta G_{RhodamineB} = -kTln\frac{K_{4-Nitrophenol}}{K_{RhodamineB}} \tag{3.1}$$

We find that the experimental absorption free energy of 4-Nitrophenol is 21.1 kJ/mol smaller than that of Rhodamine B.

3.4.3 Calculation of enthalpic and entropic components of absorption free energy

Differences in computed values of adsorption free energies of RB and NP are in qualitative agreement with findings from the experimental isotherms, bolstering our understanding of the observed discrepancies in adsorption behaviors of the two dyes. Molecular dynamics simulations of NP and RB molecules interacting with several layers of BND-TFB COF were conducted. A dye molecule is pulled from the COF surface to generate a distance-dependent free-energy profile for the desorption process (Fig. S4). For a more tightly adsorbed molecule, the energy difference between the bound and unbound state will be higher than a more loosely associated species. The computed free energy differences of the minimum(absorption/bound state) and the flat platform(free/unbound state) are -25.3 kJ mol^{-1} for NP and -33.8 kJ mol^{-1} for RB, a difference of 8.5 kJ mol^{-1}. The experimental adsorption free energy, calculated from the adsorption affinity (K_L) values in Table 1, is 21.1 kJ mol^{-1} larger for RB than for NP. Though the absolute values differ, likely because the simulation uses simplified, low-concentration conditions for adsorption, the free energy difference value derived from simulations is in qualitative agreement with experimental findings. In both theory and experiment, RB associates more strongly with the COF surface than NP.

The computation of the enthalpy differences of the absorption states and the free states cannot be directly derived from the enthalpy values of the two states since the system is much larger than the dye molecules and most of the simulation box interacts weakly with the dye molecules, which means those parts are not correlated to the absorption process. The thermal fluctuations of those molecules are large compared to the enthalpic change during the absorption process. To solve this problem, we only calculate the change of potential energies between dye molecules and other part of the systems and the potential energies between the COF membrane and water molecules. Physically these parts are the potential energies that matters during the absorption processes. These values are calculated to be: $\Delta H_{4-Nitrophenol} = -10.6\ kJ/mol$, $\Delta H_{RhodamineB} = 20.7\ kJ/mol$

Using the formula $\Delta G = \Delta H - T\Delta S$, we find the entropy changes during the absorption process: $T\Delta S_{4-Nitrophenol} = 14.7\ kJ/mol$, $T\Delta S_{RhodamineB} = 60.8\ kJ/mol$.

The adsorption process is driven by a large entropic gain during COF/dye association, and the difference in affinity can be correlated to the relative sizes of dye molecules. To determine the entropic contributions, we decomposed the absorption free energies (ΔG) into enthalpic components ΔH and entropic components $T\Delta S$. The calculated enthalpic components (ΔH) of the absorption free energies are negative for NP and positive for RB, indicating that adsorption is energetically unfavorable for RB and suggesting that its adsorption is driven by a large entropic gain. Indeed, the entropy change during RB adsorption is approximately four times that of NP. Further simulations suggest that this increase in entropy upon adsorption can be attributed to depletion interactions between the COF and dye molecules. As a molecule approaches the COF surface, the excluded volume for water molecules is reduced, resulting in an increase in system entropy. As the dye molecule increases in size, more water is displaced because the excluded volume is larger, and the entropic gain increases in magnitude. This means that larger molecules should have a significant advantage in adsorption affinity to COF structures before any specific chemical structure or energetic terms are considered. This simple result may explain why larger dyes are often observed to be size excluded from polycrystalline COF membranes and smaller ones are not, even if size-selective transport through a COF pore is not the mechanism driving the observed separations.

3.5 Conclusions, Implications, and Outlook

In the area of framework materials, it is tempting and perhaps too common to map seemingly reasonable mechanistic hypotheses onto cartoons that do not depict reality. Polycrystalline COF membranes used in separation studies to date are ultimately not the idealized 2D COF structures derived from powder diffraction methods, and it is hard to rationalize how an unaligned, polycrys-

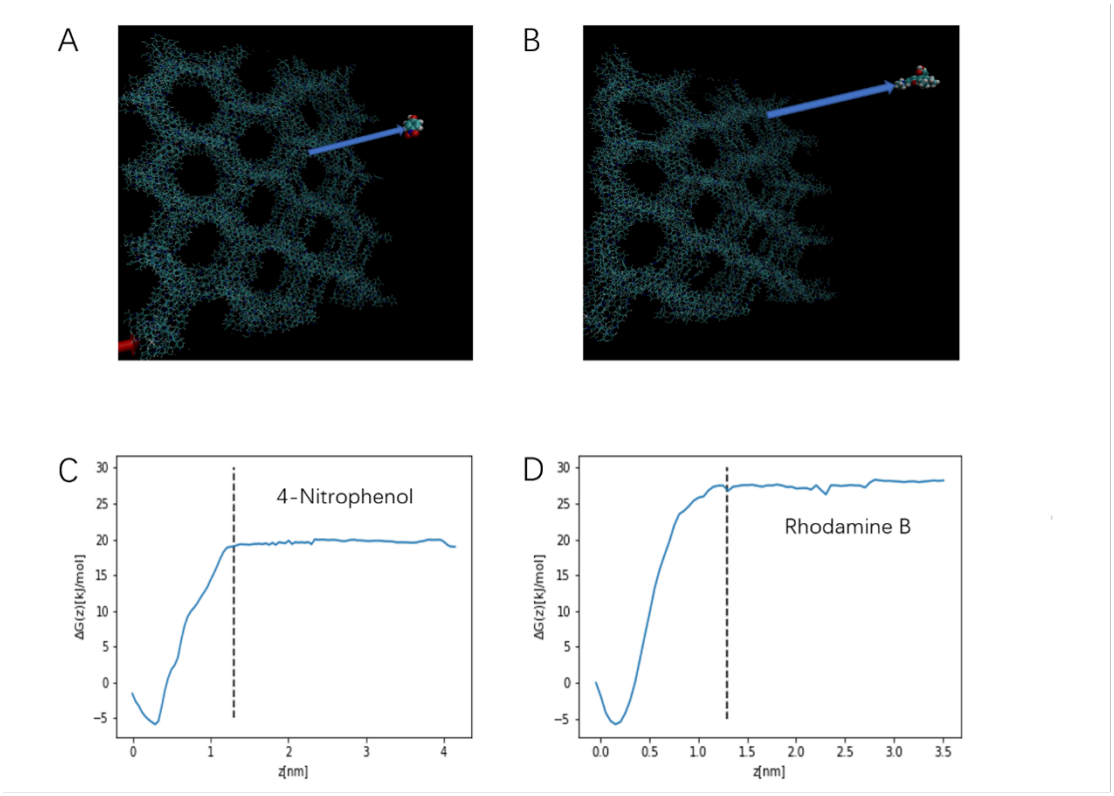

Figure 3.6: (A) Simulation snapshot of a 4-Nitrophenol molecule being pulled from the BND-TFB COF membrane (B) Simulation snapshot of a Rhodamine B molecule being pulled from the COF membrane. In both figures, water molecules are invisible. (C) and (D) correspond to free-energy profile of 4-nitrophenol(C) and Rhodamine B(D) for moving from the absorption state into the bulk water. All free-energy profiles are defined to zero at the pulling start point. The z value of the start point are set to zero. The dashed lines represent the boundaries of the absorption regime and the bulk water. The absorption free energy is calculated from the difference of the minimum of the free energy file and the average of the free energy in the bulk water.

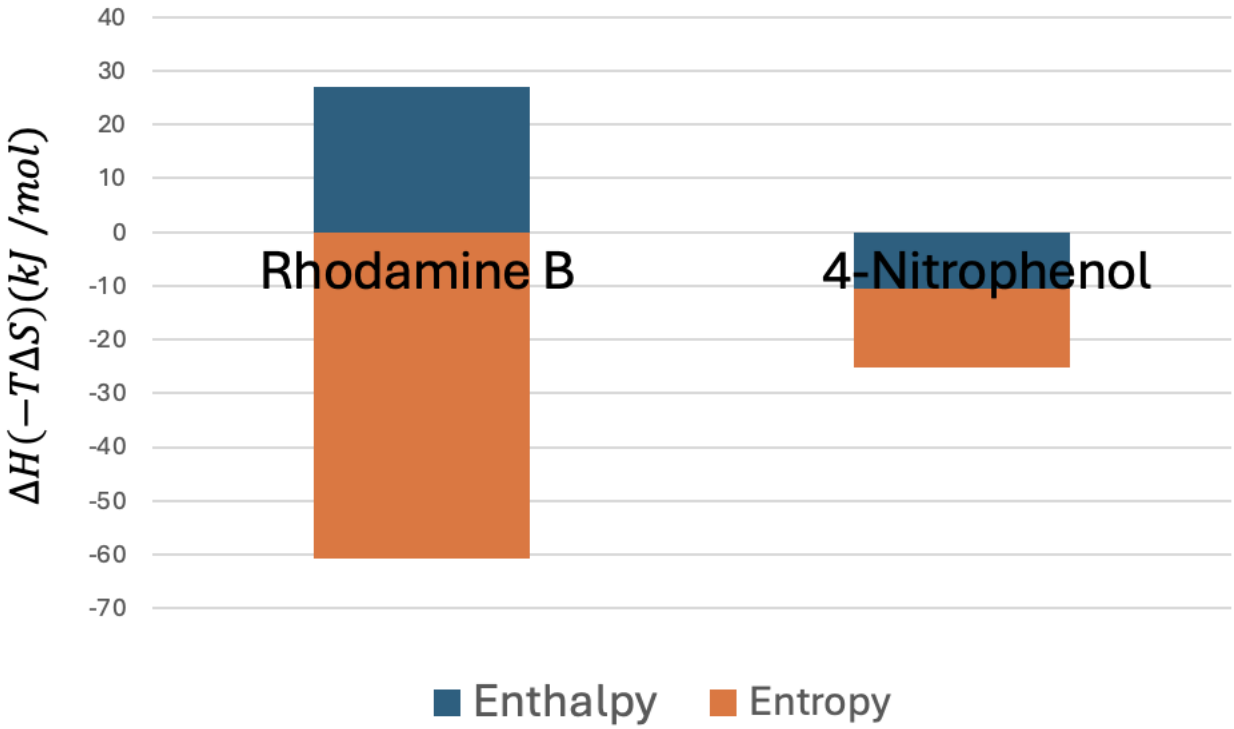

Figure 3.7: Simulational results of entropy and enthalpy portions of the free energy of adsorption. It can be seen that even Rhodamine B is enthalpically unfavored for adsorption, the entropic term dominates the free energy and favors the adsorption of Rhodamine B, which is a larger dye molecule.

talline, and defective structure can show both very high apparent size selectivity and permeability. The present study indeed demonstrates that dye separations through polycrystalline COF membranes, often attributed to size-selective rejection, more likely occur via mechanisms that do not require pristine membranes nor specialized fabrication techniques. COF samples show adsorption isotherms of various chromophores commonly used to demonstrate separations that strongly implicate adsorption as the primary separation mechanism for so-called COF membranes. Adsorption is not an inherently undesirable separation mechanism, but novel adsorbents are designed and deployed in completely different forms and contexts than separation membranes. We would expect these differences to become clear in future efforts to engineer separation processes using polycrystalline COF films or other efforts to build on the existing COF membrane literature. Based on these findings, it is necessary to reevaluate the field of COF-based separations. The assumption that polycrystalline COF films function as precise molecular sieves has propagated through the literature because of a pervasive lack of adequate membrane performance characterization, as well as the widely variable materials quality of tested COF membranes. Our flow rate- and volume-dependent dye rejection studies demonstrate that experiments run at insufficient flow rates and volumes can support inaccurate conclusions about the separation mechanism. Although these parameters might be first identified by optimizing new COF systems, studies that do not also probe other conditions risk failing to recognize the actual transport/rejection mechanism and might instead serve to confirm preconceived hypotheses. Using objects that are more appropriately sized to the typical COF pore than previous small molecule models, reported nanoparticle sieving experiments appear to be a powerful demonstration of size-selective transport through a molecularly precise membrane. Though solely attributed to differences in particle size and exactly correlated to the dimension of the tested COF pore, the reported nanoparticle separations also corresponded to a change in surface ligand chemistry. An unnecessary change with this level of precision did

not occur by coincidence. Extraordinary claims of size-selection require exceptional evidence to corroborate them, and reviewers should demand very high standards for studies that insinuate this behavior. Surface chemistry must be consistent in any demonstration of size-selectivity. Size-selectivity must be quantified and reported based on self-consistent bulk measurement techniques that confirm observations made by microscopy. The performance yield must be characterized and reported over long elution volumes, as size distributions determined by microscopy at early elution points are insufficient evidence for demonstrating size-selection. Though nanoscale size-separations remain a potentially promising application for COFs, meaningful conclusions require careful consideration of less-prominent factors in the chosen system, consistency, and appropriate control experiments. To realize the potential of molecularly precise membranes for any proposed separation, improved materials quality is critically important. Ascribing a precise, molecular separation mechanism based on pore transport to materials that obviously do not exhibit the ideal structure and orientation will impede real progress in this field. However, the idealized cartoon structure for a 2D COF membrane (crystalline, oriented, long-range order) has yet to be attained, and it is reasonable to expect that the dominant mechanisms of molecular transport, and therefore rejection, by COF films will change as crystallite size and orientation are increased. For instance, a COF film composed of crystallites that are highly oriented in a pore-on geometry will contain continuous channels that may facilitate more through-pore molecular transport than a non-oriented counterpart. Furthermore, as the lateral dimensions of crystallites are increased, the density of grain boundary defects will decrease, and the relative contributions of through-pore and through-defect transport will change. These structural improvements may manifest themselves in new mechanisms of small molecule rejection, which could include a mixture of pore-mediated size exclusion and adsorption to the COF surface. It is critical that researchers approach the characterization of these improved materials and their transport properties with care, as the underlying

mechanisms will be complex. Such studies will require carefully designed control experiments that unambiguously demonstrate that rejection is attributed to the COF alone, rather than any supporting membrane, as well as systematic studies of separation performance with varied conditions to rule out alternative transport mechanisms. Despite these challenges, focused efforts to enhance membrane quality and improve materials characterization thereof are foundational to advancing the field towards designer membranes, which have the potential to revolutionize the field of separation science.

CHAPTER 4
TRANSPORT IN A NETWORK STRUCTURE

When particles are driven in opposite directions, they spontaneously segregate into flowing lanes. The formation of lanes reduces the friction between oppositely moving particles and increases the efficiency of motion. The lane formation phenomenon is ubiquitous in charged colloidal mixtures [93], pedestrian dynamics [94], and active Brownian particles [95].

When the size asymmetry of particles increases, the large particles tend to form periodic structures while small particles diffuse freely through the lattice. This phenomenon is known as superionic behavior in ionic conductors [96] and colloidal mixtures [97–99]. When superionic colloidal mixtures are driven by an external field, it is expected that the large and small particles respond differently. The lane formation phase is observed at a low field, which is similar to the size-symmetric systems. The coupling between the flow of small particles and the vibrational motion of the large particles leads to a novel nonequilibrium phase. Small particles aggregate into clusters with the occurrence of stable wavepackets of vibrational motion of large particles. This behavior is reminiscent of soliton excitation in nonlinear dynamics. The following report is published in [100].

Field-driven cluster formation in two-dimensional colloidal binary mixtures

Authors: Dingwen Qian, M. Olvera de la Cruz

This paper was published in [100]

4.1 Chapter abstract

We study size- and charge-asymmetric oppositely charged colloids driven by an external electric field. The large particles are connected by harmonic springs, forming a hexagonal-lattice network while the small particles are free of bonds and exhibit fluid-like motion. We show that this model exhibits a cluster formation pattern when the external driving force exceeds a critical value. The clustering is accompanied with stable wavepackets in vibrational motions of the large particles.

4.2 Introduction

In solids, the atoms vibrate around their equilibrium positions and the excitations of vibrational motions, phonons, are well described by elastic theory [101]. Although particles in fluids have vibrational motions, they do not have well-defined equilibrium positions. Instead of tracking the motion of individual fluid particles, it is more appropriate to describe them with continuous quantities, such as density, velocity, and pressure. Active systems can be solid or fluid. While active solids have well-defined reference positions, active fluids do not. Most well-studied active systems are fluids [102–104], however, interest in active solids has grown recently [105, 106].

In many physical systems, people have observed the coexistence of vibrational and fluid-like degrees of freedom. Examples include ion cores and conducting electrons in metals, rigid and mobile ions in superionic conductors [96] and most recently, superionic behavior observed in size-asymmetric colloidal compounds [49, 97–99, 107–110]. While there are many reports on the

equilibrium behavior of these mixtures, the far-from-equilibrium behavior is still not studied. In this paper, we explore the far-from-equilibrium behavior of systems with both *vibrational* and *fluid-like* degrees of freedom.

Here, we study size- and charge-asymmetric oppositely charged colloidal compounds under an external electric field in a two-dimensional space. The study of two-dimensional colloidal mixtures is highly relevant to the behavior of materials confined at interfaces in both equilibrium [111–114] and nonequilibrium [115, 116] conditions. When colloidal particles sediment onto the base of a glass sample cell, they form a monolayer of colloidal mixtures and their motions are in the two directions parallel to the glass base [111]. Recent advancement in the synthesis of colloidal disks [117] inspires us to study size-asymmetric colloidal disks in a two-dimensional space. A particular feature of our model systems is harmonic interactions between the large particles. The large colloidal particles are connected by harmonic springs and form a hexagonal lattice. The harmonic springs enforce elastic coupling between the motion of the large particles in the far-from-equilibrium regime, and elasticity plays an important role in the phenomena we describe in this paper. Experimentally, the development of programmable DNA origami nanosprings makes it possible to create springs with adjustable lengths and strengths [118]. Two-dimensional networks of polymer-linked nanoparticles have been synthesized [119], which is similar to the network of large colloidal particles we propose in this paper. Another important feature of our systems is an extremely large size ratio. The size of the small particles is set to be much smaller than the large particles so that the small particles drift across the lattice under the external field, showing the behavior of a continuous flow. Under external driving force, the small particles flow through the lattice formed by the large particles, resembling the flow of fluid through the interstitial spaces in a foam [120, 121]. In this study, in analogy to the solitons found in the flow of fluid through foams, we observe cluster formation of small particles and soliton-like vibrational motions of the

large particles when the external driving force exceeds a critical value. The soliton-like vibrational motions mean that wavepackets of displacement vectors of the large particles travel with stable shapes.

4.3 Model and methodology

Here we briefly summarize the system design and geometry. The motions of the size-asymmetric colloidal disks are confined to the two directions parallel to the substrate. The size ratio between the large and small colloidal particles is $R : r = 20 : 1$ and the number ratio between the large and small particles is $N : n = 1 : 12$. The radius of the small particles is $r = 50\ \mathrm{nm}$, which is the unit length scale in our system. The large colloidal particles are connected by harmonic springs, forming a hexagonal lattice with lattice constant $a = 45r$. FIG. 4.1 shows the geometry of one unit cell of the system from the top view and the side view. The total area fraction of the colloidal particles is $\phi = 0.738$. The simulations are conducted in a square box containing 60×60 unit cells with periodic boundary conditions. The particle number, volume, and temperature are constant.

We introduce here the interactions and external driven forces in our Brownian dynamics simulations. Since the system is in a low Reynolds number regime, overdamped Langevin dynamics is implemented to simulate the equilibrium and nonequilibrium behavior of our system, which neglects the inertia of particles. We use the LAMMPS package to conduct the Brownian dynamics simulations [122]. We do not consider hydrodynamics effects here. The equation of motion for particle i is:

$$\frac{\mathrm{d}\mathbf{r}_i}{\mathrm{d}t} = \frac{-\boldsymbol{\nabla}_i U + \mathbf{F}_{ex}^i}{\gamma_i} + \boldsymbol{\xi}_i \tag{4.1}$$

where $\mathbf{r}_i$ is the position vector of the particle i, U is the total conservative force potential energy, $\mathbf{F}_{ex}^i = \mathbf{E}q_i$ is the external force acting on the particle i, and γ_i is the drag coefficient of particle i.

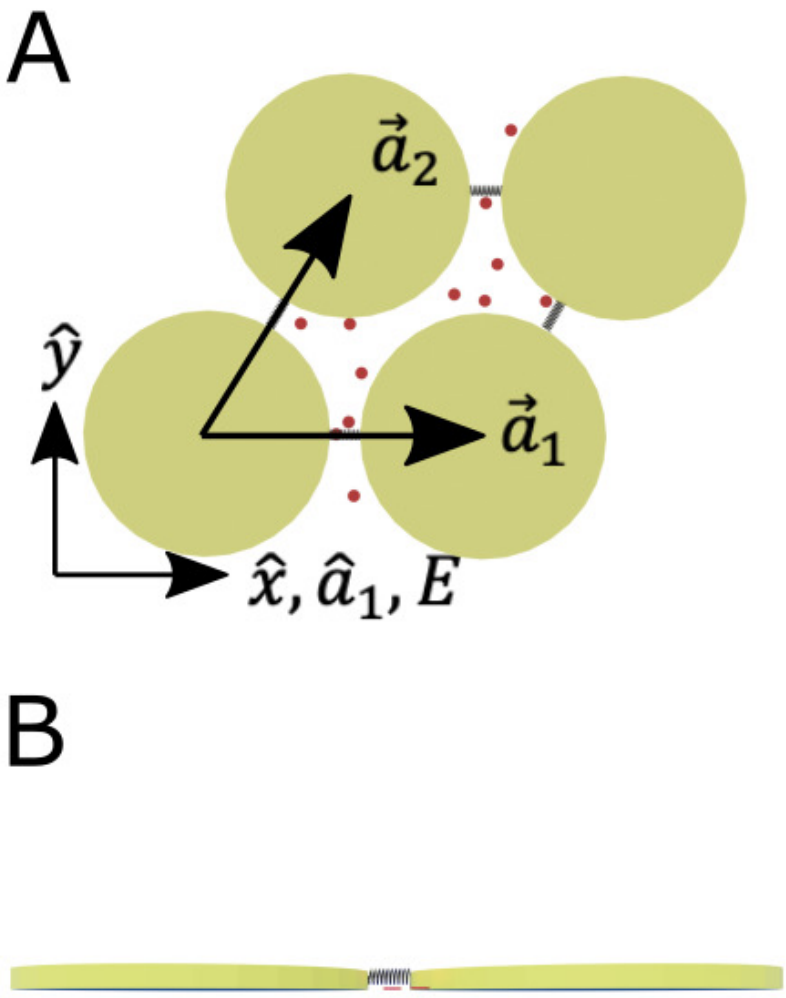

Figure 4.1: Sketches of the system geometry. (A) Top view of one unit cell of the hexagonal lattice. The lattice vectors are $\vec{a}_1 = [45r, 0]$ and $\vec{a}_2 = [\frac{45r}{2}, \frac{45\sqrt{3}r}{2}]$. The electric field is applied in the direction of $\vec{a}_1$, which is the x-direction of the simulation box. (B) Side view of the 3D structures of the large colloidal particles, small colloidal particles, and nanosprings connecting the large particles. The height of the small particles is much lower than the height of the large particles, $h \ll H$, and the monomers of the nanosprings are typically at the length scale of $1\ \mathrm{nm}$. Therefore, the nanosprings are not an obstacle for the small particles.

The charge of the large particles is $q_L = 96\ e$ and the charge of the small particles is $q_S = -8\ e$. The charge ratio between the large and small particles is $q_L : q_S = 12 : -1$, which respects the charge neutrality considering the number ratio is $N : n = 1 : 12$. The drag force on particle i depends on the drag coefficient and velocity of the particle $\mathbf{F}_{Di} = -\gamma_i \mathbf{v}_i$. Here we explain how we set the drag coefficients of the colloidal disks. We set the height of the colloidal disks to be much smaller than their radius, i.e., $h = 5\ \mathrm{nm} \ll r$ and $H = 50\ \mathrm{nm} \ll R$. In a low Reynolds number fluid with viscosity η, the drag force on a disk with radius r, negligible height $h \ll r$ and moving in the plane with speed $\boldsymbol{v}$ has an exact formula $\boldsymbol{F}_D = -\frac{32}{3}\eta r \boldsymbol{v}$, which is independent of the thickness of the disks [28]. Therefore, the friction coefficients of the small particles and large particles are $\gamma_S = \frac{32}{3}\eta r$ and $\gamma_L = \frac{32}{3}\eta R$ respectively, where the water viscosity is $\eta = 1 \times 10^{-3}\ \mathrm{Pa \cdot s}$. It follows that the friction coefficient for the large particles is 20 times the friction coefficient for the small particles, $\gamma_L = 20\gamma_S$. The thermal force $\boldsymbol{\xi}_i$ is a white noise with zero mean, satisfying $\langle \xi_{i\alpha} \xi_{j\beta} \rangle = 2\frac{k_B T}{\gamma_i}\delta_{ij}\delta_{\alpha\beta}\delta(t - t')$, where i, j denote the particle indices and α, β denote the spatial directions. $k_B T$ is the thermal energy at $T = 298\ \mathrm{K}$ and set as the unit energy scale in the simulation. The Brownian time of the small particles $\tau = \frac{r^2}{D} = 3.3 \times 10^{-4}\ \mathrm{s}$ is set as the time unit, where $D = \frac{k_B T}{\gamma_S}$ is the bare diffusion coefficient of the small particle. The timestep for integration is $\Delta t = 10^{-4}\tau$.

The potential energy of total conservative interactions U consists of bonded and non-bonded interactions. The bonded interaction is the harmonic potential between neighboring large particles, $U_{spring} = \sum_{\{ij\}(nn)} \frac{1}{2}K(r_{ij} - a)^2$, where (nn) denotes nearest neighbors, K is the spring constant, r_{ij} is the distance between the neighboring large particles and a is the equilibrium length of the harmonic springs, which equals the lattice constant. In this report, we use a dimensionless spring constant to quantify the strength of the springs, $\tilde{K} = \frac{Kr^2}{k_B T}$, where r is the radius of the small particles and the unit length scale in our simulations. The non-bonded interactions are composed

of two parts, the hardcore interaction and the screened Coulomb interaction. We use the repulsive Weeks-Chandler-Andersen (WCA) potential to model the hardcore interaction, $U_{WCA}(r_{ij})$ given by

$$\begin{cases} 4\varepsilon\left[\left(\frac{\sigma_{ij}}{r_{ij}}\right)^{12}-\left(\frac{\sigma_{ij}}{r_{ij}}\right)^{6}\right]+\varepsilon, & r_{ij}<2^{1/6}\sigma_{ij}. \\ 0, & r_{ij}>2^{1/6}\sigma_{ij}. \end{cases} \tag{4.2}$$

and Yukawa potential to model the screened electrostatic interaction,

$$\beta U_{el}(r_{ij}) = \frac{\lambda_B q_i q_j \exp[-\kappa(r_{ij}-\sigma_{ij})]}{(1+\kappa R_i)(1+\kappa R_j) r_{ij}} \tag{4.3}$$

Here, $\sigma_{ij} = R_i + R_j$ where the R_i and R_j are the radii of particle i and j respectively. The WCA interaction strength $\varepsilon = 10\ k_BT$, $\beta = \frac{1}{k_BT}$, and $\lambda_B = \frac{e^2}{4\pi\epsilon_0\epsilon_r k_BT}$ is the Bjerrum length. The Bjerrum length equals 0.7 nm for water solvent at $T = 298$ K, and q_i and q_j are the charges of the particle i and j in the unit of the elementary charge respectively. The Debye length $\lambda_D = \kappa^{-1} = (4\pi\lambda_B \sum_{i=1}^{N} n_i z_i^2)^{-\frac{1}{2}}$ is a measure of how far a charge carrier's electrostatic effects persist in a solution with free ion concentration n_i and ion charge numbers z_i. The environment is deionized water with ion concentration $n = 10^{-7}$ mol/L. The Debye length equals $1\ \mu$m in the deionized water at $T = 298$ K, which is the radius of the large particles. This means the electrostatic interaction persists up to the radius of the large particles.

Before we conduct the simulations on the nonequilibrium conditions, we prepared the systems by allowing them to reach thermodynamics equilibrium. We set the external force equal to zero and run the simulations for $10^2\tau$. The pressure and internal energy of the systems become stable, and we see that as the criterion of equilibrium for the systems. Then, we apply an external force on the systems and let them evolve under nonequilibrium conditions. In this study, we focus on the nonequilibrium steady state (NESS) which is defined when the number of clusters reaches a

constant value. In our simulations, we observe that clusters of small particles form and change in sizes until the system reaches this nonequilibrium steady state (NESS). The typical time to reach the nonequilibrium steady state is $10^4\tau$.

The particles are driven by an external electric field in the x-direction. The large particles are driven to move to the right and the small particles are driven to move to the left. From $\mathbf{F}^i_{ex} = \mathbf{E}q_i$, we know that the magnitude of the external driving force on the large particles is 12 times the magnitude of the external driving force on the small particles. To quantify how strong the external driving force is compared to the thermal noise, we use the dimensionless driving force $\tilde{f} \equiv \frac{f_{ex}r}{k_BT} = \frac{Eqr}{k_BT}$, where f_{ex} is the magnitude of the external driving force on the small particles, r is the radius of the small particles and k_BT is the thermal energy.

The center of mass of all large colloidal particles drifts due to the external field and the collision with the small particles. When we look into the vibrational motions of the large particles, it is more convenient to choose the center of mass of all large particles as the frame of reference, which we call the COM frame in this report. We only use the COM frame when we present the results of the vibrational motions of the large particles, and use the laboratory frame of reference for other parts of the report. The transformation of the coordinates of particles from the laboratory frame of reference to the COM frame is $\tilde{\mathbf{r}}_i(t) = \mathbf{r}_i(t) - \mathbf{R}_{cm}(t)$, where $\tilde{\mathbf{r}}_i(t)$ is the position vector of the particle i in the COM frame at time t, the $\mathbf{r}_i(t)$ is the position vector of the particle i in the laboratory frame of reference at time t and $\mathbf{R}_{cm}(t) = \frac{1}{N}\sum_{i\in Large}\mathbf{R}_i(t)$ is the position vector of the center of mass of all large particles in the laboratory frame of reference at time t. We use $\mathbf{R}_i$ to denote the position vectors of the large particles while using $\mathbf{r}_i$ to denote the position vectors of any particles. In the COM frame, the displacement vector of one large particle is $\delta\tilde{\mathbf{R}}_i(t) = \tilde{\mathbf{R}}_i(t) - \tilde{\mathbf{R}}_{i0}$, where $\tilde{\mathbf{R}}_{i0}$ is the reference position of the large particle i and does not change with

time in the COM frame. It follows that $\sum_{i \in Large} \delta\tilde{\mathbf{R}}_i(t) = 0$. The displacement vector fields are calculated in microstates (snapshots) of the systems. We also calculate the vibrational spectra of the large particles using the discrete Fourier transform of the time profile of the velocities of the large particles.

$$\mathbf{v}_n(\nu) = \frac{1}{N_{frame}} \sum_{j=0}^{N_{frame}-1} \mathbf{v}_n(t_j) exp[i2\pi\nu t_j] \tag{4.4}$$

$$I_m(\nu) = \frac{\tau^2}{r^2} \frac{1}{N_{particles}} \sum_{n=1}^{N_{particles}} |v_{nm}(\nu)|^2 \tag{4.5}$$

The vibrational spectra are calculated from velocites recorded from $N_{step} = 1000$ consecutive timeframes. The index m denotes the component of the velocities, which can be x or y in our systems. The vibrational intensity is dimensionless due to the prefactor $\frac{\tau^2}{r^2}$.

In this report, we focus on the effects of varying the external driving force and the spring constant of the springs between the large particles. The dimensionless spring constants are $\tilde{K} = 20, 30, 40$, corresponding to $K = \frac{\tilde{K} k_B T}{r^2} = 3.36 \times 10^{-2},\ 5.04 \times 10^{-2},\ 6.72 \times 10^{-2}\ \mathrm{pN}/\mu\mathrm{m}$. The strongest dimensionless driving force is $\tilde{f} = 80$, corresponding to $E = \frac{\tilde{f} k_B T}{qr} = 5.13\ \mathrm{mV/nm}$, which is much lower than the breakdown field of water $E_B = 65\ \mathrm{mV/nm}$ [123].

4.4 Results and discussion

When $\tilde{f} \ll 1$, the small particles distribute homogeneously in the lattice (FIG. 4.2A). When $\tilde{f} \gg 1$, the small particles form lanes in the channels (FIG. 4.2B). The lane formation is observed in size-symmetric colloidal mixtures when the particles are not connected by the springs [93, 125–132]. In our systems, the small particles form lanes, but the large particles do not aggregate, due to the springs. Interestingly, we observe the formation of clusters of small particles with further increasing $\tilde{f}$ (FIG. 4.2C). When we freeze the motion of the large particles, the small particles

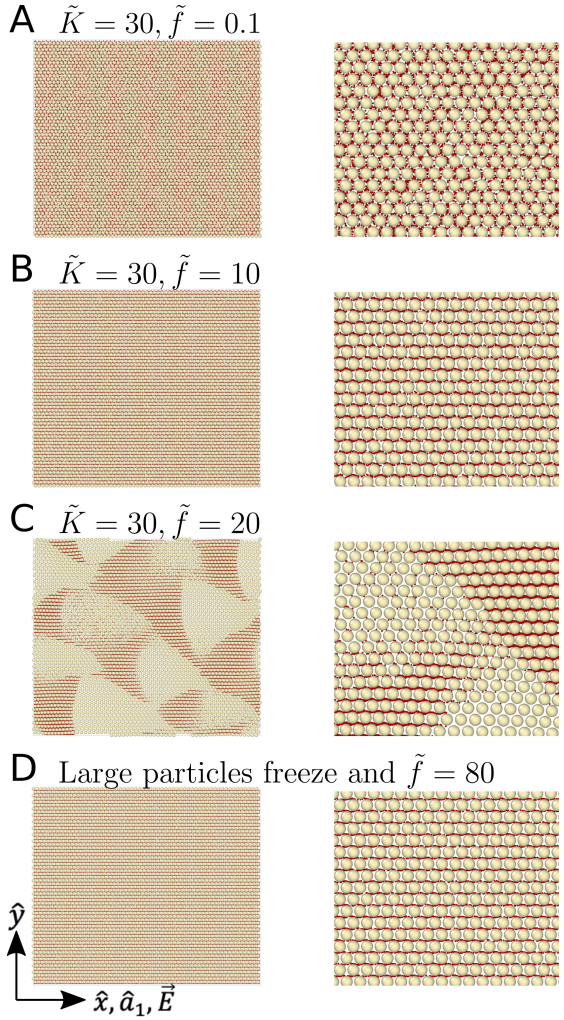

Figure 4.2: Representative snapshots of colloidal mixtures driven in opposite directions with the dimensionless spring constant $\tilde{K} = 30$. The left figures represent the whole simulation boxes, while the right figures are enlarged portions of the left figures. All figures are enlarged 4 times from left to right. In addition, the small particles are enlarged 4 times the original size to make them visible. The snapshots are made using the OVITO package [124]. (A) The dimensionless spring constant and driving force are $\tilde{K} = 30$ and $\tilde{f} = 0.1$, respectively. The driving force is much smaller than the thermal noise, and the small particles distribute homogeneously in the lattice. (B) The dimensionless spring constant and driving force are $\tilde{K} = 30$ and $\tilde{f} = 10$, respectively. The small particles form lanes in the channels between the large particles, while the large particles vibrate randomly. (C) The dimensionless spring constant and driving force are $\tilde{K} = 30$ and $\tilde{f} = 20$, respectively. The small particles aggregate into clusters in the channels between the large particles. (D) The large particles are frozen on their reference positions forming a hexagonal lattice, while the small particles are driven by the dimensionless external force $\tilde{f} = 80$.

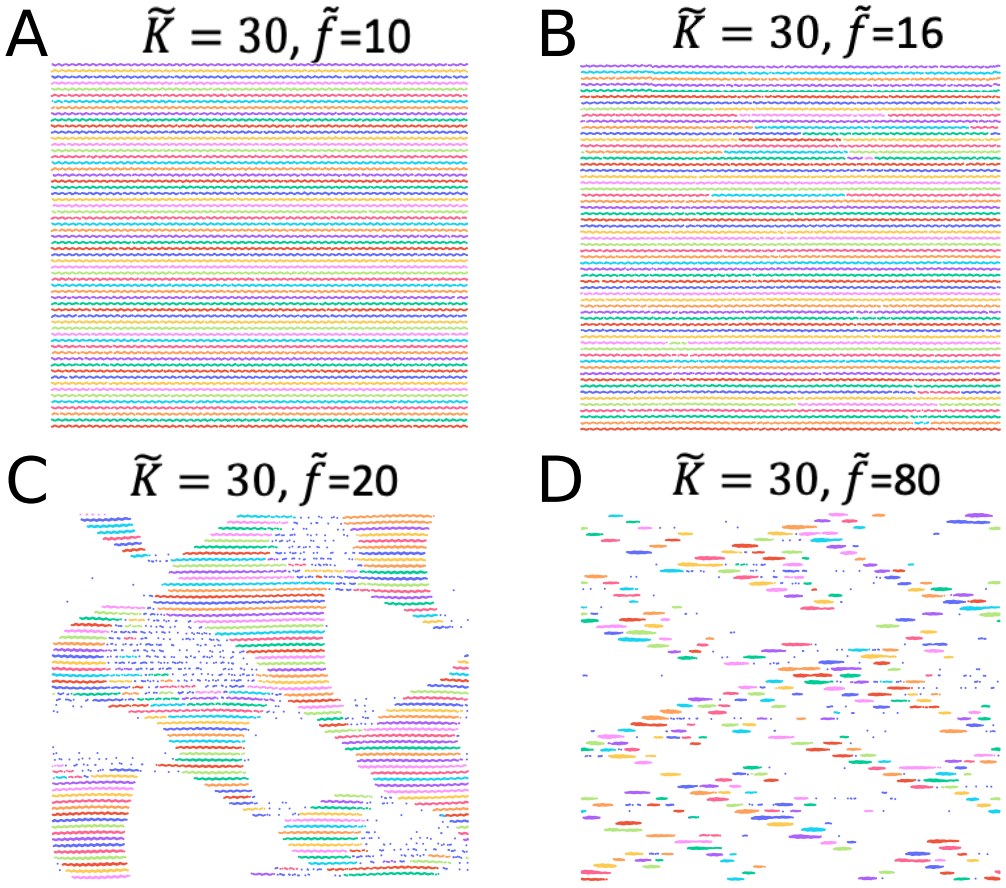

Figure 4.3: Illustrations of different states in the driving colloidal mixtures with the dimensionless spring constant $\tilde{K} = 30$. Here we show only the small particles, which are divided into clusters. The neighboring clusters are distinguished by their colors. The small particles are enlarged 6 times the original size to make them visible. (A) The dimensionless spring constant and driving force are $\tilde{K} = 30$ and $\tilde{f} = 10$, respectively. The system is in the lane state, where the small particles form clusters that are percolated only in the x-direction. (B) The dimensionless spring constant and driving force are $\tilde{K} = 30$ and $\tilde{f} = 16$, respectively. The system is in the intermediate state, where x-percolated clusters and non-percolated clusters coexist. (C) The dimensionless spring constant and driving force are $\tilde{K} = 30$ and $\tilde{f} = 20$, respectively. The system is in the cluster state, where there are only non-percolated clusters. (D) The dimensionless spring constant and driving force are $\tilde{K} = 30$ and $\tilde{f} = 80$, respectively. The system is in the cluster state at a higher field, where the clusters are more round in shape. The clusters in the neighbor channels separate from each other in the x-direction with a nearly constant distance.

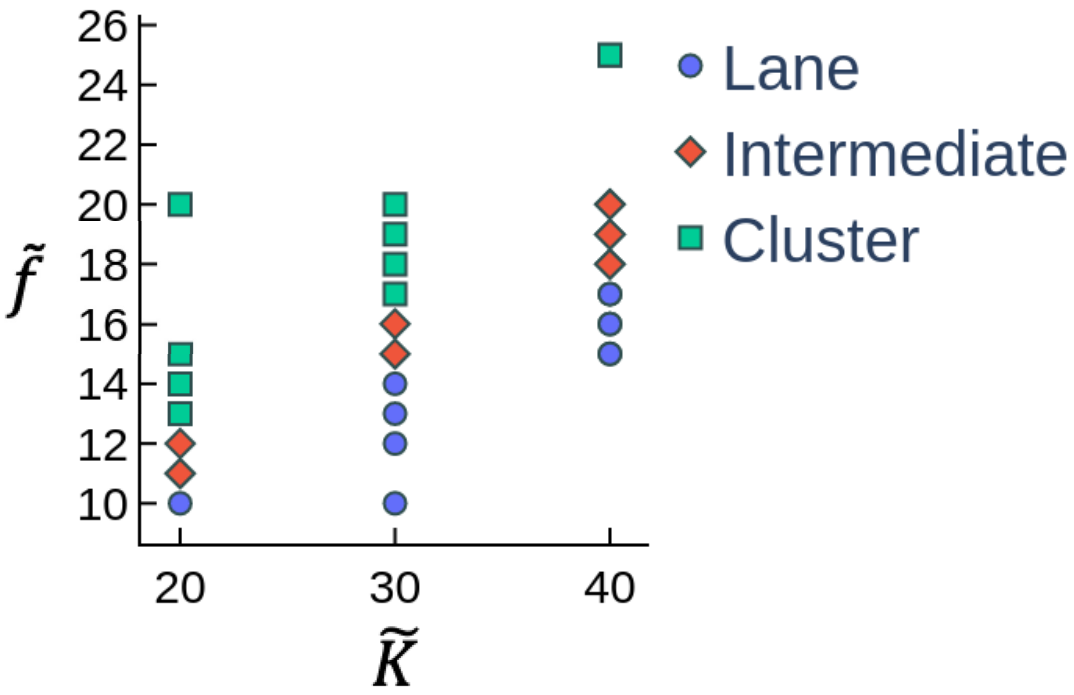

Figure 4.4: Phase diagram of driven colloidal mixtures. The horizontal axis is the dimensionless spring constant and the vertical axis is the dimensionless external driving force. The phase diagram shows that the transition field increases as the spring constant increases. We only show the data points with external driving forces close to the transition.

can still form lanes at high fields, but no cluster formation is observed (FIG. 4.2D). This means that in our systems, lane formation does not require the motion of the large particles, while cluster formation only happens when the large particles are allowed to vibrate.

4.4.1 Lane to cluster transition and phase diagram

First of all, we give the definition of a cluster of small particles. Two small particles are considered *neighbors* if they are within the Debye length λ_D, since they do not interact with each other strongly when they are separated beyond this distance. Two particles are considered in one cluster if we can

find a path of *neighbors* connecting them. One cluster is considered percolated in one direction if this cluster goes across the periodic boundary and forms a loop. If we are in the equilibrium state or $\tilde{f} \ll 1$, the small particles distribute homogeneously in the system, therefore they are all connected and considered to be in one cluster. This cluster is percolated in both x and y directions. The lane state occurs when all clusters are percolated in the x-direction and not percolated in the y-direction. The lanes of small particles drift in the channels between the large particles, and the small particles distribute homogeneously inside the channels. Meanwhile, the cluster state occurs when all clusters are not percolated. It is natural to define one intermediate state, where x-percolated clusters and non-percolated clusters coexist.

With these definitions, we find that when we increase the external driving force, the system evolves from the lane state (FIG. 4.3A) to the intermediate state (FIG. 4.3B), then into the cluster state (FIG. 4.3C and D). In the cluster state, the small particles travel in clusters that have constant velocities and stable shapes. As we further increase the external driving force, the shapes of the clusters become more and more round, which can be quantified by asphericity. We will introduce asphericity in the next subsection. We also observe that the clusters in the neighbor channels are repulsive to each other. They separate from each other in the x-direction at a nearly constant distance. The transition driving force is defined as the lowest driving force where the cluster state emerges. When the spring constant increases, we observe that the transition driving force also increases. This is shown in the phase diagram in FIG. 4.4. In the section on the vibrational motions of the large particles, we further discuss this trend.

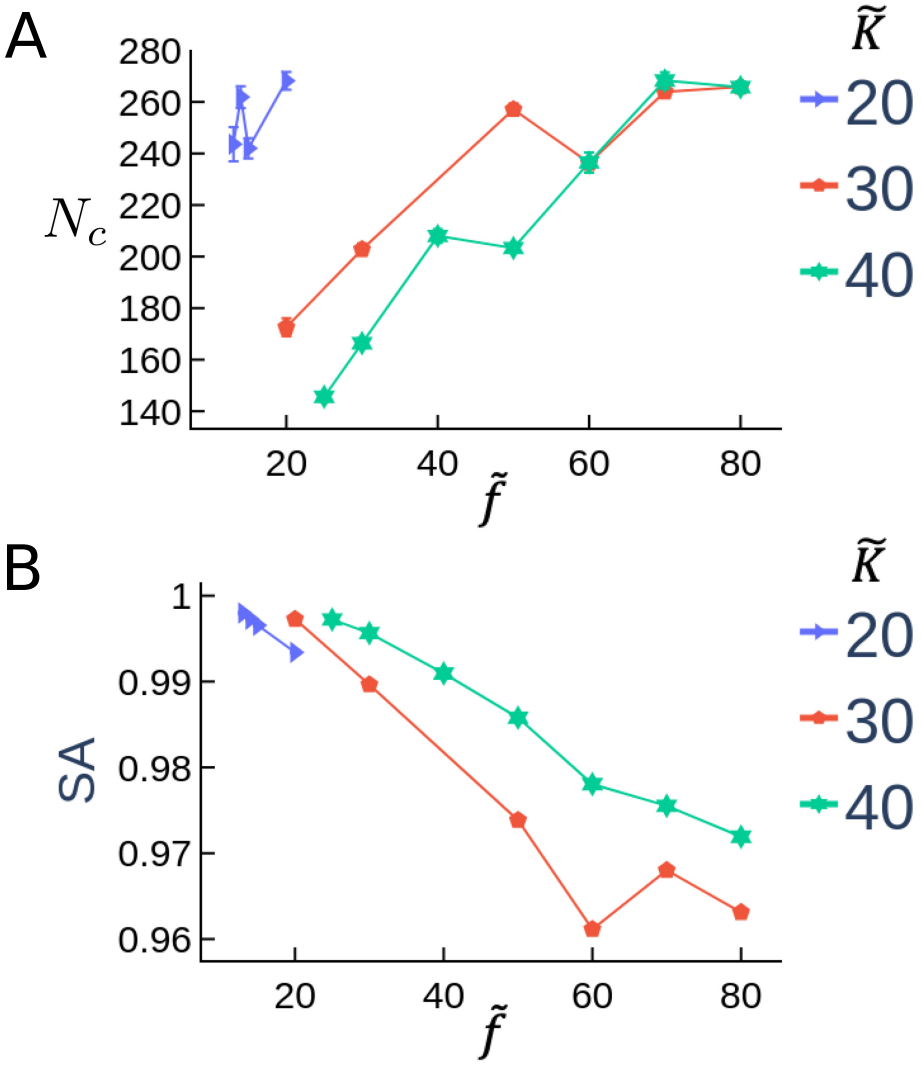

Figure 4.5: Number of clusters and size-weighted average asphericity at different spring constants and driving forces in the cluster state. The data points are mostly for $\tilde{K} = 30$ and $\tilde{K} = 40$. (A) The number of clusters N_c increases as we increase the external driving force. We also observe that at the same external driving force, the number of clusters is larger with smaller spring constants. (B) The size-weighted average asphericity $\bar{A}_w$ quantifies how round the clusters are and gives more weight to larger clusters. Lower asphericity means the shape of the cluster is more spherically symmetric. The plot shows that the large clusters become more spherically symmetric as we increase the external driving force. At the same external driving force, the large clusters are more spherically symmetric in the systems with lower spring constants.

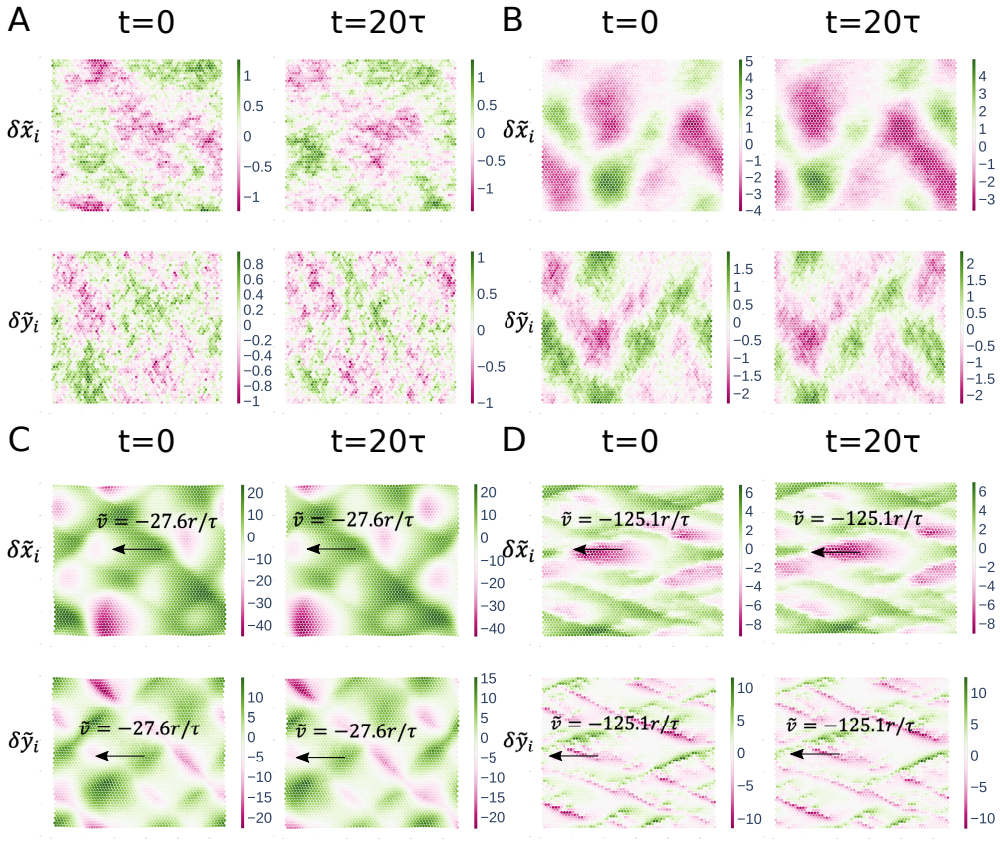

Figure 4.6: Vibrational motions of the large particles in the center of mass (COM) frame. In all figures, from left to right is time evolution, and the top two figures are the vibrational motions in the x-direction while the bottom two figures are the vibrational motions in the y-direction. The displacement vector fields are calculated in two consecutive microstates (snapshots) at t and $t + 20\tau$, where we set the first timestep $t = 0$. The time interval 20τ is chosen because it is large enough to observe the displacement of the pattern. The green color denotes positive values, which means vibrating in the direction of the axis, while the magnenta color means vibrating in the opposite direction of the axis. The color bars show the scale in the unit of small particles' radius r. (A) The dimensionless spring constant and driving force are $\tilde{K} = 30$ and $\tilde{f} = 10$, respectively. The system is in the lane state, and the vibrational motions of the large particles do not show a stable pattern. (B) The dimensionless spring constant and driving force are $\tilde{K} = 30$ and $\tilde{f} = 15$, respectively. The system is in the intermediate state. The vibrational motions of the large particles show patterns when time evolves, but the patterns are not stable (C) The dimensionless spring constant and driving force are $\tilde{K} = 30$ and $\tilde{f} = 20$, respectively. The system is in the cluster state, and stable patterns are observed. The wavepackets are moving at speed $\tilde{v} = -27.6r/\tau$. (D) The dimensionless spring constant and driving force are $\tilde{K} = 30$ and $\tilde{f} = 80$, respectively. The system is in the cluster state at a higher field, where we see stable patterns in the vibrational motions. The angle pattern is due to the separation between the clusters in the neighbor channels. We can see some constant horizontal separations between the wavepackets of displacement vectors, and they are defined as the length scales of the vibrational pattern. The wavepackets are moving at speed $\tilde{v} = -125.1r/\tau$.

4.4.2 Asphericity of the clusters

To quantify the evolution of the shapes of the clusters, we introduce the concept of asphericity. One cluster is a collection of mass points. The gyration tensor of the cluster is defined as

$$S_{mn} = \frac{1}{2N_p^2} \sum_{i=1}^{N_p} \sum_{j=1}^{N_p} ({r_m}^{(i)} - {r_m}^{(j)})({r_n}^{(i)} - {r_n}^{(j)}) \tag{4.6}$$

where m, n denote the directions, i, j denote the particle indices and N_p denotes the number of particles in the cluster. This tensor describes the second moments of positions of a collection of particles. We can always find a coordination system where S_{mn} is diagonal,

$$\boldsymbol{S} = \begin{bmatrix} \lambda_a^2 & 0 \\ 0 & \lambda_b^2 \end{bmatrix} \tag{4.7}$$

where we assume $\lambda_a \leq \lambda_b$. The cluster asphericity is defined as $A = \frac{2(\lambda_a^4 + \lambda_b^4)}{(\lambda_a^2 + \lambda_b^2)^2} - 1$. Under such definition, $A = 1$ when the cluster is completely flat, i.e., $\lambda_a = 0$. $A = 0$ when the cluster is spherically symmetric, i.e., $\lambda_a = \lambda_b$. We observe that the shapes of small clusters do not change significantly when we increase the driving force since small clusters do not interact with the lattice as strongly as large clusters. Thus, we use the size-weighted average asphericity to quantify the change of shapes of clusters, giving more weight to larger clusters. The size-weighted average asphericity is defined as

$$\bar{A}_w = \frac{\sum_{i=1}^{N_c} {N_p}^{(i)} * A^{(i)}}{\sum_{i=1}^{N_c} {N_p}^{(i)}} \tag{4.8}$$

where N_c denotes the number of clusters, ${N_p}^{(i)}$ denotes the number of particles in the ith cluster, and $A^{(i)}$ denotes the asphericity of the ith cluster. FIG. 4.5A shows that the number of clusters N_c increases as the external driving force increases and eventually saturates at high external fields. The average value of the number of clusters is calculated from 10 consecutive timeframes. The errorbar is calculated from the standard deviation of the number of clusters over 10 consecutive timeframes. The system is considered to reach the nonequilibrium steady state (NESS) if the standard deviation of the number of clusters is less than 0.1 of the average number of clusters, i.e., the number of clusters reaches a stable value. This criterion for the nonequilibrium steady state (NESS) also works for the lane state, since the number of clusters is well defined also in the lane state. In the lane state, the number of clusters equals the number of channels, which is 60 in our simulations. In FIG. 4.5B, we see that size-weighted average asphericity decreases when driving force increases. This means that the larger clusters become more spherically symmetric as we increase the driving force. It also shows that the larger clusters are more spherically symmetric in the systems with lower spring constants. This observation and the phase diagram can be understood better when we look at the vibrational motions of the large particles.

4.4.3 Soliton-like vibrational motions of the large particles

When the system evolves from the lane state to the cluster state, we observe that the vibrational motions of the large particles show different behavior in different states. In the lane state, the vibrational amplitude is very small, and does not show stable patterns when time evolves (FIG. 4.6A). In the intermediate state, we observe the correlation between the vibrational motions in different timesteps, but the pattern is not stable (FIG. 4.6B). In the cluster state, we observe a stable pattern (FIG. 4.6C and D). In the COM frame, the large particles vibrate around their reference positions, and the small particles drift to the left at the average velocity $\tilde{\mathbf{v}} = \mathbf{v}_{small} - \mathbf{v}_{large}$, where the $\mathbf{v}_{small}$

and $\mathbf{v}_{large}$ are the average drift velocities of the small and large particles in the lab frame. In the COM frame, the vibrational motions of the large particles in the cluster state satisfy the equation $\delta\tilde{\boldsymbol{R}}_i(t) = \delta\tilde{\boldsymbol{R}}_i(\tilde{\boldsymbol{R}}_{i0} - \tilde{\boldsymbol{v}}t)$, which means the wavepackets of the displacement vectors maintain their shapes while moving at the same velocity as the drift velocity of the small particles. This phenomenon is reminiscent of the soliton-like behavior observed in nonlinear dissipative systems [133–135]. From the vibrational spectra of large particles (FIG. 4.7), we can quantitatively evaluate the transition. In the lane and intermediate state (FIG. 4.7A and B), the vibrational spectra of large particles do not have peaks. In the cluster state (FIG. 4.7C and D), the vibrational spectra show characteristics of non-trigonometric periodic functions. The period corresponds to the time the stable vibrational patterns travel over one box length in the x-direction in each condition. This feature shows that the vibrational motions of large particles have stable patterns that travel at constant velocity in the cluster state. In FIG. 4.7D, we also observe many other peaks that correspond to the length scales of the vibrational pattern. The displacement vectors of the large particles are correlated to the density distribution of the small particles. As the driving force increases, the large clusters have larger asphericity and tend to create more strain in the lattice. On the other hand, the larger the spring constant is, the harder the lattice can deform. That explains why the larger clusters are more spherically symmetric in the systems with lower spring constants. This indicates that the formation of clusters is the result of competition between the instability caused by the external driving force and the stiffness of the lattice. This physical picture is consistent with our observation in the phase diagram that the transition driving force increases as the spring constant increases.

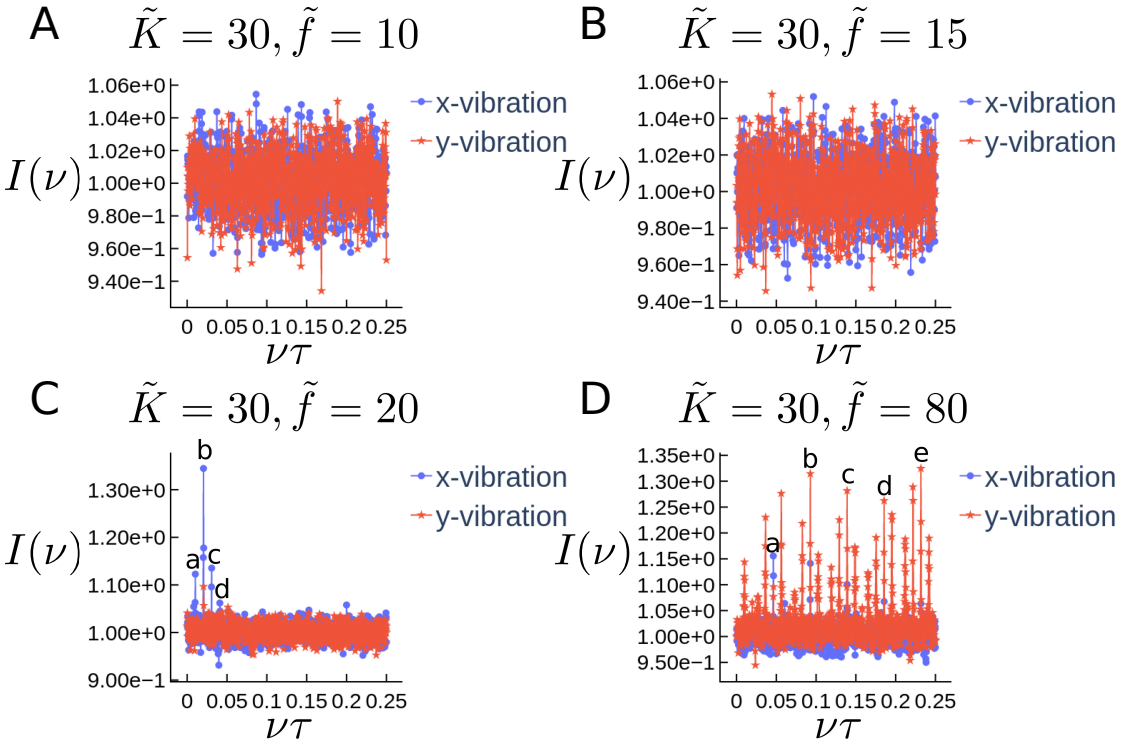

Figure 4.7: Vibrational spectra of large particles in the center of mass (COM) frame. In all figures, the blue lines are the spectra of the vibrational motion in the x-direction and the red lines are the spectra of the vibrational motion in the y direction. The horizontal axis is $\nu\tau$ because we express the frequency ν in the unit of $\frac{1}{\tau}$, where τ is the time unit in our simulations. (A) The dimensionless spring constant and driving force are $\tilde{K} = 30$ and $\tilde{f} = 10$, respectively. The system is in the lane state, and the vibrational spectra of the large particles do not have peaks. (B) The dimensionless spring constant and driving force are $\tilde{K} = 30$ and $\tilde{f} = 15$, respectively. The system is in the intermediate state, and the vibrational spectra of the large particles do not have peaks. (C) The dimensionless spring constant and driving force are $\tilde{K} = 30$ and $\tilde{f} = 20$, respectively. The system is in the cluster state, and the vibrational spectra of the large particles show several peaks. The four peaks a, b, c, d marked in the graph correspond to $\nu\tau = 0.0103,\ 0.0205,\ 0.0308,\ 0.0410$ respectively. They are all multiples of the frequency of the first peak $\nu_a\tau = 0.0103$, which is the characteristic of a non-trigonometric periodic function with a period of $T = \frac{1}{\nu_a} = 97.1\tau$. This period corresponds to the time the stable vibrational patterns travel over one box length in the x-direction. (D) The dimensionless spring constant and driving force are $\tilde{K} = 30$ and $\tilde{f} = 80$, respectively. The system is in the cluster state, and the vibrational spectra of the large particles show several peaks. The five peaks a, b, c, d, e marked in the graph correspond to $\nu\tau = 0.0463,\ 0.0928,\ 0.1390,\ 0.1855,\ 0.2318$ respectively. They are all multiples of the frequency of the first peak $\nu_a\tau = 0.0463$, which is the characteristic of a non-trigonometric periodic function with a period of $T = \frac{1}{\nu_a} = 21.6\tau$. This period corresponds to the time the stable vibrational patterns travel over one box length in the x-direction.

4.5 Conclusions

In size-asymmetric charged colloidal compounds with springs attached between the large particles, we observe various steady states including a cluster state when the external driving force is higher than the lane state. In the cluster state, the small particles form clusters that travel at constant velocities with stable shapes and we observe soliton-like behavior in the vibrational motions of the large particles in the COM frame. As we increase the external field, the size-weighted average asphericity of clusters of small particles decreases, meaning that large clusters become more spherically symmetric. At the same time, it is more difficult for the lattice to deform with higher spring constants. Since no cluster state is observed when the large particles are frozen, this state is distinguished from the cluster formation in the active fluids [136–139]. The soliton-like vibrational motions are also different from the solitary wave observed in the nonlinear active lattices [133, 140] since our systems do not have active frictions and nonlinear springs. The cluster formation and soliton-like vibrational motions in our model systems are the result of the coupling between vibrational and fluid-like degrees of freedom under nonequilibrium conditions, which is similar to the solitons observed in the drainage of foams [120, 121]. In a driven binary lattice gas model [141, 142], phase separation with a long range order is also observed in the nonequilibrium steady state. In their model, the instability is induced by fluctuation correlations of the charge field, which could also be the origin of instability in our systems. It is important to note that the Debye length in our system is smaller than the length of the clusters since the system is on a surface in contact with an electrolyte (a reservoir containing ions), which provides electrostatic screening. In a system with long-range Coulombic interactions, the requirement of charge neutrality will forbid the formation of clusters. In a driven colloidal binary mixture with low volume fraction and long-range interactions, it was found that hydrodynamics play an important role in the self-assembly

process [143]. In our systems, the hydrodynamics interactions are expected to be screened because the momentum will be transferred to the lattice of the large particles. However, hydrodynamics could still affect the morphology of the clusters in length scales of the order of the lattice constant, which can be a subject of future investigation. It should be noted that our systems have a very large parametric space, partly due to the size and charge asymmetries. We study extremely large size ratio and number ratio so that the small particles act like continuous flow over the size of the large particles. If the size ratio is not sufficiently large, we do not expect to observe the aggregation of the small particles. We also study a large overall density of the particles so that the scattering process between small and large particles is important. The phenomenon in this report is expected to be robust under such conditions, although we have not fully explored the large parametric space. Our work provides insight into the nonequilibrium organization behavior of size- and charge-asymmetric colloidal mixtures.

CHAPTER 5
CONCLUSION AND FUTURE WORK

5.1 Summary of key findings and significance

Throughout the thesis, theories and simulations over different length and time scales elucidate rich phenomena in the self-assembly, transport, and applications of materials with porous and networked structures. The highly directional interactions lead to complicated free energy landscapes, vibrational motions, and nonequilibrium behavior of the materials.

As shown in Chapter 2, the nucleation and growth processes of network structures need to be described by graphs. The topological information is encoded in the graphs, including connectivity and correlations between neighboring edges. The free energy of the clusters depends on their molecular masses and connectivity described by the graphs. In classical nucleation theory, the clusters are hypothesized to be spherical, and the free energy only depends on their sizes. The free energy landscapes of network structures are much more complicated, and competition between different pathways of self-assembly is sensitive to the experimental conditions. The conceptual framework in this work can be expanded to the self-assembly of a mixture of different building blocks (heterogeneous nucleation). The idea of heterogeneous nucleation has been employed by C. Evans et al. [144] to realize physical learning.

One of the motivations for studying network structures is their natural porosity. The natural porosity leads to many potential applications, including water purification, energy harvesting, catalysis, gas storage, and drug delivery. In Chapter 3, we discussed the possible misinterpretation of experimental advancements in water purification with covalent organic framework (COF) films.

The insight into the entropic origin of dye-COF interactions supports the hypothesis that COF films serve as adsorbents rather than size-sieving membranes. This finding could clarify the situation in the field and lead to more solid development of water purification technology using COF films. There are many routes to realizing size-sieving filtration using COF-related materials. One obvious option is to increase the crystallinity of COF membranes. It has been reported that COF membranes with improved crystallinity can reject dye molecules with a size-sieving mechanism [145]. COF membranes with oriented pores are also found to be ideal nanofluidic devices [146]. Another promising route is to synthesize COF-based hybrid membranes, which can be applied for water desalination with high efficiency [147].

The nonequilibrium phase transition in oppositely driven flows is applicable to charged colloidal mixtures and pedestrian dynamics. One limitation of the study is the dimensionality of the system. Two-dimensional size-asymmetric colloidal mixtures are realizable at the air-water interface [148]. Pedestrian systems are more naturally two-dimensional, but the size asymmetry is not easy to control. In a three-dimensional periodic system, small particles can find channels to avoid collision with large particles. Since the coupling between small and large particles is essential for cluster formation, disorder in three-dimensional systems is required. Gel is an ideal system for the combination of transport of small particles and an elastic matrix.

5.2 Opportunities for future research

5.2.1 Preliminary results on polyelectrolyte gels

The thesis is focused on network structures that have periodicity. The topology of periodic networks is relatively simpler to understand than disordered networks. However, richer phenomena emerge in disordered network systems, e.g., gels and neural networks. Polyelectrolyte gels are flexible semisolid structures holding a large quantity of fluid in the interstitial spaces of crosslinked

polymeric networks. They have charged groups or ionizable moieties stabilized by several interactions. They are also a model system for understanding biological systems with fixed charge groups.

Ionic conductivity is one ubiquitous property of polyelectrolyte gels. It is substantial for many engineering and medical applications. One important question is how molar conductivity depends on the concentration of ions. In electrolyte solutions, it was found by Friedrich Kohlrausch that the molar conductivity decreases as the concentration of ions increases. The dependence is expressed as Kohlrausch's law:

$$\Lambda_m = \Lambda_m^\circ - K\sqrt{c} \tag{5.1}$$

Where $\Lambda_m = \frac{\kappa}{c}$ is the molar conductivity (κ is the ionic conductivity and c is the concentration of ions), and K is the Kohlrausch coefficient. Lars Onsager developed a theory for electrolyte conductivity based on the Debye-Hückel approximation. The theory is now known as Debye-Hückel-Onsager (DHO) theory [149]. The DHO theory states that the decrease in molar conductivity comes from two effects: relaxation effect and electrophoretic effect (see Figure 5.1).

However, the situation is completely different in polyelectrolyte gels. As Li et al. found in polyelectrolyte gels [150], the molar conductivity increases as the pore size of the polyelectrolyte gel decreases. The ion concentration increases as the pore size decreases. It follows that the molar conductivity increases as the ion concentration increases. The difference is that one type of ion is fixed on a polymeric network. The Manning parameter $\xi = l_B/b$ is the ratio of the Bjerrum length to the distance between monomers on the polymer chain [151]. When $\xi < |z_c|^{-1}$, the gel-counterion interaction is governed by Debye-Hückel interaction. When $\xi > |z_c|^{-1}$, counterions condense on the chains until $\xi_{net} = |z_c|^{-1}$. The ratio of free ions has an analytic expression at the dilute limit: $f = \frac{0.866}{|z_c|\xi} = \frac{0.866}{|z_c|(l_B/b)}$. The molar conductivity is then estimated by $\frac{\Lambda_m}{\Lambda_m^\circ} = f$. However, this result is based on the assumption that the polyelectrolyte chain is infinitely long. Li et al.

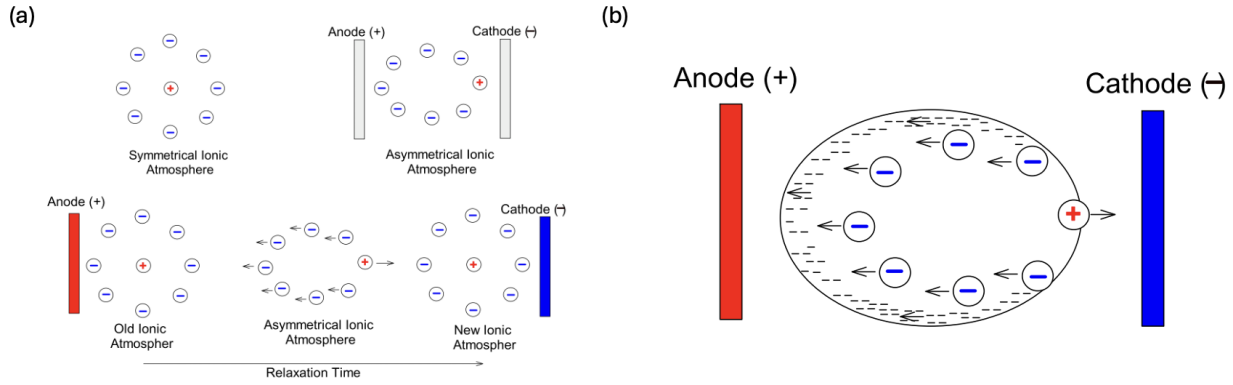

Figure 5.1: Schematics of Debye-Huckel-Onsager theory. (a) Relaxation effect. When positive ion drifts, the negative atmosphere is asymmetric around it before a new symmetric atmosphere forms. This asymmetric atmosphere will drag the positive ion. (b) Electrophoretic effect. The fluid flow will be on the opposite direction due to the drift of the negative atmosphere.

found the effect of shrinking the pore size as discussed above.

The situation becomes more complicated when we consider copolymer gels, where charged monomers and neutral monomers are randomly distributed on the network. Collaborating with an experimental group, we found a reverse dependency of molar conductivity on the ion concentration by changing the charge fraction $p_{charge} = \frac{[Charge]}{[Charge]+[Neutral]}$ (see Figure 5.2). The charged monomer is 2-Acrylamido-2-methylpropane sulfonic acid (AMPS) and the neutral monomer is acrylamide (AM) in the experimental system.

To understand the ionic molar conductivity in copolymer gel, it is crucial to elucidate how the gel swells in water. The swelling behavior determines the pore size of the gel network. The swelling ratio in experiments is defined as $\eta = \frac{V}{V_0}$, where V is the volume of the gel after swelling ($\Pi = 0$). V_0 is the initial water volume. Below is a simple scaling theory for estimating how the end-to-end distance scales with the number of monomers between the nodes at different charge fractions.

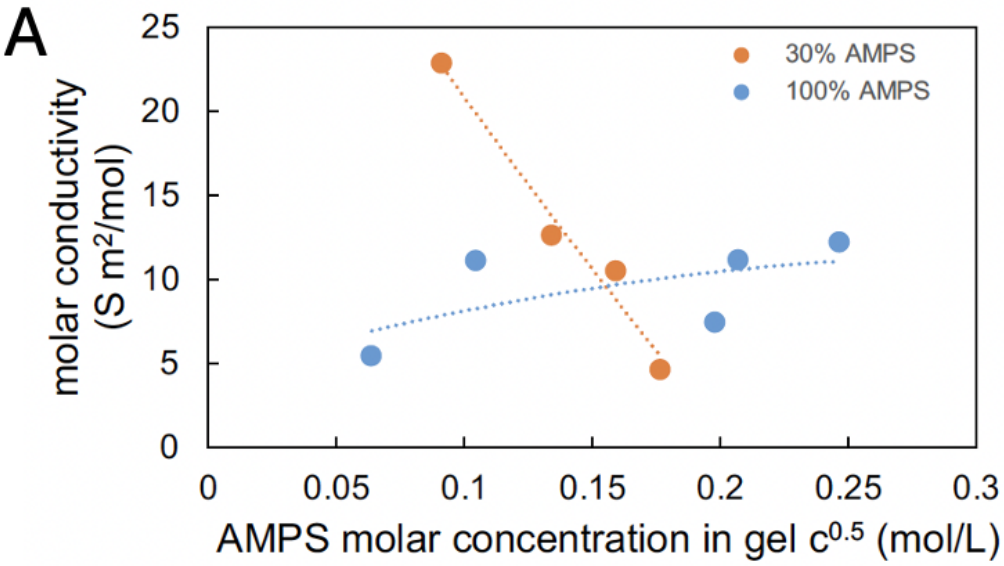

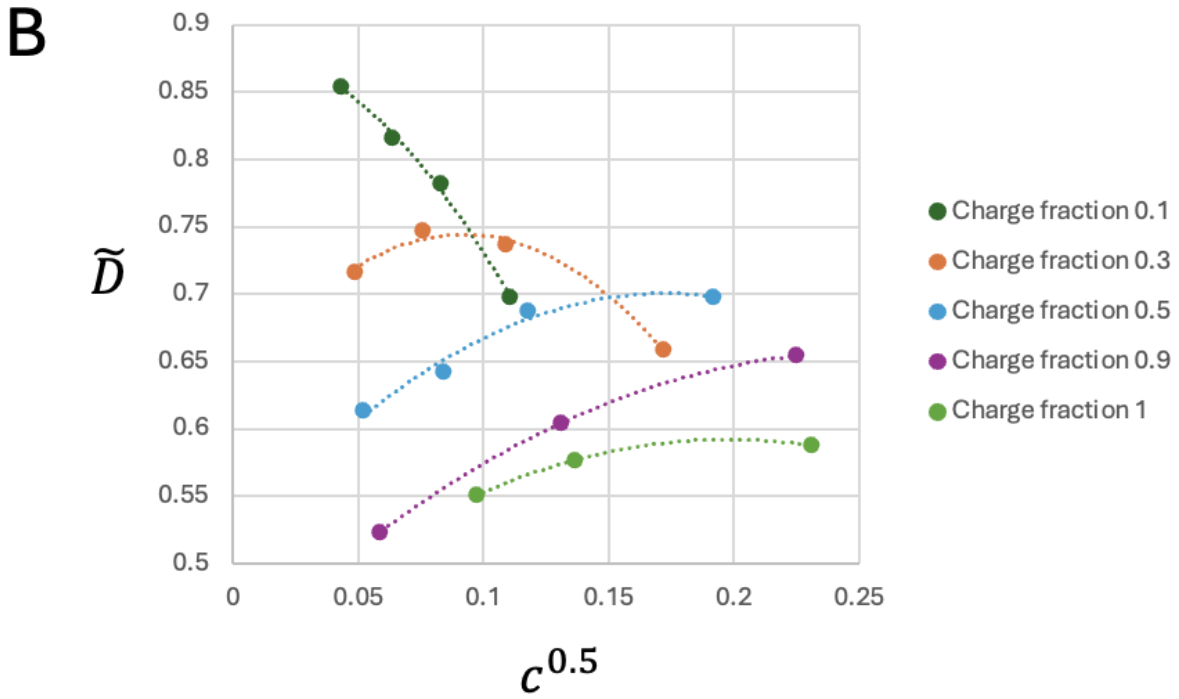

Figure 5.2: Dependency of molar conductivity on the ionic concentration at different charge fraction (A) Experimental data at different charge fraction. (B) Simulation results of normalized diffusivity versus different molar concentration. The normalized diffusivity is calculated by $\tilde{D} = \frac{D}{D_0}$, where D_0 is the diffusivity of the ion in infinitely dilute solution.

Let us assume a fixed total monomer concentration $c_0 = 1\ M$. The initial amount of monomers is $n_0 = c_0 V_0$. The crosslinker concentration ratio is defined as $p_c = \frac{c_c}{c_0}$, therefore the amount of crosslinker is $n_c = V_0 p_c c_0$. The amount of crosslinker is proportional to the number of nodes in the network, which is also proportional to the number of chains in the system: $n_{chain} = An_c$, where A is a constant. The number of monomers per chain is $N_m = \frac{n_0}{n_{chain}} = \frac{n_0}{An_c} = \frac{1}{Ap_c}$. The end-to-end distance after swelling (pore size) is dependent on the number of monomers per chain: $R_e = N_m^\nu b$, where ν should only depend on the charge portion and $b = 0.3\ \mathrm{nm}$ is the Kuhn length. The number of volumes contained by the chains and nodes is linearly dependent on the number of chains: $N_{volume} = Bn_{chain}$. The final volume of the whole gel should be $V = N_{volume} R_e^3 = ABn_c N_m^{3\nu} b^3 = ABV_0 c_0 p_c \left(\frac{1}{Ap_c}\right)^{3\nu} b^3$. It follows that the swelling ratio is $\eta = ABc_0 p_c \left(\frac{1}{Ap_c}\right)^{3\nu} b^3$. The experimentally measured exponent is $m = 1 - 3\nu$, therefore we can get $\nu = \frac{1-m}{3}$. The exponents ν for different charge fractions are listed in Table 5.1. For pure polyelectrolyte gel, $R_e = N_m^{0.997} b$, which is consistent with the expectation that the chains are highly stretched in polyelectrolyte gel.

AMPS weight percentage	**m**	ν
0	-0.303	0.434333
30	-1.129	0.709667
50	-1.158	0.719333
70	-1.244	0.748000
80	-1.259	0.753000
90	-1.600	0.866667
100	-1.991	0.997000

Table 5.1: Scaling exponent of copolymer gel. The swelling ratio scales with portion of crosslinkers $\eta \sim p_c^m$ and end-to-end distance scales with the number of monomers per chain $R_e = N_m^\nu b$.

The copolymer gel has a much more complicated potential landscape than the polyelectrolyte gel due to the random distribution of charged monomers on the network. Therefore, a model based on random networks is necessary for understanding the ionic mobility in copolymer gels. The

methodology proposed here can also be applied to systems with disordered network structures, e.g., cellular and neural systems.

5.2.2 Summary of future directions

Briefly, the work in this dissertation can be extended in the following directions: self-assembly of a mixture of different building blocks, design of COF-based materials with functional groups and hybridization with other materials, and transport in disordered networks. Graph theory serves as the right language for describing the structures of networked materials, and new physics and chemistry are to be discovered when the systems are driven far from equilibrium.

REFERENCES

(1) Zeldovich, Y. B. On the theory of new phase formation: cavitation. *Acta Physicochem. USSR* **1943**, *18*, 1.

(2) Fisher, M. E. The Theory of Condensation and the Critical Point. *Physics Physique Fizika* **1967**, *3*, 255.

(3) Jacobs, W. M.; Reinhardt, A.; Frenkel, D. Communication: Theoretical Prediction of Free-Energy Landscapes for Complex Self-Assembly. J. *Chem. Phys.* **2015**, *142*.

(4) Zhang, Y.; Yang, D.; Wang, P.; Ke, Y. Building Large DNA Bundles via Controlled Hierarchical Assembly of DNA Tubes. *ACS Nano* **2023**, *17*, 10486–10495.

(5) Webber, M. J.; Appel, E. A.; Meijer, E. W.; Langer, R. Supramolecular Biomaterials. *Nature Materials* **2016**, *15*, 13–26.

(6) Braiding, branching and chiral amplification of nanofibres in supramolecular gels. *Nature Chemistry* **2019**, *11*, 375–381.

(7) Solvent-mediated assembly of atom-precise gold–silver nanoclusters to semiconducting one-dimensional materials. *Nature Communications* **2020**, *11*, 2229.

(8) Carpenter, B. P.; Talosig, A. R.; Rose, B.; Di Palma, G.; Patterson, J. P. Understanding and controlling the nucleation and growth of metal-organic frameworks. *Chemical Society Reviews* **2023**, *52*, 6918–6937.

(9) Koner, K. et al. Bottom-up Synthesis of Crystalline Covalent Organic Framework Nanosheets, Nanotubes, and Kippah Vesicles: An Odd–Even Effect Induction. *J. Am. Chem. Soc* **2023**, *145*, 14475–14483.

(10) Zhuo, M. P.; Wu, J. J.; Wang, X. D.; Tao, Y. C.; Yuan, Y.; Liao, L. S. Hierarchical self-assembly of organic heterostructure nanowires. *Nature Communications* **2019**, *10*, 3839.

(11) Han, S.; Zhu, J.; Uliana, A. A.; Li, D.; Zhang, Y.; Zhang, L.; Wang, Y.; He, T.; Elimelech, M. Microporous organic nanotube assisted design of high performance nanofiltration membranes. *Nature Communications* **2022**, *13*, 7954.

(12) Guo, S.-D.; Stoddart, J. F.; Cai, K. Making Organic Nanotubes with Precision. *Chem* **2023**, *9*, 1071–1073.

(13) Liu, Z.; Liu, G.; Wu, Y.; Cao, D.; Sun, J.; Schneebeli, S. T.; Nassar, M. S.; Mirkin, C. A.; Stoddart, J. F. Assembly of Supramolecular Nanotubes from Molecular Triangles and 1,2-Dihalohydrocarbons. *J. Am. Chem. Soc* **2014**, *136*, 16651–16660.

(14) Sendai, T.; Biswas, S.; Aida, T. Photoreconfigurable Supramolecular Nanotube. *Journal of the American Chemical Society* **2013**, *135*, 11509–11512.

(15) Fundamental study of nonclassical nucleation mechanisms in iron. *Acta Materialia* **2022**, *226*, 117655.

(16) Chen, H.; Li, M.; Lu, Z.; Wang, X.; Yang, J.; Wang, Z.; Zhang, F.; Gu, C.; Zhang, W.; Sun, Y.; Sun, J.; Zhu, W.; Guo, X. Multistep nucleation and growth mechanisms of organic crystals from amorphous solid states. *Nature Communications* **2019**, *10*, 3872.

(17) Wang, H. et al. Hierarchical Self-Assembly of Nanowires on the Surface by Metallo-Supramolecular Truncated Cuboctahedra. *J. Am. Chem. Soc* **2021**, *143*, 5826–5835.

(18) Assembly of a Porous Supramolecular Polyknot from Rigid Trigonal Prismatic Building Blocks. *Journal of the American Chemical Society* **2019**, *141*, 12998–13002.

(19) Ding, J.; Guan, X.; Lv, J.; Chen, X.; Zhang, Y.; Li, H.; Zhang, D.; Qiu, S.; Jiang, H.-L.; Fang, Q. Three-Dimensional Covalent Organic Frameworks with Ultra-Large Pores for Highly Efficient Photocatalysis. *J. Am. Chem. Soc* **2023**, *145*, 3248–3254.

(20) Chen, Z.; Li, P.; Zhang, X.; Mian, M. R.; Wang, X.; Li, P.; Liu, Z.; O'Keeffe, M.; Stoddart, J. F.; Farha, O. K. Reticular Exploration of Uranium-Based Metal-Organic Frameworks with Hexacarboxylate Building Units. *Nano Res* **2021**, *14*, 376–380.

(21) Balancing volumetric and gravimetric uptake in highly porous materials for clean energy. *Science* **2020**, *368*, 297–303.

(22) Chen, Z.; Li, P.; Zhang, X.; Li, P.; Wasson, M. C.; Islamoglu, T.; Stoddart, J. F.; Farha, O. K. Reticular Access to Highly Porous acs-MOFs with Rigid Trigonal Prismatic Linkers for Water Sorption. *J. Am. Chem. Soc* **2019**, *141*, 2900–2905.

(23) Tripodal Organic Cages with Unconventional CH···O Interactions for Perchlorate Remediation in Water. *Journal of the American Chemical Society* **2023**, *145*, 21723–21728.

(24) Mabesoone, M. F. J.; Palmans, A. R. A.; Meijer, E. W. Solute–Solvent Interactions in Modern Physical Organic Chemistry: Supramolecular Polymers as a Muse. *J. Am. Chem. Soc* **2020**, *142*, 19781–19798.

(25) Li, P.; Li, P.; Ryder, M. R.; Liu, Z.; Stern, C. L.; Farha, O. K.; Stoddart, J. F. Interpenetration Isomerism in Triptycene-Based Hydrogen-Bonded Organic Frameworks. *Angewandte Chemie* **2019**, *131*, 1678–1683.

(26) Clausen, C. H.; Jensen, J.; Castillo, J.; Dimaki, M.; Svendsen, W. E. M. o. S. D. D. N. Qualitative Mapping of Structurally Different Dipeptide Nanotubes. *Nano Letter* **2008**, *8*, 4066–4069.

(27) Electrostatic force microscopy of self-assembled peptide structures. *Scanning* **2011**, *33*, 201–207.

(28) Cleveland, J. P.; Anczykowski, B.; Schmid, A. E.; Elings, V. B. Energy Dissipation in Tapping-Mode Atomic Force Microscopy. *Appl. Phys. Lett* **1998**, *72*, 2613–2615.

(29) Stark, M.; Möller, C.; Müller, D. J.; Guckenberger, R. From Images to Interactions: High-Resolution Phase Imaging in Tapping-Mode Atomic Force Microscopy. *Biophys. J* **2001**, *80*, 3009–3018.

(30) Koner, K.; Karak, S.; Kandambeth, S.; Karak, S.; Thomas, N.; Leanza, L.; Perego, C.; Pesce, L.; Capelli, R.; Moun, M.; Bhakar, M.; Ajithkumar, T. G.; Pavan, G. M.; Banerjee, R. Porous covalent organic nanotubes and their assembly in loops and toroids. *Nature Chemistry* **2022**, *14*, 507–514.

(31) Li, P.; Ryder, M. R.; Stoddart, J. F. Hydrogen-Bonded Organic Frameworks: A Rising Class of Porous Molecular Materials. *Accounts of Materials Research* **2020**, *1*, 77–87.

(32) Cates, M. E.; Candau, S. J. Statics and dynamics of worm-like surfactant micelles. *Journal of Physics: Condensed Matter* **1990**, *2*, 6869–6892.

(33) Simulation of gas adsorption on a surface and in slit pores with grand canonical and canonical kinetic Monte Carlo methods. *Physical Chemistry Chemical Physics* **2012**, *14*, 11112–11118.

(34) Förster, G. D.; Swinburne, T. D.; Jiang, H.; Kauppinen, E.; Bichara, C.; Semi-Grand, A. Canonical Kinetic Monte Carlo Study of Single-Walled Carbon Nanotube Growth. *AIP Adv* **2021**, *11*, 045306.

(35) Bortz, A.; Kalos, M.; Lebowitz, J. A new algorithm for Monte Carlo simulation of Ising spin systems. *Journal of Computational physics* **1975**, *17*, 10–18.

(36) Cai, R.; Kangasluoma, J. The proper view of cluster free energy in nucleation theories. *Aerosol Science and Technology* **2022**, *56*, 757–766.

(37) Ford, I. J. In *Proceedings of the Institution of Mechanical Engineers, Part C: Journal of Mechanical Engineering Science*, 2004; Vol. 218, pp 883–899.

(38) Kalikmanov, V. I. In *Nucleation Theory*; Springer Netherlands: Dordrecht, 2013, pp 17–41.

(39) Karthika, S.; Radhakrishnan, T. K.; Kalaichelvi, P. A Review of Classical and Nonclassical Nucleation Theories. *Cryst. Growth Des* **2016**, *16*, 6663–6681.

(40) Schnitzer, T.; Preuss, M. D.; van Basten, J.; Schoenmakers, S. M. C.; Spiering, A. J. H.; Vantomme, G.; Meijer, E. W. How Subtle Changes Can Make a Difference: Reproducibility in Complex Supramolecular Systems. *Angewandte Chemie - International Edition* **2022**, *61*, e202206738.

(41) Zhao, Y.; Kawano, H.; Yamagishi, H.; Otake, S.; Itoh, Y.; Huang, H.; Meijer, E. W.; Aida, T. Pathway Complexity in Nanotubular Supramolecular Polymerization: Metal-Organic Nanotubes with a Planar-Chiral Monomer. *J. Am. Chem. Soc* **2023**, *145*, 13920–13928.

(42) Pathway complexity in fibre assembly: from liquid crystals to hyper-helical gelmorphs. *Chemical Science* **2023**, *14*, 11389–11401.

(43) Sajfutdinow, M.; Jacobs, W. M.; Reinhardt, A.; Schneider, C.; Smith, D. M. Direct Observation and Rational Design of Nucleation Behavior in Addressable Self-Assembly. *Proc. Natl. Acad. Sci* **2018**, *115*, 5877–5886.

(44) Van der Tol, J. J.; Vantomme, G.; Meijer, E. W. Solvent-Induced Pathway Complexity of Supramolecular Polymerization Unveiled Using the Hansen Solubility Parameters. *Journal of the American Chemical Society* **2023**, *145*, 17987–17994.

(45) Schoenmakers, S. M. C.; Spiering, A. J. H.; Herziger, S.; Böttcher, C.; Haag, R.; Palmans, A. R. A.; Meijer, E. W. Structure and Dynamics of Supramolecular Polymers: Wait and See. *ACS Macro Lett* **2022**, *11*, 711–715.

(46) Aida, T.; Meijer, E. W.; Stupp, S. I. Functional Supramolecular Polymers. *Science* **2012**, *335*, 813–817.

(47) Molecular ordering of organic molten salts triggered by single-walled carbon nanotubes. *Science* **2003**, *300*, 2072–2074.

(48) Tian, Y.; Guo, Y.; Dong, X.; Wan, X.; Cheng, K.-H.; Chang, R.; Li, S.; Cao, X.; Chan, Y.-T.; Sue, A. C. H. Synthesis of Covalent Organic Pillars as Molecular Nanotubes with Precise Length, Diameter and Chirality. *Nat. Synth* **2023**, *2*, 395–402.

(49) Wang, S.; Lee, S.; Du, J. S.; Partridge, B. E.; Cheng, H. F.; Zhou, W.; Dravid, V. P.; Lee, B.; Glotzer, S. C.; Mirkin, C. A. The emergence of valency in colloidal crystals through electron equivalents. *Nature Materials* **2022**, *21*, 580.

(50) Koner, K.; Das, S.; Mohata, S.; Duong, N. T.; Nishiyama, Y.; Kandambeth, S.; Karak, S.; Reddy, C. M.; Banerjee, R. Viscoelastic Covalent Organic Nanotube Fabric via Macroscopic Entanglement. *Journal of the American Chemical Society* **2022**, *144*, 16052–16059.

(51) Fenton, J. L.; Burke, D. W.; Qian, D.; Cruz, M. O. D. L.; Dichtel, W. R. Polycrystalline Covalent Organic Framework Films Act as Adsorbents, Not Membranes. *Journal of the American Chemical Society* **2021**, *143*, 1466–1473.

(52) Cote, A. P.; Benin, A. I.; Ockwig, N. W.; Keeffe, M. O.; Matzger, A. J.; Yaghi, O. M. Porous, Crystalline, Covalent Organic Frameworks. *Science* **2005**, *310*, 1166–1171.

(53) Diercks, C. S.; Yaghi, O. M. The atom, the molecule, and the covalent organic framework. *Science* **2017**, *355*.

(54) El-Kaderi, H. M.; Hunt, J. R.; Mendoza-Cortés, J. L.; Côté, A. P.; Taylor, R. E.; O'Keeffe, M.; Yaghi, O. M. Designed Synthesis of 3D Covalent Organic Frameworks. *Science* **2007**, *316*, 268–273.

(55) Lohse, M. S.; Bein, T. Covalent Organic Frameworks: Structures, Synthesis, and Applications. *Advanced Functional Materials* **2018**, *28*.

(56) Alahakoon, S. B.; Thompson, C. M.; Occhialini, G.; Smaldone, R. A. Design Principles for Covalent Organic Frameworks in Energy Storage Applications. *ChemSusChem* **2017**, *10*, 2116–2129.

(57) Li, T.; Zhang, W. D.; Liu, Y.; Li, Y.; Cheng, C.; Zhu, H.; Yan, X.; Li, Z.; Gu, Z. G. A two-dimensional semiconducting covalent organic framework with nickel(II) coordination for high capacitive performance. *Journal of Materials Chemistry A* **2019**, *7*, 19676–19681.

(58) Mulzer, C. R.; Shen, L.; Bisbey, R. P.; McKone, J. R.; Zhang, N.; Abruña, H. D.; Dichtel, W. R. Superior charge storage and power density of a conducting polymer-modified covalent organic framework. *ACS Central Science* **2016**, *2*, 667–673.

(59) Xu, H.; Gao, J.; Jiang, D. Stable, crystalline, porous, covalent organic frameworks as a platform for chiral organocatalysts. *Nature Chemistry* **2015**, *7*, 905–912.

(60) Liu, J.; Wang, N.; Ma, L. Recent Advances in Covalent Organic Frameworks for Catalysis. *Chemistry - An Asian Journal* **2020**, *15*, 338–351.

(61) Li, H.; Chang, J.; Li, S.; Guan, X.; Li, D.; Li, C.; Tang, L.; Xue, M.; Yan, Y.; Valtchev, V.; Qiu, S.; Fang, Q. Three-Dimensional Tetrathiafulvalene-Based Covalent Organic Frameworks for Tunable Electrical Conductivity. *Journal of the American Chemical Society* **2019**, *141*, 13324–13329.

(62) Meng, Z.; Stolz, R. M.; Mirica, K. A. Two-Dimensional Chemiresistive Covalent Organic Framework with High Intrinsic Conductivity. *Journal of the American Chemical Society* **2019**, *141*, 11929–11937.

(63) Medina, D. D.; Sick, T.; Bein, T. Photoactive and Conducting Covalent Organic Frameworks. *Advanced Energy Materials* **2017**, *7*, 1–8.

(64) Jhulki, S.; Evans, A. M.; Hao, X. L.; Cooper, M. W.; Feriante, C. H.; Leisen, J.; Li, H.; Lam, D.; Hersam, M. C.; Barlow, S.; Brédas, J. L.; Dichtel, W. R.; Marder, S. R. Humidity Sensing through Reversible Isomerization of a Covalent Organic Framework. *Journal of the American Chemical Society* **2020**, *142*, 783–791.

(65) Li, Z.; Feng, X.; Zou, Y.; Zhang, Y.; Xia, H.; Liu, X.; Mu, Y. A 2D azine-linked covalent organic framework for gas storage applications. *Chemical Communications* **2014**, *50*, 13825–13828.

(66) Wang, H. et al. Recent progress in covalent organic framework thin films: fabrications, applications and perspectives. *Chemical Society Reviews* **2019**, *48*, 488–516.

(67) Yuan, S.; Li, X.; Zhu, J.; Zhang, G.; Van Puyvelde, P.; Van Der Bruggen, B. Covalent organic frameworks for membrane separation. *Chemical Society Reviews* **2019**, *48*, 2665–2681.

(68) Dey, K.; Pal, M.; Rout, K. C.; Kunjattu, S. S.; Das, A.; Mukherjee, R.; Kharul, U. K.; Banerjee, R. Selective Molecular Separation by Interfacially Crystallized Covalent Organic

Framework Thin Films. *Journal of the American Chemical Society* **2017**, *139*, 13083–13091.

(69) Matsumoto, M.; Valentino, L.; Stiehl, G. M.; Balch, H. B.; Corcos, A. R.; Wang, F.; Ralph, D. C.; Mariñas, B. J.; Dichtel, W. R. Lewis-Acid-Catalyzed Interfacial Polymerization of Covalent Organic Framework Films. *Chem* **2018**, *4*, 308–317.

(70) Li, J.; Zhou, X.; Wang, J.; Li, X. Two-Dimensional Covalent Organic Frameworks (COFs) for Membrane Separation: A Mini Review. *Industrial and Engineering Chemistry Research* **2019**, *58*, 15394–15406.

(71) Corcos, A. R.; Levato, G. A.; Jiang, Z.; Evans, A. M.; Livingston, A. G.; Mariñas, B. J.; Dichtel, W. R. Reducing the Pore Size of Covalent Organic Frameworks in Thin-Film Composite Membranes Enhances Solute Rejection. *ACS Materials Letters* **2019**, *1*, 440–446.

(72) Gadwal, I.; Sheng, G.; Thankamony, R. L.; Liu, Y.; Li, H.; Lai, Z. Synthesis of Sub-10 nm Two-Dimensional Covalent Organic Thin Film with Sharp Molecular Sieving Nanofiltration. *ACS Applied Materials and Interfaces* **2018**, *10*, 12295–12299.

(73) Kuehl, V. A.; Yin, J.; Duong, P. H.; Mastorovich, B.; Newell, B.; Li-Oakey, K. D.; Parkinson, B. A.; Hoberg, J. O. A Highly Ordered Nanoporous, Two-Dimensional Covalent Organic Framework with Modifiable Pores, and Its Application in Water Purification and Ion Sieving. *Journal of the American Chemical Society* **2018**, *140*, 18200–18207.

(74) Shinde, D. B.; Cao, L.; Wonanke, A. D.; Li, X.; Kumar, S.; Liu, X.; Hedhili, M. N.; Emwas, A. H.; Addicoat, M.; Huang, K. W.; Lai, Z. Pore engineering of ultrathin covalent organic framework membranes for organic solvent nanofiltration and molecular sieving. *Chemical Science* **2020**, *11*, 5434–5440.

(75) Valentino, L.; Matsumoto, M.; Dichtel, W. R.; Marinas, B. J. Development and Performance Characterization of a Polyimine Covalent Organic Framework Thin-Film Composite Nanofiltration Membrane. *Environmental Science and Technology* **2017**, *51*, 14352–14359.

(76) Wang, R.; Shi, X.; Xiao, A.; Zhou, W.; Wang, Y. Interfacial polymerization of covalent organic frameworks (COFs) on polymeric substrates for molecular separations. *Journal of Membrane Science* **2018**, *566*, 197–204.

(77) Shinde, D. B.; Sheng, G.; Li, X.; Ostwal, M.; Emwas, A. H.; Huang, K. W.; Lai, Z. Crystalline 2D Covalent Organic Framework Membranes for High-Flux Organic Solvent Nanofiltration. *Journal of the American Chemical Society* **2018**, *140*, 14342–14349.

(78) Fan, H.; Gu, J.; Meng, H.; Knebel, A.; Caro, J. High-Flux Membranes Based on the Covalent Organic Framework COF-LZU1 for Selective Dye Separation by Nanofiltration. *Angewandte Chemie - International Edition* **2018**, *57*, 4083–4087.

(79) Dey, K.; Kunjattu H., S.; Chahande, A. M.; Banerjee, R. Nanoparticle Size-Fractionation through Self-Standing Porous Covalent Organic Framework Films. *Angewandte Chemie - International Edition* **2020**, *59*, 1161–1165.

(80) Kandambeth, S.; Biswal, B. P.; Chaudhari, H. D.; Rout, K. C.; Kunjattu H., S.; Mitra, S.; Karak, S.; Das, A.; Mukherjee, R.; Kharul, U. K.; Banerjee, R. Selective Molecular Sieving in Self-Standing Porous Covalent-Organic-Framework Membranes. *Advanced Materials* **2017**, *29*, 1–9.

(81) He, Y.; Lin, X.; Chen, J.; Guo, Z.; Zhan, H. Homogeneous Polymerization of Self-standing Covalent Organic Framework Films with High Performance in Molecular Separation. *ACS Applied Materials and Interfaces* **2020**, *12*, 41942–41949.

(82) Khan, N. A.; Zhang, R.; Wu, H.; Shen, J.; Yuan, J.; Fan, C.; Cao, L.; Olson, M. A.; Jiang, Z. Solid-Vapor Interface Engineered Covalent Organic Framework Membranes for Molecular Separation. *Journal of the American Chemical Society* **2020**, *142*, 13450–13458.

(83) Li, J.; Li, J.; Rong, H.; Chen, Y.; Zhang, H.; Liu, T. X.; Yuan, Y.; Zou, X.; Zhu, G. Screen printing directed synthesis of covalent organic framework membranes with water sieving property. *Chemical Communications* **2020**, *56*, 6519–6522.

(84) Zhang, W.; Zhang, L.; Zhao, H.; Li, B.; Ma, H. A two-dimensional cationic covalent organic framework membrane for selective molecular sieving. *Journal of Materials Chemistry A* **2018**, *6*, 13331–13339.

(85) Smith, B. J.; Overholts, A. C.; Hwang, N.; Dichtel, W. R. Insight into the crystallization of amorphous imine-linked polymer networks to 2D covalent organic frameworks. *Chemical Communications* **2016**, *52*, 3690–3693.

(86) Daugherty, M. C.; Vitaku, E.; Li, R. L.; Evans, A. M.; Chavez, A. D.; Dichtel, W. R. Improved synthesis of β-ketoenamine-linked covalent organic frameworks: Via monomer exchange reactions. *Chemical Communications* **2019**, *55*, 2680–2683.

(87) Vitaku, E.; Dichtel, W. R. Synthesis of 2D Imine-Linked Covalent Organic Frameworks through Formal Transimination Reactions. *Journal of the American Chemical Society* **2017**, *139*, 12911–12914.

(88) Ji, W.; Xiao, L.; Ling, Y.; Ching, C.; Matsumoto, M.; Bisbey, R. P.; Helbling, D. E.; Dichtel, W. R. Removal of GenX and Perfluorinated Alkyl Substances from Water by Amine-Functionalized Covalent Organic Frameworks. *Journal of the American Chemical Society* **2018**, *140*, 12677–12681.

(89) Karak, S.; Dey, K.; Torris, A.; Halder, A.; Bera, S.; Kanheerampockil, F.; Banerjee, R. Inducing Disorder in Order: Hierarchically Porous Covalent Organic Framework Nanostructures for Rapid Removal of Persistent Organic Pollutants. *Journal of the American Chemical Society* **2019**, *141*, 7572–7581.

(90) Robertson, M. J.; Tirado-Rives, J.; Jorgensen, W. L. Improved Peptide and Protein Torsional Energetics with the OPLS-AA Force Field. *Journal of Chemical Theory and Computation* **2015**, *11*, 3499–3509.

(91) Hess, B.; Kutzner, C.; Van Der Spoel, D.; Lindahl, E. GRGMACS 4: Algorithms for highly efficient, load-balanced, and scalable molecular simulation. *Journal of Chemical Theory and Computation* **2008**, *4*, 435–447.

(92) Dodda, L. S.; De Vaca, I. C.; Tirado-Rives, J.; Jorgensen, W. L. LigParGen web server: An automatic OPLS-AA parameter generator for organic ligands. *Nucleic Acids Research* **2017**, *45*, W331–W336.

(93) Vissers, T.; Wysocki, A.; Rex, M.; Löwen, H.; Royall, C. P.; Imhof, A.; Van Blaaderen, A. Lane formation in driven mixtures of oppositely charged colloids. *Soft Matter* **2011**, *7*, 2352–2356.

(94) Bacik, K. A.; Bacik, B. S.; Rogers, T. Lane nucleation in complex active flows. *Science* **2023**, *379*, 923–928.

(95) Bruna, M.; Burger, M.; de Wit, O. Lane formation and aggregation spots in a model of ants. **2024**, 1–35.

(96) Boyce, J. B.; Huberman, B. A. Superionic conductors: Transitions, structures, dynamics. *Physics Reports* **1979**, *51*, 189–265.

(97) Ehlen, A.; Lopez-Rios, H.; Olvera de la Cruz, M. Metallization of colloidal crystals. *Physical Review Materials* **2021**, *5*, 115601.

(98) Lin, Y.; Olvera de la Cruz, M. Superionic Colloidal Crystals: Ionic to Metallic Bonding Transitions. *Journal of Physical Chemistry B* **2022**, *126*, 6740–6749.

(99) Lopez-Rios, H.; Ehlen, A.; Olvera de la Cruz, M. Delocalization Transition in Colloidal Crystals. *Journal of Physical Chemistry C* **2021**, *125*, 1096–1106.

(100) Qian, D.; De La Cruz, M. O. Field-driven cluster formation in two-dimensional colloidal binary mixtures. *Physical Review E* **2023**, *107*, 1–10.

(101) Chen, K.; Still, T.; Schoenholz, S.; Aptowicz, K. B.; Schindler, M.; Maggs, A. C.; Liu, A. J.; Yodh, A. G. Phonons in two-dimensional soft colloidal crystals. *Physical Review E* **2013**, *88*, 022315.

(102) Loi, D.; Mossa, S.; Cugliandolo, L. F. Effective temperature of active matter. *Physical Review E* **2008**, *77*, 051111.

(103) Toner, J.; Tu, Y. Flocks, herds, and schools: A quantitative theory of flocking. *Physical Review E* **1998**, *58*, 4828–4858.

(104) Rubenstein, M.; Cornejo, A.; Nagpal, R. Programmable self-aseembly in a thousand-robot swarm. *Science* **2014**, *345*, 795–800.

(105) Baconnier, P.; Shohat, D.; López, C. H.; Coulais, C.; Démery, V.; Düring, G.; Dauchot, O. Selective and collective actuation in active solids. *Nature Physics* **2022**, *18*, 1234.

(106) Ferrante, E.; Turgut, A. E.; Dorigo, M.; Huepe, C. Elasticity-based mechanism for the collective motion of self-propelled particles with springlike interactions: A model system for natural and artificial swarms. *Physical Review Letters* **2013**, *111*, 268302.

(107) Leunissen, M. E.; Christova, C. G.; Hynninen, A. P.; Royall, C. P.; Campbell, A. I.; Imhof, A.; Dijkstra, M.; Van Roij, R.; Van Blaaderen, A. Ionic colloidal crystals of oppositely charged particles. *Nature* **2005**, *437*, 235–240.

(108) Girard, M.; Wang, S.; Du, J. S.; Das, A.; Huang, Z.; Dravid, V. P.; Lee, B.; Mirkin, C. A.; Olvera de la Cruz, M. Particle analogs of electrons in colloidal crystals. *Science* **2019**, *364*, 1174–1178.

(109) Lin, Y.; Olvera de la Cruz, M. Sublattice melting in binary superionic colloidal crystals. *Physical Review E* **2020**, *101*, 032603.

(110) Padilla, L. A.; León-Islas, A. A.; Funkhouser, J.; Armas-Pérez, J. C.; Ramírez-Hernández, A. Dynamics and phase behavior of two-dimensional size-asymmetric binary mixtures of core-softened colloids. *Journal of Chemical Physics* **2021**, *155*, 214901.

(111) Thorneywork, A. L.; Abbott, J. L.; Aarts, D.; Dullens, R. Two-Dimensional Melting of Colloidal Hard Spheres. *Physical Review Letters* **2017**, *118*, 158001.

(112) Keim, P.; Maret, G.; Herz, U. Harmonic Lattice Behavior of Two-Dimensional Colloidal Crystals. *Physical Review Letters* **2004**, *92*, 215504.

(113) Bernard, E. P.; Krauth, W. Two-Step Melting in Two Dimensions : First-Order Liquid-Hexatic Transition. *Physical Review Letters* **2011**, *107*, 155704.

(114) Bian, T.; Gardin, A.; Gemen, J.; Houben, L.; Perego, C.; Lee, B.; Elad, N.; Chu, Z.; Pavan, G. M.; Klajn, R. Electrostatic co-assembly of nanoparticles with oppositely charged small molecules into static and dynamic superstructures. *Nature Chemistry* **2021**, *13*, 940–949.

(115) Zöttl, A.; Stark, H. Hydrodynamics determines collective motion and phase behavior of active colloids in quasi-two-dimensional confinement. *Physical Review Letters* **2014**, *112*, 118101.

(116) Glanz, T.; Löwen, H. The nature of the laning transition in two dimensions. *Journal of Physics Condensed Matter* **2012**, *24*, 464114.

(117) Qu, N.; Luo, Z.; Zhao, S.; Liu, B. Frame-Guided Synthesis of Polymeric Colloidal Discs. *Journal of the American Chemical Society* **2021**, *143*, 1790–1797.

(118) Iwaki, M.; Wickham, S. F.; Ikezaki, K.; Yanagida, T.; Shih, W. M. A programmable DNA origami nanospring that reveals force-induced adjacent binding of myosin VI heads. *Nature Communications* **2016**, *7*, 13715.

(119) Hu, X.; Park, J.-e.; Kang, S.; Kim, C.-j.; Park, S.-j.; Kim, Y. Free-standing two-dimensional sheets of polymer-linked nanoparticles. *Nanoscale* **2022**, *14*, 12849–12855.

(120) Zhu, W. H.; Pashrashid, A.; Adel, W.; Gunerhan, H.; Nisar, K. S.; Ahamed Saleel, C.; Inc, M.; Rezazadeh, H. Dynamical behaviour of the foam drainage equation. *Results in Physics* **2021**, *30*, 104844.

(121) Koehler, S. A.; Hilgenfeldt, S.; Stone, H. A. A Generalized view of foam drainage: Experiment and theory. *Langmuir* **2000**, *16*, 6327–6341.

(122) Thompson, A. P.; Aktulga, H. M.; Berger, R.; Bolintineanu, D. S.; Brown, W. M.; Crozier, P. S.; in 't Veld, P. J.; Kohlmeyer, A.; Moore, S. G.; Nguyen, T. D.; Shan, R.; Stevens, M. J.; Tranchida, J.; Trott, C.; Plimpton, S. J. LAMMPS - a flexible simulation tool for particle-based materials modeling at the atomic, meso, and continuum scales. *Computer Physics Communications* **2022**, *271*.

(123) Jones, H. M.; Kunhardt, E. E. The influence of pressure and conductivity on the pulsed breakdown of water. *IEEE Transactions on Dielectrics and Electrical Insulation* **1994**, *1*, 1016–1025.

(124) Stukowski, A. Visualization and analysis of atomistic simulation data with OVITO-the Open Visualization Tool. *Modelling and Simulation in Materials Science and Engineering* **2010**, *18*.

(125) Bagchi, D. Macroscopic charge segregation in driven polyelectrolyte solutions. *Soft Matter* **2022**, *18*, 5676–5686.

(126) Sütterlin, K. R.; Wysocki, A.; Ivlev, A. V.; Räth, C.; Thomas, H. M.; Rubin-Zuzic, M.; Goedheer, W. J.; Fortov, V. E.; Lipaev, A. M.; Molotkov, V. I.; Petrov, O. F.; Morfill, G. E.; Löwen, H. Dynamics of lane formation in driven binary complex plasmas. *Physical Review Letters* **2009**, *102*, 085003.

(127) Dzubiella, J.; Hoffmann, G. P.; Löwen, H. Lane formation in colloidal mixtures driven by an external field. *Physical Review E* **2002**, *65*, 021402.

(128) Rex, M.; Löwen, H. Lane formation in oppositely charged colloids driven by an electric field: Chaining and two-dimensional crystallization. *Physical Review E - Statistical, Nonlinear, and Soft Matter Physics* **2007**, *75*, 051402.

(129) Reichhardt, C.; Thibault, J.; Papanikolaou, S.; Reichhardt, C. Laning and clustering transitions in driven binary active matter systems. *Physical Review E* **2018**, *98*, 022603.

(130) Li, B.; Wang, Y. L.; Shi, G.; Gao, Y.; Shi, X.; Woodward, C. E.; Forsman, J. Phase Transitions of Oppositely Charged Colloidal Particles Driven by Alternating Current Electric Field. *ACS Nano* **2021**, *15*, 2363–2373.

(131) Klymko, K.; Geissler, P. L.; Whitelam, S. Microscopic origin and macroscopic implications of lane formation in mixtures of oppositely driven particles. *Physical Review E* **2016**, *94*, 022608.

(132) Wächtler, C. W.; Kogler, F.; Klapp, S. Lane formation in a driven attractive fluid. *Physical Review E* **2016**, *94*, 052603.

(133) Chetverikov, A. P.; Ebeling, W.; Velarde, M. G. Dissipative solitons and complex currents in active lattices. *International Journal of Bifurcation and Chaos* **2006**, *16*, 1613–1632.

(134) Malomed, B. A.; G.Winful, H. Stable solitons in two-component active systems. *Physical Review E* **1996**, *53*, 5365–5368.

(135) Chetverikov, A. P.; Ebeling, W.; Velarde, M. G. Soliton-like excitations and solectrons in two-dimensional nonlinear lattices. *European Physical Journal B* **2011**, *80*, 137–145.

(136) Buttinoni, I.; Bialké, J.; Kümmel, F.; Löwen, H.; Bechinger, C.; Speck, T. Dynamical clustering and phase separation in suspensions of self-propelled colloidal particles. *Physical Review Letters* **2013**, *110*, 238301.

(137) Zaccone, A.; Wu, H.; Gentili, D.; Morbidelli, M. Theory of activated-rate processes under shear with application to shear-induced aggregation of colloids. *Physical Review E* **2009**, *80*, 051404.

(138) Kanehl, P.; Stark, H. Self-Organized Velocity Pulses of Dense Colloidal Suspensions in Microchannel Flow. *Physical Review Letters* **2017**, *119*, 018002.

(139) Zaccone, A.; Gentili, D.; Wu, H.; Morbidelli, M.; Del Gado, E. Shear-driven solidification of dilute colloidal suspensions. *Physical Review Letters* **2011**, *106*, 138301.

(140) Velarde, M. G.; Ebeling, W.; Chetverikov, A. P. On the possibility of electric conduction mediated by dissipative solitons. *International Journal of Bifurcation and Chaos in Applied Sciences and Engineering* **2005**, *15*, 245–251.

(141) Lavrentovich, M. O.; Dickman, R.; Zia, R. K. Microemulsions in the driven Widom-Rowlinson lattice gas. *Physical Review E* **2021**, *104*, 1–16.

(142) Dickman, R.; Zia, R. K. Driven Widom-Rowlinson lattice gas. *Physical Review E* **2018**, *97*, 1–14.

(143) Yuan, J.; Takae, K.; Tanaka, H. Impact of Inverse Squeezing Flow on the Self-Assembly of Oppositely Charged Colloidal Particles under Electric Field. *Physical Review Letters* **2022**, *129*, 248001.

(144) Evans, C. G.; O'Brien, J.; Winfree, E.; Murugan, A. Pattern recognition in the nucleation kinetics of non-equilibrium self-assembly. *Nature* **2024**, *625*, 500–507.

(145) A smart and responsive crystalline porous organic cage membrane with switchable pore apertures for graded molecular sieving. *Nature Materials* **2022**, *21*, 463–470.

(146) Cao, L.; Liu, X.; Shinde, D. B.; Chen, C.; Chen, I.-C.; Li, Z.; Zhou, Z.; Yang, Z.; Han, Y.; Lai, Z. Oriented Two-Dimensional Covalent Organic Framework Membranes with High Ion Flux and Smart Gating Nanofluidic Transport. *Angewandte Chemie* **2022**, *134*.

(147) Jrad, A.; Olson, M. A.; Trabolsi, A. Molecular design of covalent organic frameworks for seawater desalination: A state-of-the-art review. *Chem* **2023**, *9*, 1413–1451.

(148) Ma, X.; Chen, W.; Wang, Z.; Peng, Y.; Han, Y.; Tong, P. Test of the universal scaling law of diffusion in colloidal monolayers. *Physical Review Letters* **2013**, *110*, 2–6.

(149) Onsager, L. REPORT ON A REVISION OF THE CONDUCTIVITY THEORY. *Faraday Soc.* **1927**, *23*, 341–349.

(150) Li, H.; Erbaş, A.; Zwanikken, J.; Olvera De La Cruz, M. Ionic Conductivity in Polyelectrolyte Hydrogels. *Macromolecules* **2016**, *49*, 9239–9246.

(151) Manning, G. S. A limiting law for the conductance of the rod model of a salt-free polyelectrolyte solution. *Journal of Physical Chemistry* **1975**, *79*, 262–265.

(152) Bonaccurso, E.; Schönfeld, F.; Butt, H. J. Electrostatic forces acting on tip and cantilever in atomic force microscopy. *Physical Review B - Condensed Matter and Materials Physics* **2006**, *74*, 1–8.

(153) Chen, J.; Brooks, C. L.; Scheraga, H. A. Revisiting the Carboxylic Acid Dimers in Aqueous Solution : Interplay of Hydrogen Bonding, Hydrophobic Interactions, and Entropy. *Journal of Physical Chemistry B* **2008**, *112*, 242–249.

(154) Use of approximate integrals in ab initio theory. An application in MP2 energy calculations. *Chemical Physics Letters* **1993**, *208*, 359–363.

(155) Shao, Y.; et al. Advances in molecular quantum chemistry contained in the Q-Chem 4 program package. *Molecular Physics* **2015**, *113*, 184–215.

(156) Abraham, M. J.; Murtola, T.; Schulz, R.; Páll, S.; Smith, J. C.; Hess, B.; Lindah, E. Gromacs: High performance molecular simulations through multi-level parallelism from laptops to supercomputers. *SoftwareX* **2015**, *1-2*, 19–25.

(157) Development and testing of the OPLS all-atom force field on conformational energetics and properties of organic liquids. *Journal of the American Chemical Society* **1996**, *118*, 11225–11236.

(158) Danilov, D.; Barner-Kowollik, C.; Wenzel, W. Modelling of reversible single chain polymer self-assembly: From the polymer towards the protein limit. *Chemical Communications* **2015**, *51*, 6002–6005.

APPENDIX A

SUPPLEMENTARY INFORMATION FOR CHAPTER 2

This appendix contains the supplementary information associated with Chapter 2. The following was submitted to JACS in 2024.

Supplementary Information: Hydrogen-Bonded Fibers Assembled from Trigonal Prismatic Building Blocks

Authors: Sayantan Mahapatra[#], Dingwen Qian[#], Ruihua Zhang, Shuliang Yang, Penghao Li, Yuanning Feng, Long Zhang, Huang Wu, James S. W. Seale, Partha Jyoti Das, Prateek K. Jha, Kevin Lee Kohlstedt, M. Olvera de la Cruz, and J. Fraser Stoddart

A.1 Materials / General Information

The peripherally extended triptycene (H_6PET) was synthesized following a published protocol [25]. Addition of H_6PET in acetone ($\sim$1mM) leads to a turbid solution (**Figures A.1a–b**) from which a few mL of solution was extracted and centrifuged for one minute. This procedure facilitates the settling of structures at the bottom of the vial. Subsequently, we dropcasted selectively the white-colored solution onto a cover slip for optical imaging which shows (**Figures A.1c–d**) the presence of numerous fibers with noticeable optical contrast. The fibers are exhibited predominantly a unidirectional nature with the width ranges from 1.4 to 2.0 μm. From the optical contrast, we can suggest the tubular nature of the fibrous structures. Furthermore, confocal Raman spectroscopic analysis (LabRAM HR Evolution) was employed for the chemical identification of the fibrous structures. By focusing a red laser ($\lambda_{ex} = 633$ nm) onto a fiber structure (**Figure A.1d**), we detected the carbon-carbon double bond stretching frequency (only one detectable peak, red spectrum in **Figure A.1e**) at $\sim$1609 cm^{-1} ($t_{acq} = 10$ sec, $P_{acq} = 3.34$ mW). The peak shows consistent characteristics across various sections of the same fiber, affirming its structural and morphological homogeneity. Moreover, the focused laser exposure of 10 seconds ($P_{acq} = 3.34$ mW) does not affect the fiber structures (not visible by optical microscope), providing evidence of hydrogen-bonded fiber structure's stability under laser illumination. For comparison, the powder Raman

spectrum of H_6PET was acquired (pink spectrum in **Figure A.1e**, $\lambda_{ex} = 633$ nm, $t_{acq} = 10$ sec, $P_{acq} = 3.34$ mW), confirming the $\sim$1609 cm^{-1} peak.

For a detailed analysis of the fiber growth mechanism and trajectory at the early stage, sample concentrations of 10 μM (H_6PET in acetone) were utilized for different experimental investigations (such as AFM, TEM, and SEM). Following the preparation of a fresh solution (clear solution), 2–6 μL solution was very quickly (typically within 30 sec) extracted and dropcasted on the sample for further experimental analysis i.e., 6 μL solution for AFM, and 2 μL solution for TEM experiments. This sample was designated as 0 hours (dropcasted within 30 sec). For the analysis of 3-hour, 6-hour, 12-hour, and 24-hour solutions, we extracted 2–6 μL solution from the clear part of the solution. The large-scale microfibers are already visible to the naked eye at this stage. One such example of a 6-hour solution is shown in Figure A.1f.

A.2 UV-Visible Spectroscopy

Approximately 10 μM of solution (H_6PET in acetone) was employed for UV-Vis spectroscopy in a capped quartz cuvette at different time intervals (i.e., $0 \rightarrow 3 \rightarrow 6 \rightarrow 9 \rightarrow 12 \rightarrow 24$ hours) at 298 K. UV-Vis absorption spectra were recorded on a UV-3600 Plus SHIMADZU spectrophotometer at Northwestern University. No detectable solvent loss was observed in this time range. We employed a scan range of 200–700 nm with a data interval of 1.0 nm. **Figure A.2a** illustrates the spectrum of pure acetone, revealing significant noise levels below 330 nm. The signal, however, remains flat (**Figure A.2b**) in the range between 330–400 nm. Hence, we only focus on the 330–400 nm region to detect any variations resulting from the formation of the fibers at different time intervals. **Figure A.2c** illustrates the variation in absorbance over different time intervals primarily because of light scattering. The spectra obtained at different times were averaged from three separate trials. For ease of interpretation, the transmittance (%T) values were plotted over time specifically at $\lambda = 333$

nm (**Figure 2.1g** in main text). The transmittance (%T) values are calculated using the following equation:

$$\%T = antilog(2–Absorbance) \tag{A.1}$$

The transmittance (%T) value changes as follows: 94.3% (0-hours) → 63.0% (3-hours) → 48.3% (6-hours) → 46.5% (9-hours) → 45.8% (12-hours) → 43.8% (24 hours). In addition, the refractive index (RI) of the solution at different time intervals was plotted in **Figure A.2d**. The RI values were calculated using the following equation:

$$RI = \frac{1}{T} + \sqrt{\frac{1}{T-1}} \tag{A.2}$$

where T is the percent transmittance.

A.3 Atomic Force Microscopy (AFM)

For AFM characterization, approximately 6 µL of freshly prepared (i.e., 0 hours) solution (10 µM, H_6PET in acetone) was dropcasted quickly on freshly cleaved highly oriented pyrolytic graphite (HOPG) surface (ZYB grade from µmasch). After dropcasting, the sample was dried thoroughly in the air (∼6 hours) and imaged under ambient conditions. The HOPG substrate was tilted $\sim 40^{\circ}$ during drop-casting to ensure a smooth flow of the solution. AFM Imaging was performed with a dried sample on a Dimension ICON, Bruker Corporation using tapping mode at Northwestern University's SPID/NUANCE facility. The height and phase profile of individual one-dimensional nanotubes and higher-order structures were analyzed utilizing built-in software. The height profile provides the approximate outer diameter of the nanotubes, which was found to be ∼4.75 ± 0.2 nm. On the other hand, a dip in the AFM phase image indicates a change in the properties of the

structure (i.e., a change in the tip-sample interactions) which can be attributed to the presence of the hollow tube i.e., air is present. If the tube is solid, the AFM phase profile would follow the AFM height profile [27].

Mathematical Interpretation of AFM Phase Image:

In tapping-mode atomic force microscopy (TM-AFM), the cantilever is stimulated to oscillate near its resonant frequency. The AFM tip makes intermittent contact with the sample surface. In contrast to contact-mode AFM, tapping-mode AFM minimizes tip-sample interaction times, thereby reducing lateral forces. Variations in the effective vertical forces acting on the tip modify the oscillation in both amplitude and phase [152]. Concurrently capturing the topography and phase shift of the cantilever oscillation relative to the driving signal enables the mapping of interaction properties across a heterogeneous sample. This phase imaging technique is valuable for exploring diverse material properties. As demonstrated recently [28], the phase shift directly correlates with the energy dissipated in the tip-sample contact. The true interpretation of phase images remains extremely difficult and ambiguous. The dissipation-contributing channels, influenced significantly by sample topography, are not easily accessible. Here, we explore the formation of contrast in phase imaging, focusing on the structure and interaction of a macromolecular system. The discussion on contrast formation in phase imaging centers around the influence of interaction and topography. The phase shift, amplitude, and the energy dissipated in the tip-sample contact can be equated as [29]:

$$PE_d = AA_0 sin\phi - A^2 \tag{A.3}$$

where A and A_0 are actual and free amplitude respectively. ϕ is the phase shift. E_d is the dissipated energy in the tip-sample contact. P contains the information about the cantilever (including its environments) and can be written in terms of its spring constant (K_{cant}), natural resonant frequency (ω_{cant}), and quality factor (Q_{cant}). Each quantity can be written into its average value and its local

variation.

$$E_d = E_d^0 + \delta E \tag{A.4}$$

$$A = A_0(a_0 + \delta a) \tag{A.5}$$

$$\phi = \Pi/2 + \phi_0 + \delta\phi \tag{A.6}$$

The phase shift is determined relative to the free oscillation (90°). Therefore, ϕ_0 represents the average deviation from $90°$, while $\delta\phi$ indicates variations around that average value. A phase shift $\delta\phi > 0$ is referred to as delayed, and $\delta\phi$ ¡ 0 is referred to as advanced. The amplitude (A) is written in terms of free amplitude (A_0). For clarification, coordinates (x, y) are omitted. Therefore, Eq. A.3 becomes:

$$P(E_d^0 + \delta E) = A_0^2(a_0 + \delta a)cos(\phi_0 + \delta\phi) - [A_0(a_0 + \delta a)]^2 \tag{A.7}$$

$$\frac{P(E_d^0 + \delta E)}{A_0^2} = (a_0 + \delta a)cos(\phi_0 + \delta\phi) - [(a_0 + \delta a)]^2 \tag{A.8}$$

Consider the small angle approximation, $sin(\delta\phi) = \delta\phi$ and $cos(\delta\phi) = 1$ and neglect the $(\delta a)^2$,

$$\frac{P(E_d^0 + \delta E)}{A_0^2} = (a_0 cos\phi_0 + a_0^2) + [cos\phi_0(\delta a) - 2a_0(\delta a) - a_0 sin\phi_0(\delta\phi)] \tag{A.9}$$

This equation can be divided into two parts, one containing the averages and other containing the variations:

$$P(E_d^0) = A_0^2(a_0 cos\phi_0 + a_0^2) \tag{A.10}$$

$$P(\delta E) = A_0^2[cos\phi_0(\delta a) - 2a_0(\delta a) - a_0 sin\phi_0(\delta\phi)] \tag{A.11}$$

Eq. A. 11 indicates the dependence of phase image ($\delta\phi$) with the variation in the dissipative

energy (δE) [where (δa) is the error image]. Thus, the phase shift of the tip oscillation establishes a connection between the dynamic behavior of the cantilever and the tip-sample interaction. In each tapping cycle under ambient conditions, the tip may experience various tip-sample force regimes, encompassing attractive forces like van der Waals and capillary forces, as well as the repulsive indentation force. This information can be employed to trace the sample topography and understand its interaction with the tip. Importantly, the tip-sample interactions are associated with the material, charge, and conformation (molecular geometry) of the sample. In the case of the hydrogen-bonded organic nanotube, the phase line profile shows the phase shift on the side walls is on average delayed by $+2.75 \pm 0.25^{\circ}$ (relative to the HOPG surface). Whereas the center part of the tube (in between the side walls) is advanced by -1°. This observation confirms that the tip-sample interactions are very similar on both the side walls. In the central part, however, it is completely different. This behavior is understandable as we investigate the nanotube model where molecular conformation is expected to be distinct in the central region compared to both the sidewalls (where molecular conformation is similar), leading to differences in tip-sample interactions (Figure A.3).

A.4 Transmission Electron Microscopy (TEM)

High-magnification TEM characterizations were performed on JEOL ARM200CF at Northwestern University's EPIC/NUANCE facility. Approximately 2 μL of freshly prepared (i.e., 0 hours) solution (10 μM, H_6PET in acetone) was dropcasted on the ultrathin carbon TEM grid. After drying, the sample was characterized directly under different magnifications. TEM Images were acquired using a JEOL ARM200CF microscope operated at 200 kV. Figure A.4 illustrates additional TEM images of hydrogen-bonded organic nanotubes (HONTs) with a hollow nature. Occasionally, the HONTs may experience partial damage due to exposure to high-energy electron density (200 kV) during TEM imaging (Figure A.4e). It is also worth mentioning that, in addition to the nanotubes,

a few higher-order structures (width ranging from ∼20–60 nm) are also observable when examining the freshly prepared solution (i.e., 0 hours) under TEM analysis (Figures A.4d and A.4f). The one-dimensional nanotubes grow spontaneously (transverse growth) in all directions to generate such extended structures. The high-order structures exhibit predominantly a unidirectional nature (up to several micrometers in length), aligning well with the pattern observed in the one-directional nanotube structures. This observation strongly suggests that the higher-order structures originate from the nanotubes.

A.5 N_2 Adsorption Isotherm

The N_2 adsorption isotherms of hydrogen-bonded large-scale microfibers were measured at 77K. Isolating individual HONTs proved impossible because of their spontaneous transformation into large-scale microfibers. H_6PET (8.3 mg) was mixed with acetone (5 mL), resulting in a turbid solution. The turbid solution was passed through a 45-mm syringe filter. The resulting clear solution was placed in a 20 mL glass vial. The vial was loosely capped to facilitate the slow evaporation of the solvent. After 6 days, the vial was completely dry, and fibrous structures were observed (Figure A.5a) sticking to the side glass walls. In addition to the fibers, some amorphous white solid materials were also detected (Figure A.5a) at the bottom of the vial. We extracted everything i.e., fibrous structures and amorphous materials from the glass vial using a spatula. Activation of the samples was performed under a dynamic vacuum for 1 h at 25 °C and 14 h at 90 °C on the Micromeritics ASAP 2020 instrument at Northwestern University. Around 30–32 mg sample was used in the experiment. The Brunauer-Emmett-Teller (BET) surface area was calculated within the range of 0.01 to 0.1 P_0/P. This range was chosen to minimize errors and ensure consistency ($R^2 > 0.999$) in the surface area analysis. The pore size distribution (Figure A.5b) using a carbon cylinder-pore model (at 77 K) method indicated consistently two types of

pores i.e., 22–30 Å and 35–41 Å aligning well with the theoretically predicted one-dimensional nanotube model (Figure A.5c). The pore distribution, ranging from 35 to 41 Å, corresponds to the primary hollow tubular channel extending along the length of the nanotube (Figures A.5c and A.5b). Conversely, the pore distribution of 22–30 Å coincides (Figures A.5d and A.5c) with the side pores situated on the walls of the nanotube.

A.6 Phenomenological Model of H_6PET Assembly at Early Stage

A.6.1 Dimerization Free Energy Calculation and the Solvent Effect

Since benzoic acidic groups are the terminal groups of the arms, we calculate the free energy of dimerization of benzoic acids for measurement of the double hydrogen bond strength. The free energy of dimerization in the solvent is calculated [153] by the following formula:

$$\Delta G_d^{sol} = \Delta G_d^{gas} + \Delta\Delta G_{solv} + RTln(\frac{1}{22.4}) \tag{A.12}$$

The free energy of dimerization in gas ΔG_d^{gas} is calculated by the RI-MP2 method [154] using the Q-Chem package [155]. The basis is the correlation-consistent Dunning's cc-pvtz, and the aux-basis is rimp2-cc-pvtz. The gas-phase free energy is calculated using the ideal gas equation of state. The free energy of dimerization is composed of enthalpic and entropic terms: $\Delta G_d^{gas} = \Delta H_d^{gas} - T\Delta S_d^{gas}$. The entropy change of rotation during dimerization is ΔS_d^{rot}. The solvation energy is calculated from all-atom molecular dynamics simulations in NPT ensembles using GROMACS package [156]. We calculated the solvation energy difference in acetone and diethyl ether for comparison. The OPLS forcefield is used in the all-atom simulations [157]. The last term in the free energy of dimerization in the solvent is a correction term converting from the standard state in gas phase to the standard state in the solution phase. The free energy components mentioned

above are listed in Table A.1.

ΔH_d^{gas}	ΔS_d^{gas}	ΔS_d^{rot}	ΔG_d^{gas}	ΔG_{ace}^{m}	$\Delta\Delta G_{ace}$	ΔG_d^{ace}	ΔG_{eth}^{d}	ΔG_{eth}^{m}	$\Delta\Delta G_{eth}$	ΔG_d^{eth}
–16.9	–38.3	–25.1	–5.5	–11.3	2.4	–4.9	–19.8	–10.3	0.8	–6.5

Table A.1: Components of the dimerization free energy of benzoic acids in acetone and ether. All enthalpic and free energy terms are in the unit of kcal/mol. The entropic terms are in the unit of cal/(mol·K).

Acetone is a more polar solvent in comparison with diethyl ether. The free energy of dimerization of benzoic acid in acetone is higher than in ether by 1.6 kcal/mol. This result is consistent with the expectation that hydrogen bonds are weaker in more polar solvents [153].

The entropy change during the dimerization is used as the estimation of the entropy loss due to the restriction of rigid body motions. The concentration of monomers in the experiments is $10^{-3}\ M$. Therefore, the constant term in Eq. (2.9) (in the main text) is $10^{-3}\exp\left[\frac{\Delta S_d^{sol}}{k}\right] = (10^{-3}\exp\left[\frac{\Delta S_d^{gas}}{k} + \ln 22.4\right] = \exp[-23]$.

The diffusion coefficient of H_6PET molecules in acetone is calculated using Stokes formula: $D = \frac{kT}{6\pi\eta R} = 6.9 \times 10^{-10}\ m^2/s$, where the radius R is estimated to be 1 nm and the dynamic viscosity η is $0.316\ mPa \cdot s$ for acetone at room temperature. The average diffusion time scale is $\tau_D = \frac{\overline{r}^2}{D} = 24\ ns$, where $\overline{r} = 10\ nm$ is the average distance between monomers based on the concentration $10^{-3}M$. The average time required for a monomer to locate an attachable site is estimated by $\tau = \tau_D \exp\left[-\frac{\Delta S_d^{rot}}{k}\right] = 7\ ms$, where $\exp\left[-\frac{\Delta S_d^{rot}}{k}\right]$ is the fraction of collisions with right orientation.

A.6.2 Shape Anisotropies and Snapshots of H_6PET Assemblies

The gyration tensor of a PET assembly characterizes its density distribution in space:

$$S_{mn} = \frac{1}{2N_V^2} \sum_{i=1}^{N_V} \sum_{j=1}^{N_V} \left(r_m^{(i)} - r_m^{(j)}\right) \left(r_n^{(i)} - r_n^{(j)}\right) \tag{A.13}$$

where m and n are indices for directions, i and j are indices for the monomers. We can always find a coordination system where the gyration tensor is diagonalized:

$$\tilde{S} = \begin{bmatrix} \lambda_a^2 & 0 & 0 \\ 0 & \lambda_b^2 & 0 \\ 0 & 0 & \lambda_c^2 \end{bmatrix} \tag{A.14}$$

The shape anisotropy [158] is defined as $\kappa^2 = \frac{3}{2} \frac{\lambda_a^4 + \lambda_b^4 + \lambda_c^4}{\left(\lambda_a^2 + \lambda_b^2 + \lambda_c^2\right)^2} - \frac{1}{2}$. When $\lambda_a = \lambda_b = 0$ and $\lambda_c \neq 0$, the assembly is a straight line in one direction and $\kappa^2 = 1$. When $\lambda_a = \lambda_b = \lambda_c$, the assembly extends evenly in all directions and $\kappa^2 = 0$. Here we define the tubular structure as $\kappa^2 > 0.2$. The shape anisotropy of the assembly as the function of hydrogen bond strength $|\Delta H_d^\circ|$ at different value of $|\Delta S_a^\circ|$ is shown in **Figure A.7c**.

A.6.3 Free energy of fragments and free energy landscape of growth paths at different regimes

In classical nucleation theory, the free energy of cluster formation for n-cluster is defined [36, 38] as $\Delta G\left(n\right) = -kTln[\frac{\rho^{eq}(n)}{\rho^{eq}(1)}]$. The $\rho^{eq}\left(n\right)$ is the concentration of the n-cluster assuming that the n-cluster is in chemical equilibrium with the reservoir of monomers with concentration $\rho^{eq}\left(1\right)$ .The cluster is fully characterized by its size n because of the capillary approximation. The capillary

approximation hypothesizes that a cluster is a large homogeneous spherical droplet of a well-defined radius with the bulk liquid properties inside it and the bulk vapor density outside it. In the system with clusters of complex structure, the free energy of the cluster depends on the geometry of the clusters. In our system, the geometric information is encoded in the graph representation of the fragments. Therefore, it is natural to define the free energy of the fragment as $\Delta G\left(g_{N_V,N_E}\right) = -kTln\left[\frac{\rho^{eq}\left(g_{N_V,N_E}\right)}{\rho^{eq}(m)}\right] = \Delta G^{\circ}\left(g_{N_V,N_E}\right) - \left(N_V - 1\right)kTln[m_0]$, where the second equal relation follows from the law of mass action. Similar approach has been seen in the work of Jacobs *et al.* [3], with the difference that they work with lattice models. Cai *et al.* [36] derived a formula with similar format for classical nucleation theory.

In the main text we showed the free energy landscapes of different pathways at the regime of forming tubular structures. Here we show the free energy landscapes at the regime of no assembly and forming a three-dimensional structure in **Figure A.10**.

A.6.4 Experimental Control for Proposed Theoretical Model

In order to validate our theoretical model, we designed two more PET monomers (H_6PET-1 and H_6PET-2, **Figure A.11**) of varying arm lengths and prepared $\sim$1mM solution in acetone. We observed no hydrogen-bonded fiber formation process for both the PET monomers in acetone. In keeping with the previous experiments, $\sim$10 μM solutions were prepared (for both the monomers) and $\sim$6 μL solutions were dropcasted (within 30 seconds) on HOPG surface for AFM investigations. This procedure offers a direct comparison with the results obtained from the H_6PET case. As shown in **Figures A.11b** and **A.11d**, no nanotube structures were visualized. Since the arm lengths of H_6PET-1 and H_6PET-2 are longer compared to H_6PET, we anticipate the tubular phase does not manifest itself in these cases, most likely due to structural instabilities. As such, we find that H_6PET-1 and H_6PET-2 do not form hydrogen-bonded fibrous structures under the same

conditions that lead to fiber formation in structurally analogous H_6PET.

A.7 Field Emission Scanning Electron Microscope (FESEM)

Field Emission Scanning Electron Microscopy (FESEM) characterization was performed on Hitachi S-4800 instrumebt at Northwestern University's EPIC/NUANCE facility. The sample (at different hours such as 3, 6, 12, and 24-hours) was dropcasted on the silicon plate. After drying, a $\sim$9 nm thick layer of OsO4 was coated on the sample surface using a Denton Desk III TSC Sputter Coater to increase the conductivity. In order to gain a better understanding of the nanofibers' existence and distribution, samples of 3, 6, 12, and 24 hours were imaged by SEM over multiple regions (at least five) several hundred micrometers apart.

A.8 More Details about Higher-Order Structures

A.8.1 Thermodynamics of H_6PET Assembly

The formation of hydrogen-bonded unidirectional nanotubes (at the early stage) is the result of anisotropy in growth kinetics. The nanotubes exhibit extremely high aspect ratio ($\lambda = \frac{L}{d}$) and are characterized by a high surface-area-to-volume ratio. Below we demonstrate that the thermodynamically stable product has a small aspect ratio, i.e., be a three-dimensional structure. The three-dimensional structure is more stable because the number of hydrogen bonds per monomer in the assembly of low aspect ratio is significantly higher compared to that in the nanotube, resulting in a minimal surface area that lowers the free energy. We can build a Flory-Huggins theory of the free energy of the self-assembly:[15]

$$F = \sum_{L_x,L_y,L_z} c\left(L_x, L_y, L_z\right)\left[lnc\left(L_x, L_y, L_z\right) + \varepsilon_z L_x L_y + \varepsilon_x (L_y L_z + L_x L_z)\right] \tag{A.15}$$

under the constraint $\sum_{L_x,L_y,L_z} c\left(L_x, L_y, L_z\right) L_x L_y L_z = \phi$. The $c\left(L_x, L_y, L_z\right)$ is the concentration of the assembly with dimensions (L_x, L_y, L_z) in different directions. ε_z and ε_x are the scission energy density in x and z directions. After minimizing the free energy with the constraint, we get $\frac{\overline{L_x}}{\overline{L_z}} = \frac{\varepsilon_x}{\varepsilon_z}$. The average length scale depends linearly on the scission energy density and the aspect ratio should be small. Hence, the theoretical model suggests that the nanotube tends to grow thicker at long experimental time which eventually leads to large-scale microfiber structures.

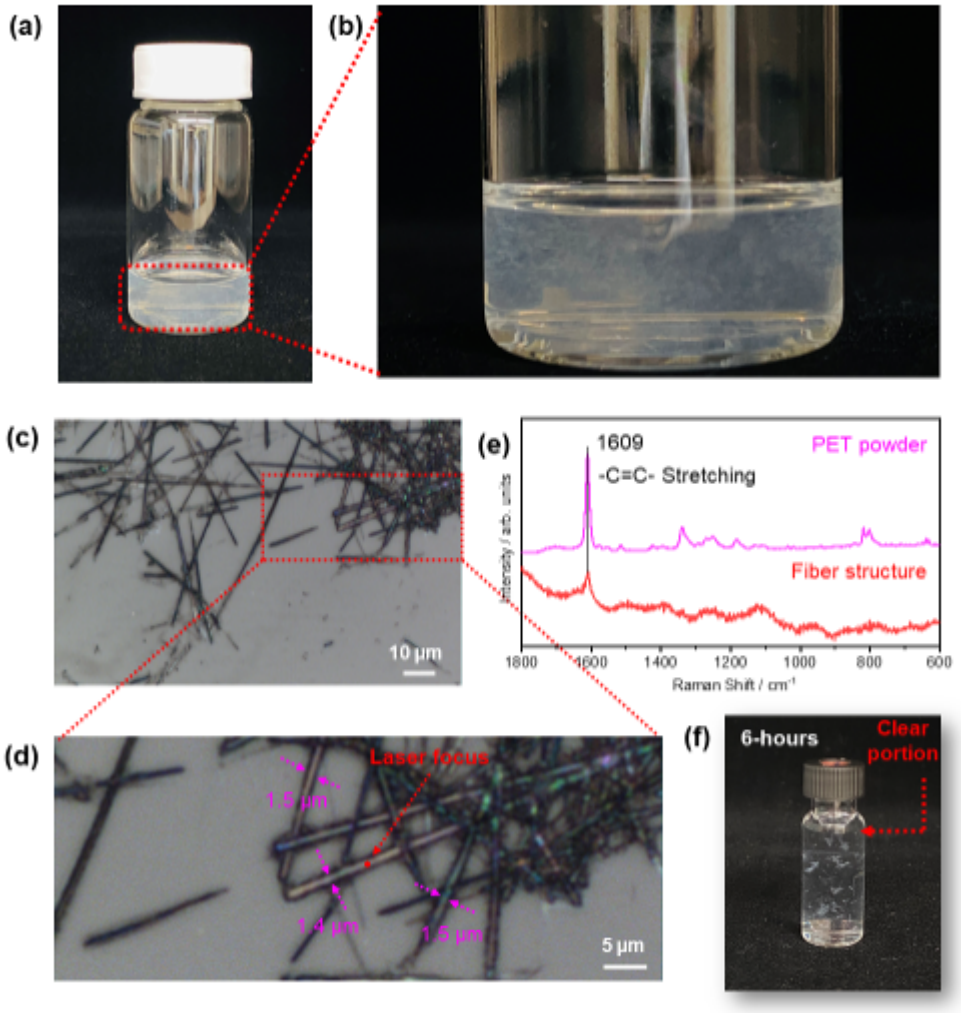

Figure A.1: (a) Image of H_6PET solution in acetone ($\sim$ 1mM). (b) Zoom-in image, showing abundance of fiber formation. (c)–(d) Optical images of unidirectional fibers. (e) Confocal Raman spectra of fibers (red) and H_6PET powder (pink). (f) 6-Hours solution where a few µL solution is taken from the clear portion for experimental analysis. Large-scale fibrous structures are visible.

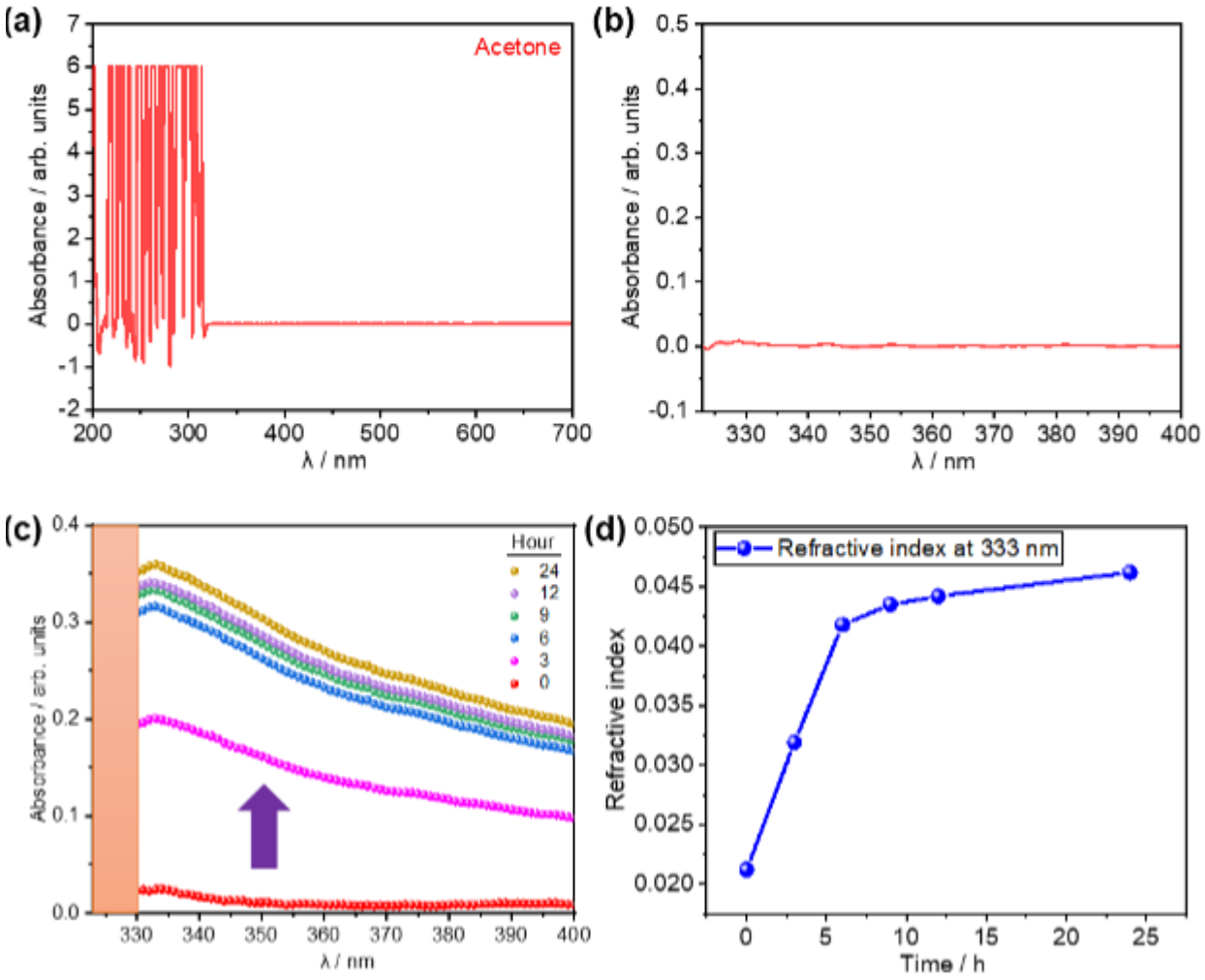

Figure A.2: (a) UV-Vis Spectrum of pure acetone. (b) Zoom-in range (323–400 nm) showing a flat base line. (c) UV-Vis Spectra of spontaneous fiber formation recorded with time (0 $\rightarrow$ 3 $\rightarrow$ 6 $\rightarrow$ 9 $\rightarrow$ 12 $\rightarrow$ 24 hours). Due to light scattering, the absorbance increases as time progresses. (d) Corresponding refractive index change of the solution over time

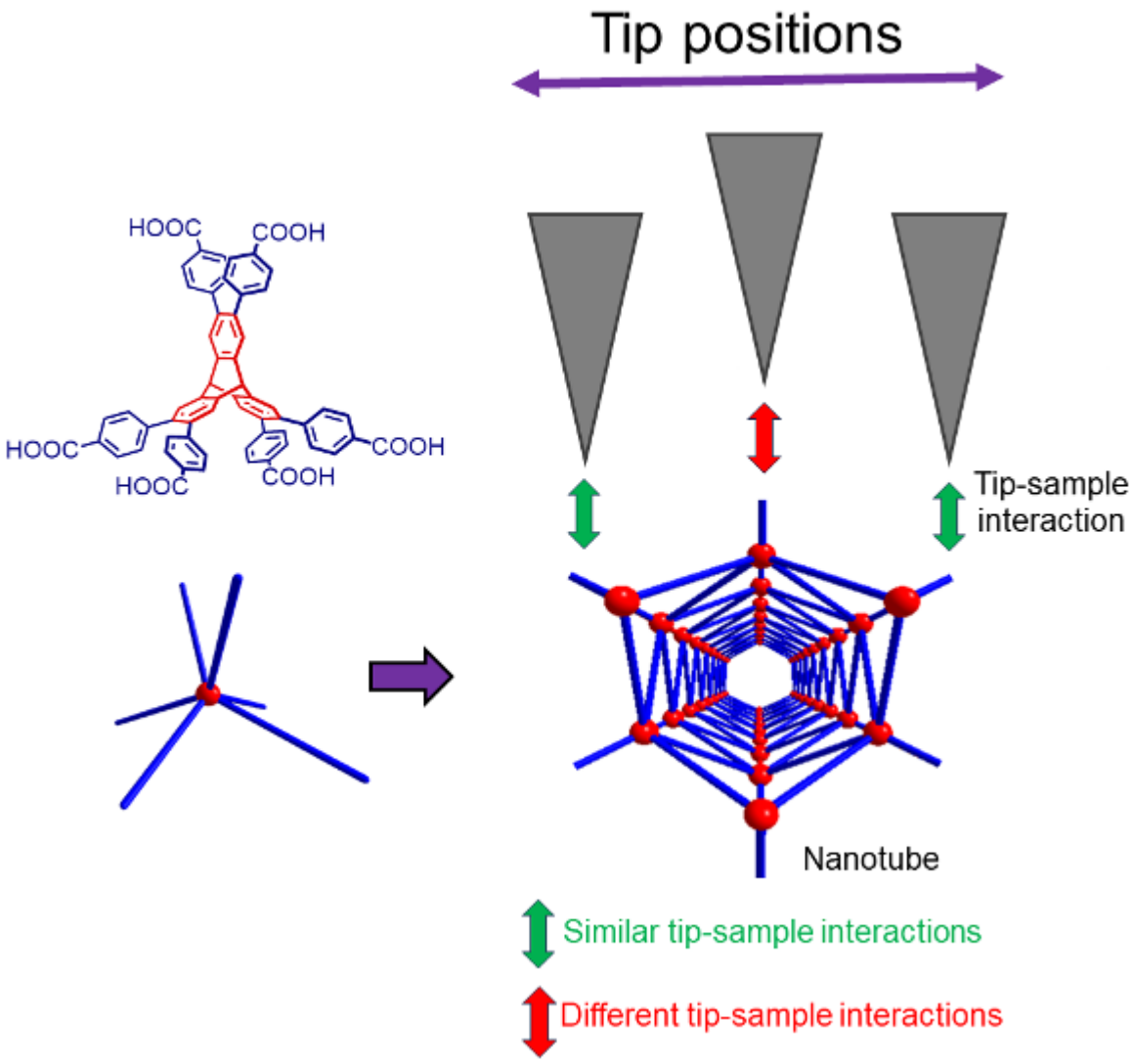

Figure A.3: Schematic illustration of similar and different tip-sample interactions at the two sidewalls and center of the nanotube, respectively. Molecular configuration leads predominantly to interaction variations between tip and sample.

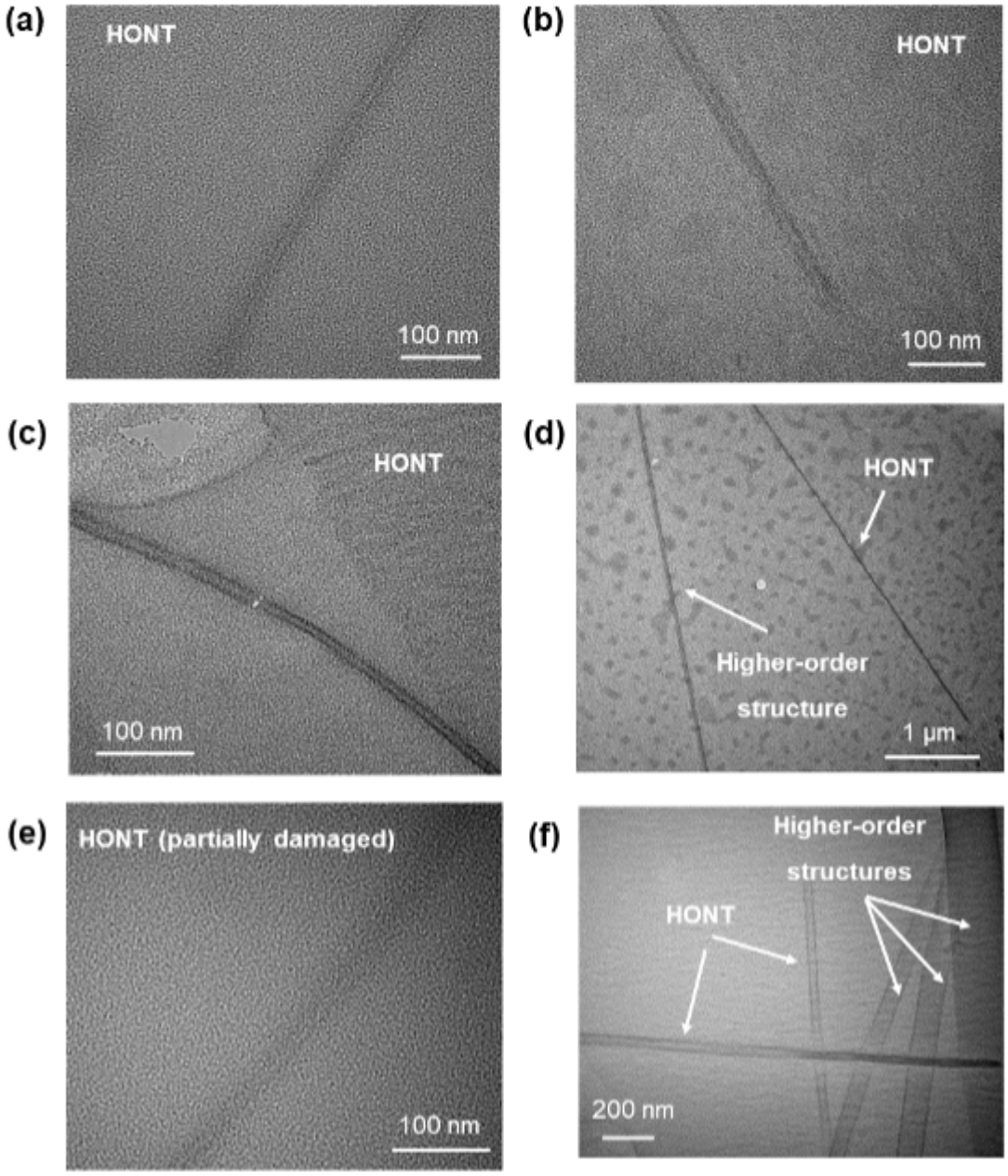

Figure A.4: (a)-(c) Additional TEM images of hydrogen-bonded organic nanotubes (HONTs), showing predominantly a unidirectional nature. (e) Strong electron energy could damage the nanotube while imaging. (d) and (f) Presence of higher-order structures (larger width compare to nanotube) along with HONTs (0-hour solution). The higher-order structures also exhibit predominantly one-dimensional nature.

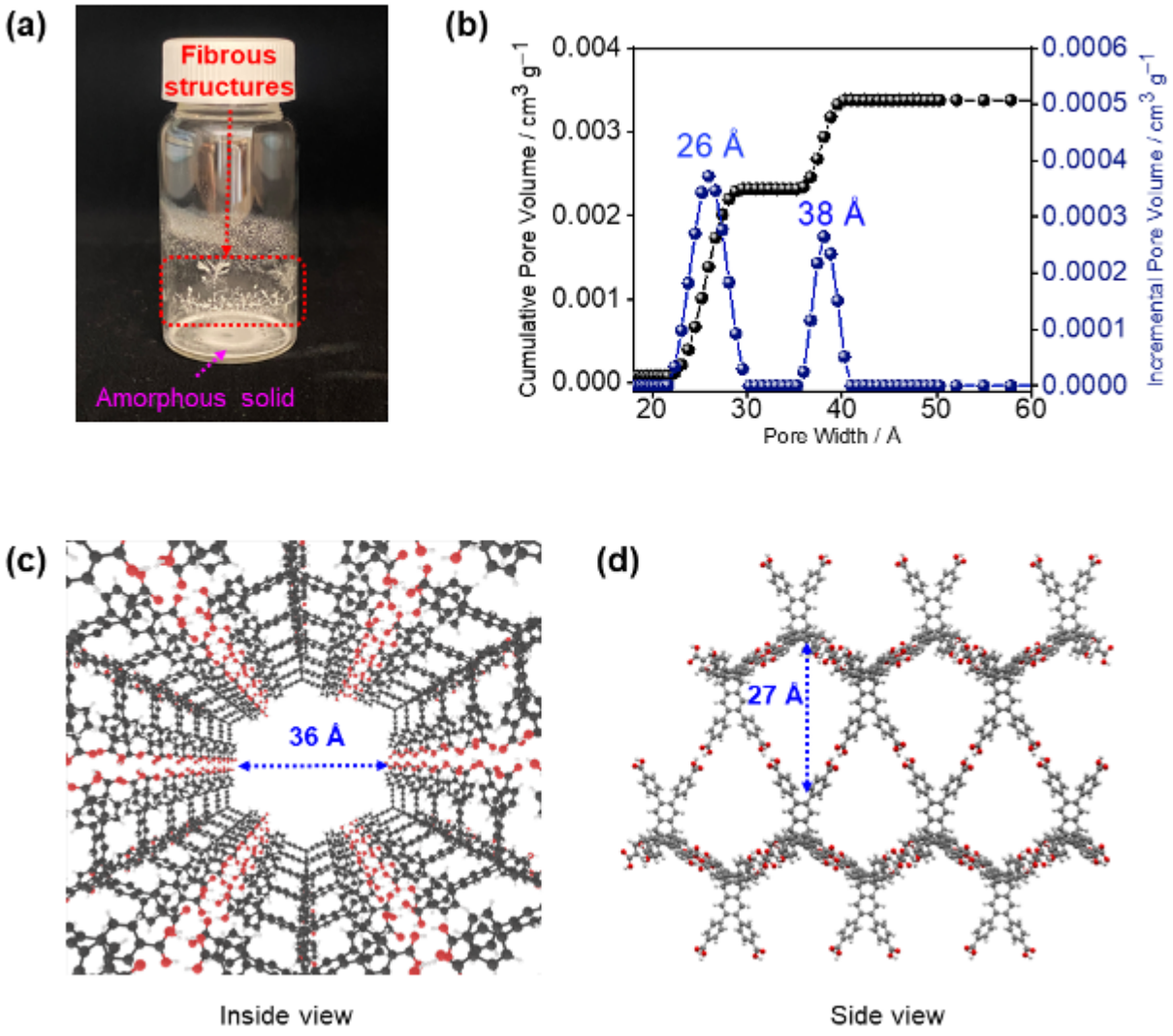

Figure A.5: (a) Example of the sample used for gas adsorption isotherm experiments. After the solvent is completely evaporated, fiber structures (at the side walls) as well as amorphous solid (down part of the vial) are visible. (b) Pore size distribution of hydrogen-bonded fibers, showing two types of pores [i.e., 22–30 Å and 35–41 Å]. (c) Inside view of nanotube model, showing the hollow tubular channel (∼36 Å). (d) Side view of nanotube model, illustrating ∼27 Å pore at the sidewalls

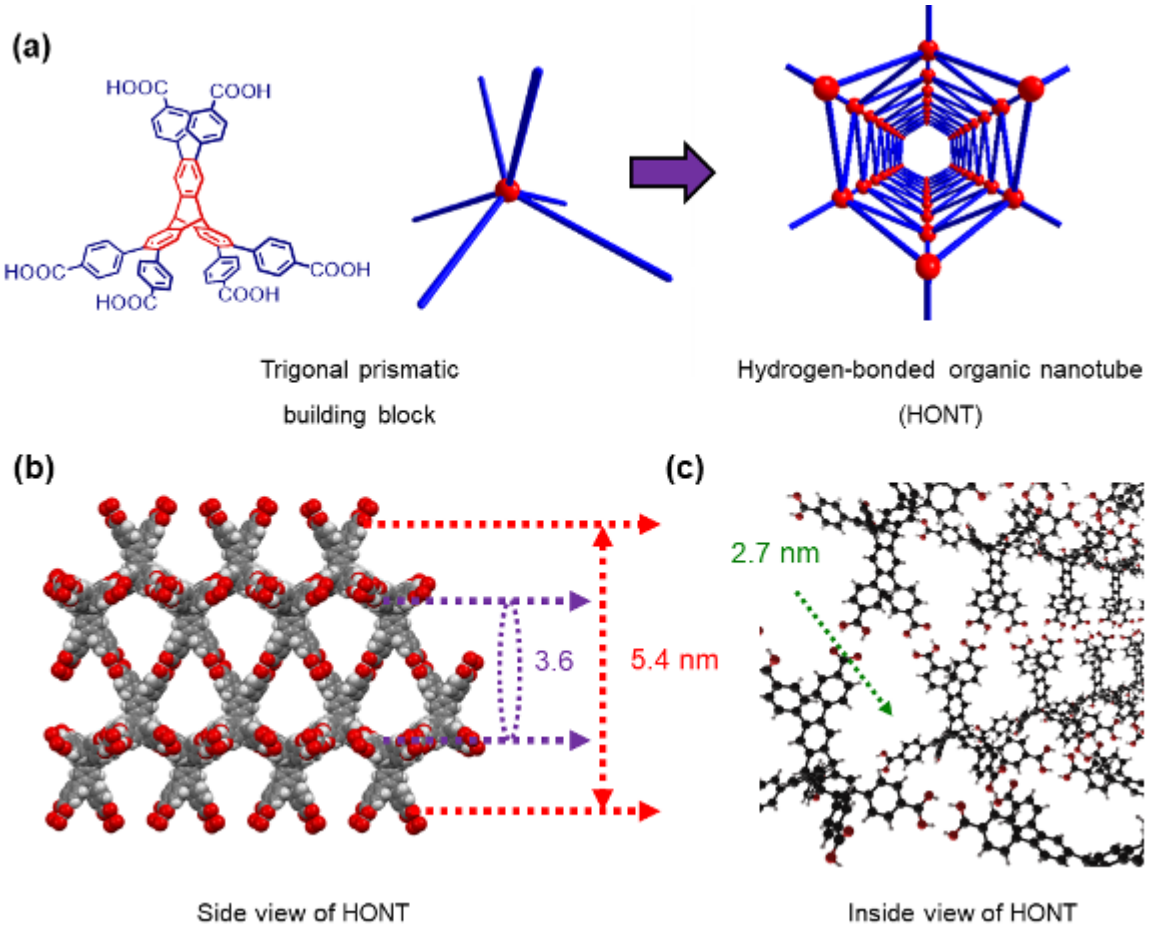

Figure A.6: (a) Schematic illustrtaion of highly anisotropic hydrogen-bonded organic nanotube model from trigonal prosmatic building blocks. (b) Side view of nanotube model, showing an external diameter of ∼5.4 nm and an internal diameter of ∼3.6 nm. The model is consistent with the AFM and TEM experiments as well as pore size distribution results. (c) Inside view of nanotube model, illustrating the ∼2.7 nm pore (at sidewalls) more clearly

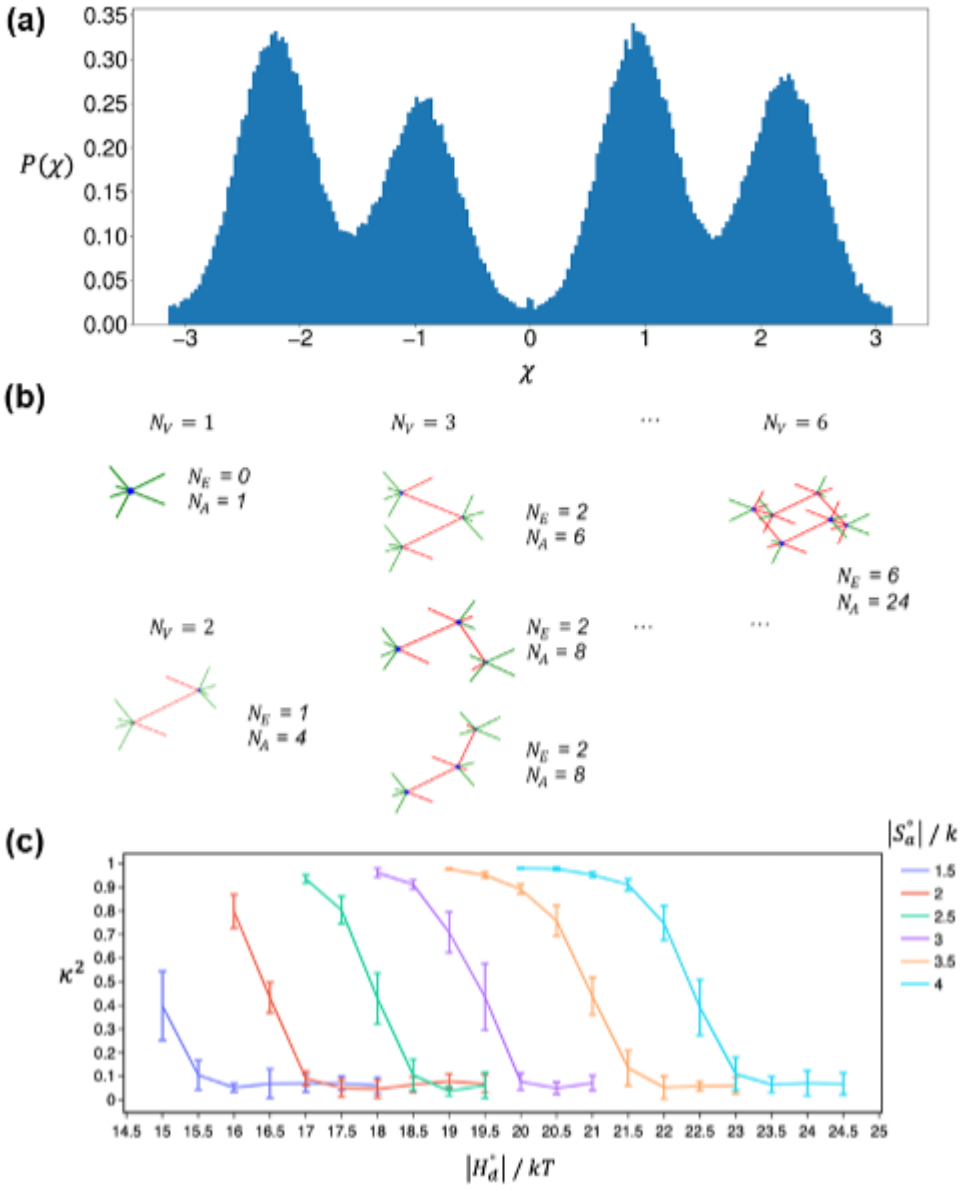

Figure A.7: (a) Density distribution of the dihedral angles of the arms of H_6PET. The four peaks correspond to the four minima in the dihedral potential energy. (b) Schematic illustrtaion of graph representation from monomer to six-membered ring configuration. N_V, N_E and N_A denotes number of vertices, edges, and restricted arms, respectively. (c) Shape anisotropy as function of hydrogen bond strength. As the hydrogen bonds become stronger, the anisotropy decreases.

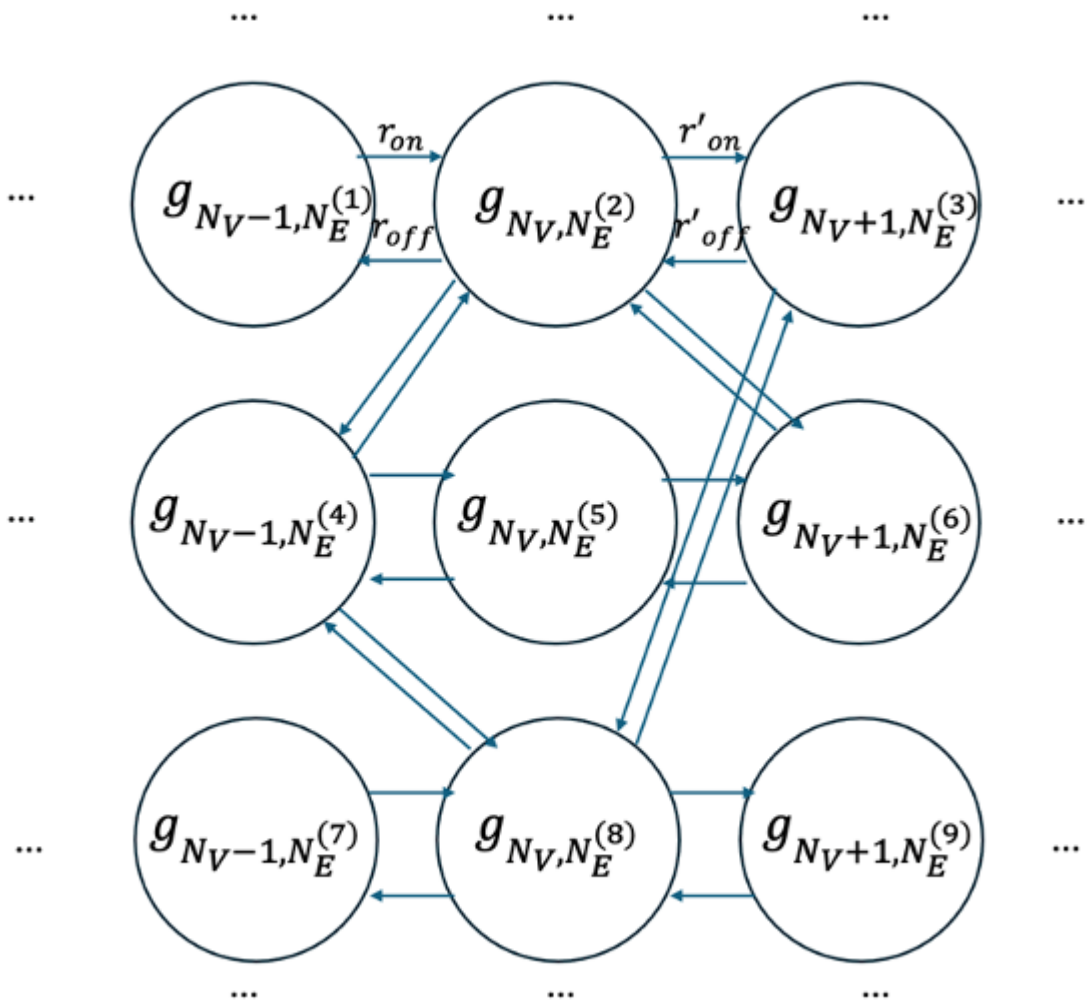

Figure A.8: Schematic representation of the kinetic Monte Carlo simulation of self-assembly of H_6PET. The system evolves by adding or removing one monomer and there is no correlation between successive events. The simulation is effectively a kinetic sampling of the density distribution of the fragment space $\{g_{N_V,N_E}\}$.

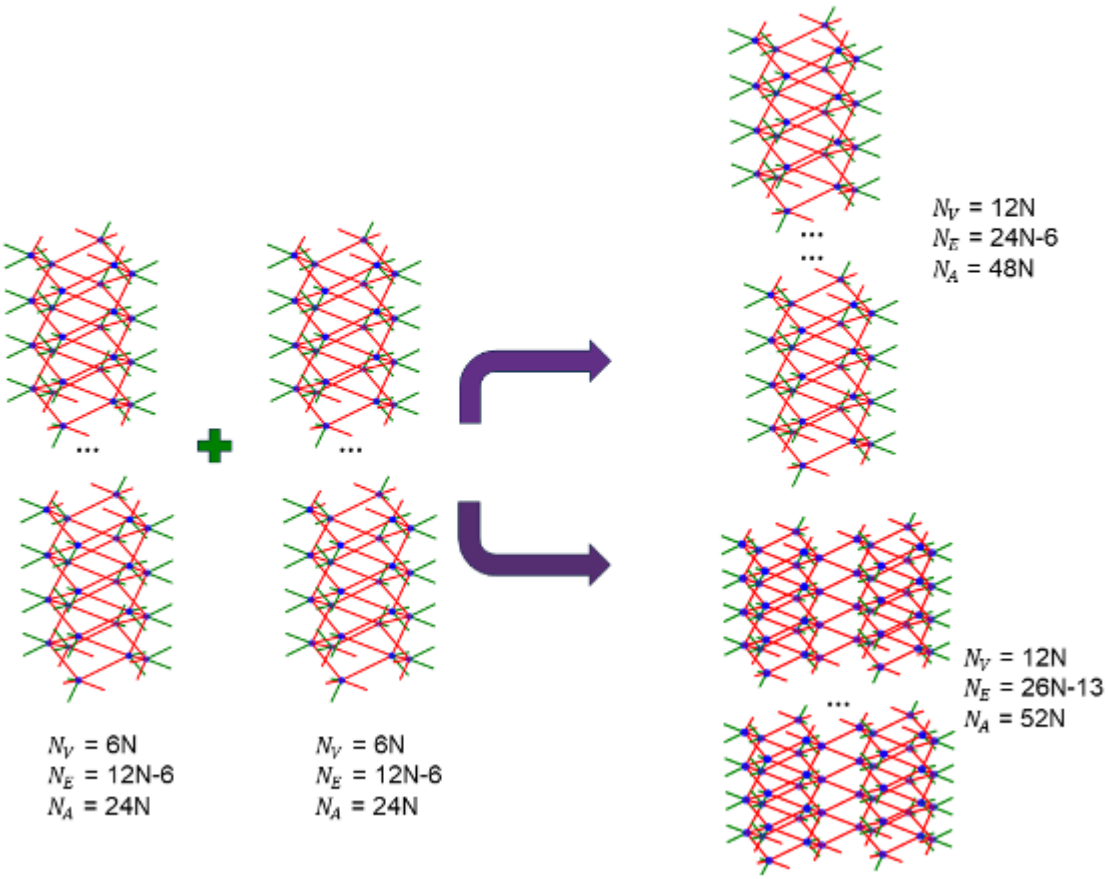

Figure A.9: Schematic illustration of self-assembly of two 0th-order nanotubes. The nanotubes can assemble transversely or longitudinally. When the lengths of the nanotubes are large, it is much more stable for them to assemble transversely. This schematic diagram illustrates one possibility way of generating higher-order structures. N_V, N_E and N_A denotes number of vertices, edges, and restricted arms, respectively.

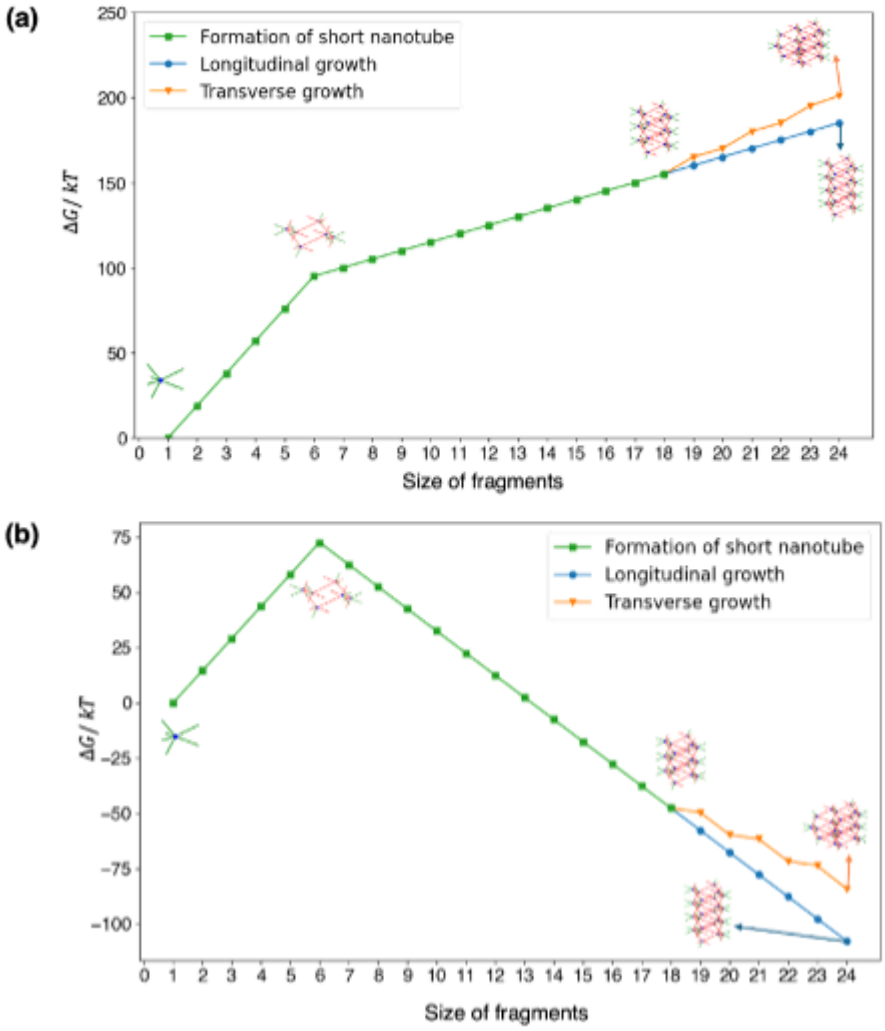

Figure A.10: Free energy landscapes in the regime of no assembly, and formation of 3D structures. (a) Free energy landscapes when the hydrogen bond strength $|\Delta H_d^\circ| = 14kT$ and the entropy loss of restricted arms $|\Delta S_a^\circ| = 2.5k$. The free energy keeps going up as size increases so there is no extensive growth. (b) Free energy landscapes when the hydrogen bond strength $|\Delta H_d^\circ| = 24.5kT$ and the entropy loss of restricted arms $|\Delta S_a^\circ| = 4k$. The free energy decreases in the process of transverse growth as well as longitudinal growth. Therefore the growths in all directions are all diffusion-limited and the growth rate is almost identical. Therefore, the assembly is three-dimensional.

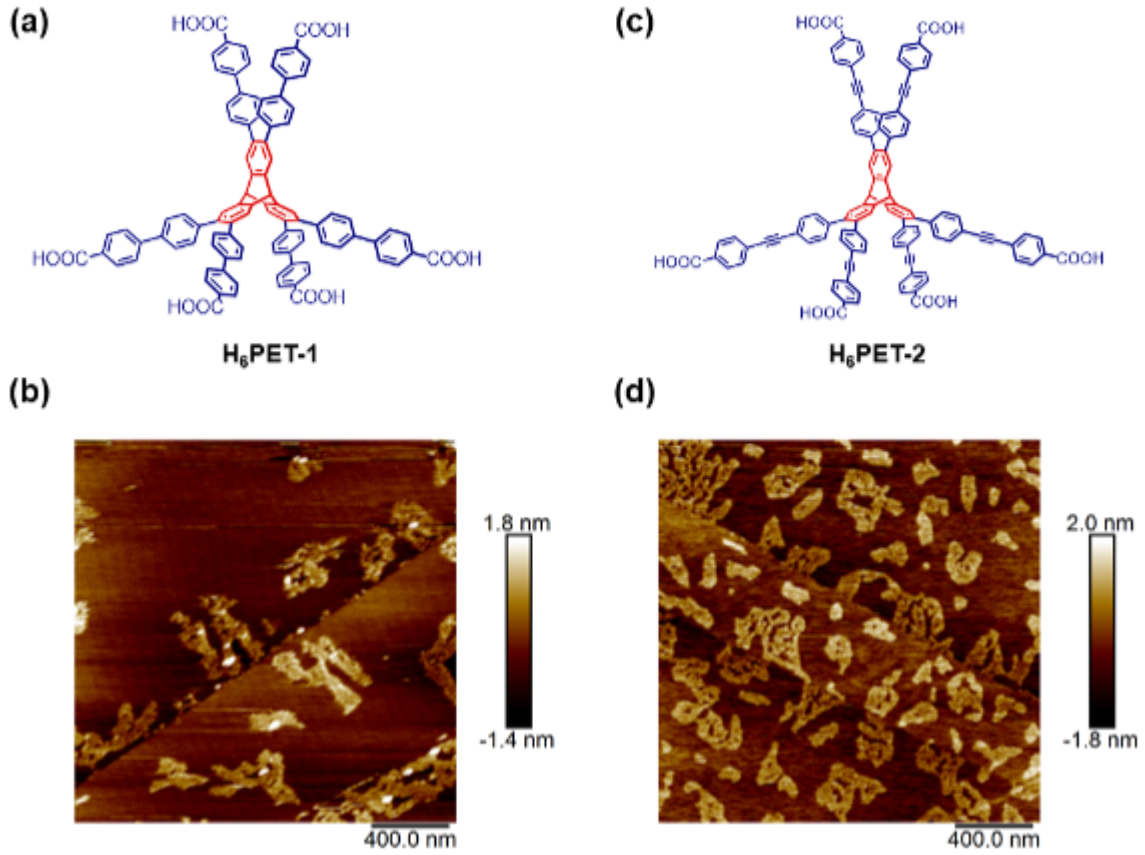

Figure A.11: (a) and (c) Structural formula of H_6PET-1 and H_6PET-2, respectively with varying the arm lengths. (b) and (d) Corresponding AFM height images of H_6PET-1 and H_6PET-2, respectively when the solution is dropcasted from acetone on HOPG surface under ambient conditions. In contrast to H_6PET, these two monomers do not provide fiber structures in acetone. Also, no nanotube or higher-order structures are found in AFM images. As a results of poor AFM resolution, the structural features remain unidentified.

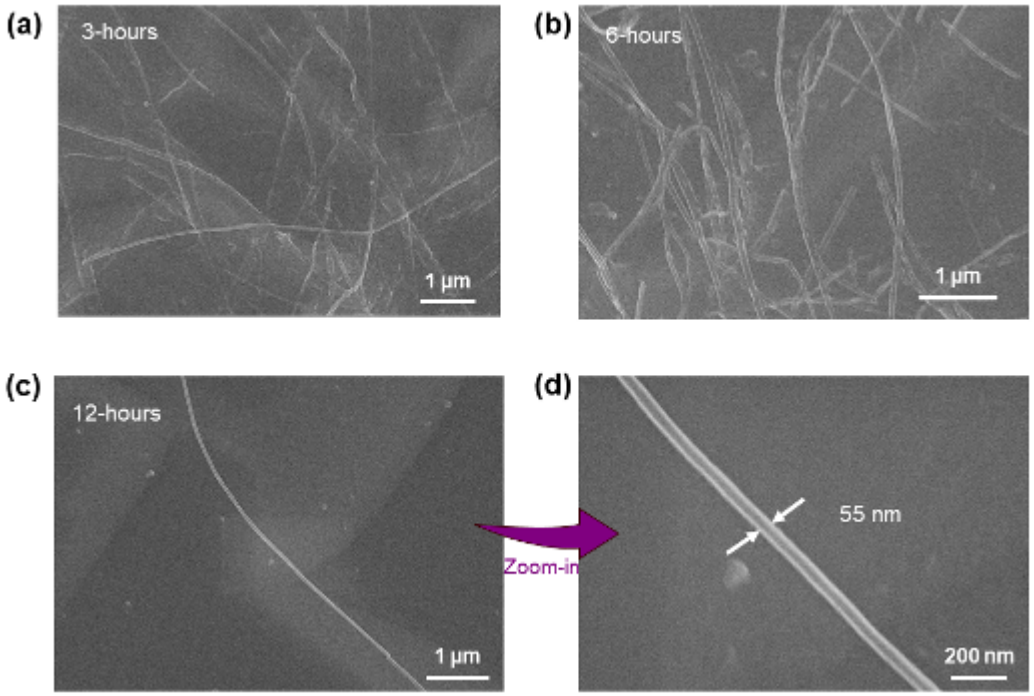

Figure A.12: (a) and (b) Representative large-scale SEM images of 3-hours and 6-hours solutions (respetively), showing many nanofiber structures. (c) Representative large-scale SEM images of a 12-hours solution. The nanofiber population has decreased significantly. (d) Zoom-in SEM image of one such nanofiber (12-hour solution), showing $\sim$55 nm width

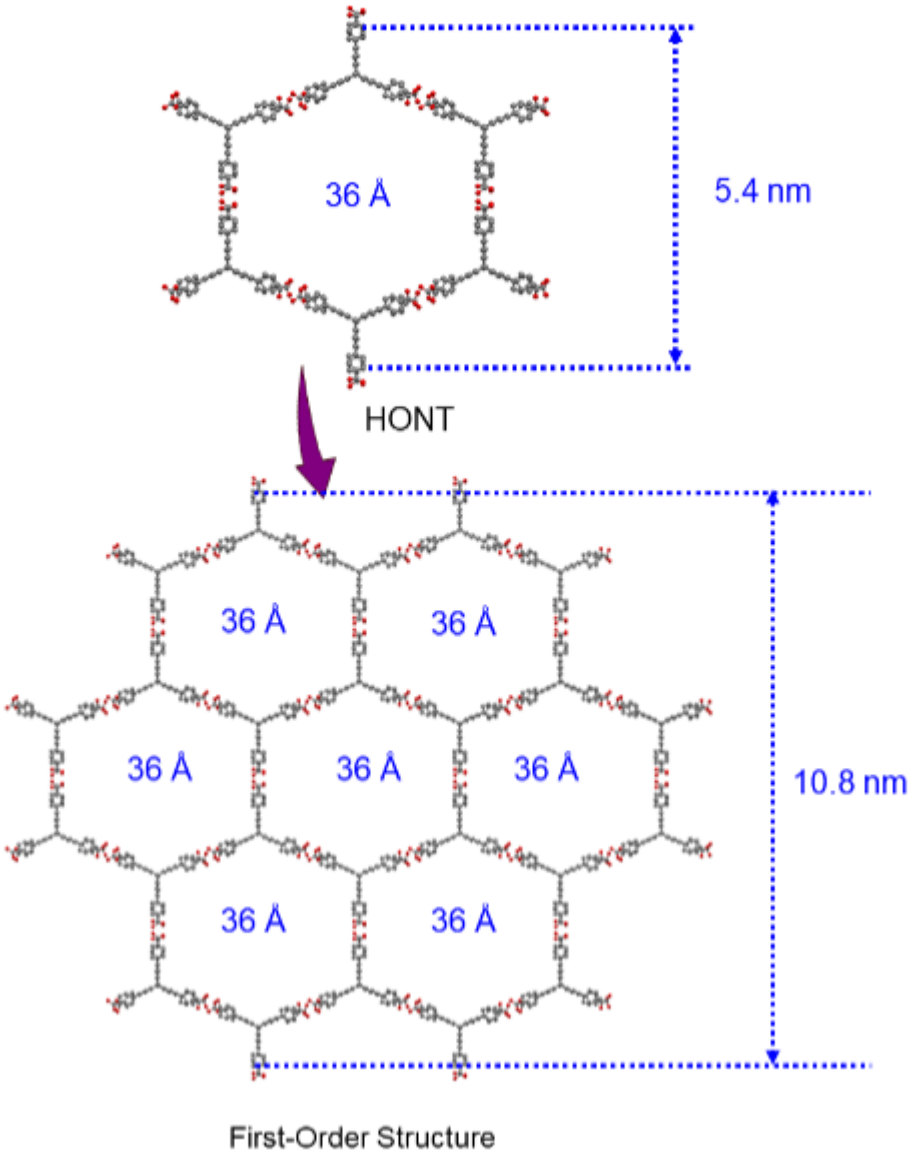

Figure A.13: Tentative Model of HONT and first-order structure. The model suggests a ∼5.4 nm diameter for nanotube and ∼10.8 nm diameter for first-order structure. The pore sizes also remain consistent as the nanotube grows towards higher-order structures. The first-order structure can grow towards higher-order structures with the similar process.

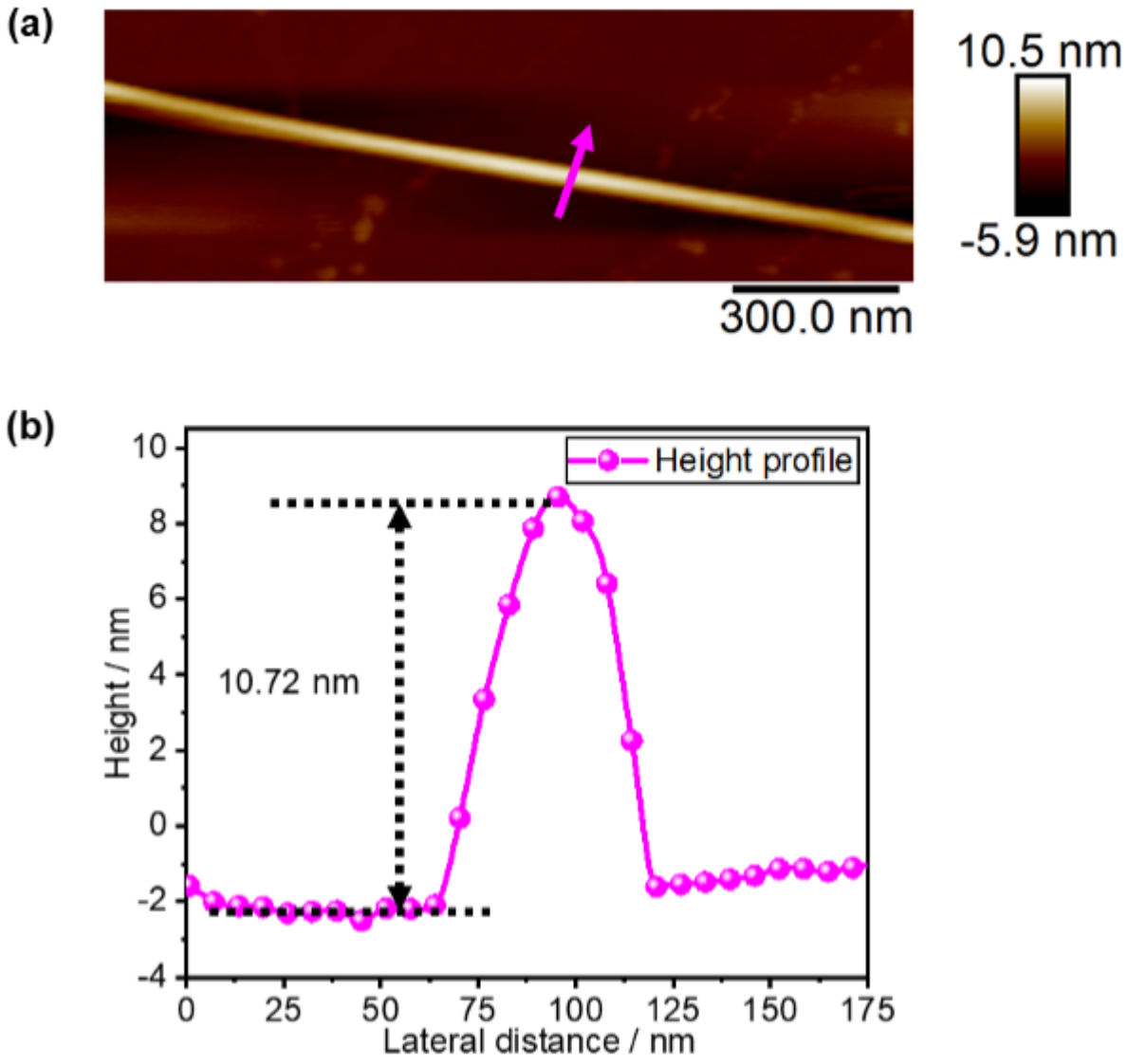

Figure A.14: (a) Representative AFM height image of first-order structure, showinf unidirectional nature. (b) Corresponding height profile from the pink arrow, illustrating ∼10.72 nm height (external diameter). It is in line with the model predicted value of ∼10.8 nm.

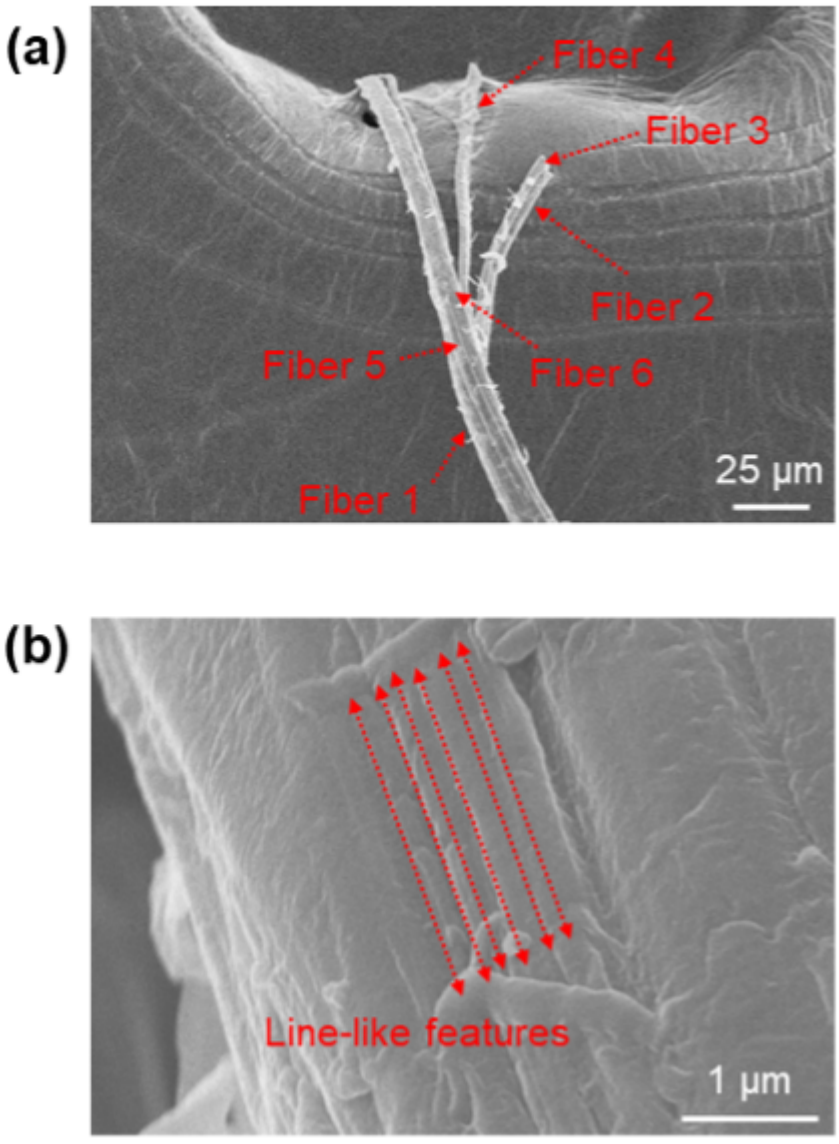

Figure A.15: (a) Corressponding SEM image of microfibers (10–15 μm width). (b) Zoom-in SEM image of one such fiber, showing multiple line-like features